



CENTRO DE INVESTIGACIÓN Y DE ESTUDIOS  
AVANZADOS DEL INSTITUTO POLITÉCNICO NACIONAL

Chemistry Department  
Zacatenco Campus

*Asymptotic expansion of molecular integrals in  
self-consistent auxiliary density functional methods*

**Thesis submitted by**  
Aurelio Álvarez Ibarra

**In order to obtain the**  
**Doctor in Science**

**Degree, in the speciality of**  
Chemistry Sciences

**Thesis director:** Dr. Andreas Köster

Mexico City

August 2013





CENTRO DE INVESTIGACIÓN Y DE ESTUDIOS  
AVANZADOS DEL INSTITUTO POLITÉCNICO NACIONAL

Departamento de Química  
Unidad Zacatenco

*Expansión asintótica de integrales moleculares en métodos  
de teoría de funcionales de la densidad auxiliar  
autoconsistente*

**Tesis que presenta**  
Aurelio Álvarez Ibarra

**para obtener el grado de**  
**Doctor en Ciencias**

**en la especialidad de**  
Ciencias Químicas

**Director de tesis:** Dr. Andreas Köster

Ciudad de México

Agosto 2013



El presente trabajo se realizó en el Departamento de Química del Centro de Investigación y de Estudios Avanzados del Instituto Politécnico Nacional (CINVESTAV-IPN) bajo la dirección del Prof. Dr. Andreas M. Köster y con el apoyo de la beca No. 210726 otorgada por el Consejo Nacional de Ciencia y Tecnología (CONACyT).



*A mi madre, quien me enseñó, entre muchas otras cosas, el valor del esfuerzo y dedicación en todos los aspectos de la vida. He aquí otro fruto de tu trabajo.*

*A mi padre, mi hermana y toda mi familia, quienes me vieron nacer, me educaron y me acompañan a través del maravillosamente complejo camino de la vida*

*A Laura, la mujer de mi vida, quien con su ejemplo y apoyo me muestra las cosas por las que vale la pena luchar. Juntos lo estamos aprendiendo.*



# Agradecimientos

A los profesores del jurado que diligentemente evaluaron este trabajo y amablemente aportaron su conocimiento para mejorarlo:

Dr. Samuel B. Trickey

Dr. Claudio Marcelo Zicovich Wilson

Dr. Omar Solorza Feria

Dr. Alberto Vela Amieva

Dra. Rosa Santillán Baca

Al Dr. Andreas M. Köster quien me aceptó bajo su tutela y me demostró las virtudes del trabajo consistente y organizado, además de compartir conmigo valiosas opiniones acerca del crecimiento personal y el servicio a la comunidad.

A los profesores y compañeros del departamento de Química quienes han compartido conmigo no sólo su conocimiento científico sino también su visión personal en muchos aspectos de la vida. Todos ustedes han participado en el proceso del cual este trabajo se ha producido.

Al Centro de Investigación y de Estudios Avanzados (CINVESTAV) por el apoyo material y financiero para la realización de este trabajo. A la administración de los sistemas de cómputo de alto desempeño *Xiuhcoatl* del CINVESTAV y *WestGrid* de la plataforma Compute Canada. Al Consejo Nacional de Ciencia y Tecnología por el apoyo financiero otorgado a través de la beca número 210726.



# Contents

List of Figures	i
List of Tables	v
List of Acronyms and Symbols	vii
Related work	xi
Abstract	xv
Introduction	xix
<b>1 Quantum chemistry fundamentals</b>	<b>1</b>
1.1 The Schrödinger equation . . . . .	1
1.2 Density functional theory . . . . .	5
1.2.1 Hohenberg-Kohn theorems . . . . .	5
1.2.2 The Kohn-Sham method . . . . .	8
<b>2 Methodology for DFT calculations</b>	<b>13</b>
2.1 Linear combination of atomic orbitals . . . . .	13
2.1.1 Gaussian type orbitals . . . . .	13
2.1.2 The LCGTO Kohn-Sham method . . . . .	14
2.2 Variational fitting of the Coulomb potential . . . . .	17
2.3 Auxiliary density functional theory . . . . .	21
<b>3 Molecular integral evaluation</b>	<b>25</b>

3.1	Notation . . . . .	25
3.2	The Gaussian product theorem . . . . .	26
3.3	Overlap integrals . . . . .	27
3.4	The Boys function . . . . .	29
3.5	Nuclear attraction integrals . . . . .	30
3.6	Electron repulsion integrals . . . . .	33
	3.6.1 Calculation of the Kohn-Sham matrix elements . . . . .	33
	3.6.2 Calculation of the Coulomb vector elements . . . . .	36
3.7	Analytic energy derivative . . . . .	39
	3.7.1 GTO derivatives . . . . .	41
	3.7.2 Overlap integral derivatives . . . . .	42
	3.7.3 Nuclear attraction integral derivatives . . . . .	44
	3.7.4 Electron repulsion integral derivatives . . . . .	47
3.8	Asymptotic expansion of electron repulsion integrals . . . . .	50
	3.8.1 Asymptotic expansion of the Kohn-Sham matrix elements . . . . .	54
	3.8.2 Asymptotic expansion of the Coulomb vector elements . . . . .	56
<b>4</b>	<b>Double asymptotic expansion of electron repulsion integrals</b>	<b>59</b>
	4.1 A second asymptotic expansion for ERIs . . . . .	59
	4.2 Double asymptotic expansion of the Kohn-Sham matrix elements . . . . .	64
	4.3 Double asymptotic expansion of the Coulomb vector elements . . . . .	66
	4.4 Asymptotic expansion of nuclear attraction integrals . . . . .	69
	4.5 Double asymptotic expansion for ERI derivatives . . . . .	73
	4.6 Asymptotic expansion of the embedding integral derivatives . . . . .	81
<b>5</b>	<b>A new mixed SCF scheme</b>	<b>87</b>
	5.1 The SCF procedure . . . . .	87
	5.2 The SCF schemes . . . . .	89
	5.3 The near-field ERIs bottleneck . . . . .	90
	5.4 A new solution for the I/O bottleneck . . . . .	90
<b>6</b>	<b>Validation and performance of the code</b>	<b>93</b>
	6.1 Electron repulsion integrals . . . . .	93

6.1.1	Direct SCF ERIs . . . . .	94
6.1.2	ERI gradients . . . . .	101
6.2	Embedding integrals . . . . .	103
6.2.1	Core embedding integrals . . . . .	104
6.2.2	Embedding integral gradients . . . . .	107
6.3	The mixed SCF scheme . . . . .	108
6.4	Perspectives . . . . .	110
6.4.1	RNA polymerase II in water . . . . .	110
6.4.2	Molecular dynamics of the $\text{Na}_{55}^+$ cluster . . . . .	112
6.4.3	Geometry optimization of the insulin monomer . . . . .	115
<b>7</b>	<b>Conclusions and future work</b>	<b>119</b>
7.1	Conclusions . . . . .	119
7.2	Future work . . . . .	121
	<b>Appendices</b>	<b>123</b>
<b>A</b>	<b>The positive semidefinite nature of the variational fitting error</b>	<b>125</b>
<b>B</b>	<b>Double asymptotic expansion of two-center ERIs with HGTF</b>	<b>129</b>
	<b>Bibliography</b>	<b>131</b>



# List of Figures

3.1	The Gaussian product theorem. The product of two Gaussian functions (blue and black) results in a third Gaussian function (red). . . . .	26
3.2	Pathway diagram for the calculation of the overlap integrals. . . . .	28
3.3	The Boys function of orders 0, 1 and 2 calculated with Eq. (3.9) (solid line) and the asymptotic expansion in Eq. (3.11) (dashed lined). . . .	30
3.4	Pathway diagram for the calculation of nuclear attraction integrals. .	30
3.5	Pathway diagram for the calculation of the electron repulsion integrals for the Kohn-Sham matrix. . . . .	34
3.6	Pathway diagram for the calculation of the Coulomb vector. Unlike previous diagrams, this one is read from both ends toward the middle.	36
3.7	Assignment diagrams for the inverse horizontal recurrence relation of a) $dd$ and b) $ff$ density matrix elements. The shift steps are represented by horizontal arrows and the compaction steps by vertical arrows. . .	37
3.8	Assignment diagrams for the inverse orbital product transformation of a) $ds$ and b) $fs$ density matrix elements. Shift steps are represented by horizontal arrows, compaction steps by vertical arrows and reduction steps by out-of-plane arrows. . . . .	38
3.9	Pathway diagram for the calculation of the overlap integral derivative up-shift term. . . . .	43
3.10	Pathway diagram for the calculation of the overlap integral derivative down-shift term. . . . .	43
3.11	Pathway diagram for the calculation of the nuclear attraction integral derivative up-shift term. . . . .	46

3.12	Pathway diagram for the calculation of the nuclear attraction integral derivative down-shift term. . . . .	46
3.13	Pathway diagram for the calculation of the nuclear attraction integral derivative with respect to the operator center. . . . .	47
3.14	Pathway diagram for the calculation of the electron repulsion integral derivative up-shift term. . . . .	49
3.15	Pathway diagram for the calculation of the electron repulsion integral derivative down-shift term. . . . .	49
3.16	Pathway diagram for the calculation of the electron repulsion integral derivative with respect to the auxiliary function center. . . . .	50
3.17	Conditions for the application of the asymptotic expansion of ERIs. a) One of the atoms overlaps with the near-field region of the potential $\phi_{\bar{e}}(\vec{r})$ thus the asymptotic expansion is not feasible. b) Both atoms are outside the near-field region of the potential $\phi_{\bar{e}}(\vec{r})$ , thus the asymptotic expansion can be applied. . . . .	53
3.18	Pathway diagram for the calculation of the far-field ERIs for the Kohn-Sham matrix elements using the asymptotic expansion. . . . .	55
3.19	Pathway diagram for the calculation of the electron repulsion integral for the Coulomb vector using the asymptotic expansion. . . . .	57
4.1	Pathway diagram for the calculation of the electron repulsion integral of the Kohn-Sham matrix elements using the double asymptotic expansion. . . . .	64
4.2	Pseudocode for the calculation of the electron repulsion integral for the Kohn-Sham matrix using the double asymptotic expansion. . . . .	65
4.3	Pathway diagram for the calculation of the electron repulsion integral of the Coulomb vector using the double asymptotic expansion. . . . .	67
4.4	Pseudocode for the calculation of the electron repulsion integral for the Coulomb vector using the double asymptotic expansion. . . . .	68
4.5	Pathway diagram for the calculation of embedding integrals using the asymptotic expansion. . . . .	71
4.6	Pseudocode for the calculation of embedding integrals using the asymptotic expansion. . . . .	72

4.7	Pathway diagram for the calculation of the electron repulsion integral derivative up-shift term using the double asymptotic expansion. . . .	77
4.8	Pathway diagram for the calculation of the electron repulsion integral derivative down-shift term using the double asymptotic expansion. . .	78
4.9	Pathway diagram for the calculation of the electron repulsion integral derivative with respect to the auxiliary function center using the double asymptotic expansion. . . . .	78
4.10	Pseudocode for the calculation of the ERIs gradients using the double asymptotic expansion. . . . .	80
4.11	Pathway diagram for the calculation of the embedding integral derivative up-shift term using the asymptotic expansion. . . . .	83
4.12	Pathway diagram for the calculation of the embedding integral derivative down-shift term using the asymptotic expansion. . . . .	84
4.13	Pathway diagram for the calculation of the electron repulsion integral derivative with respect to the auxiliary function center using the double asymptotic expansion. . . . .	84
4.14	Pseudocode for the calculation of the embedding integral gradients using the asymptotic expansion. . . . .	86
5.1	The general form of the self-consistent field procedure. . . . .	88
5.2	Comparison of the self-consistent field schemes available in deMon2k.	92
6.1	Computational timings for the ERI calculation per SCF cycle of n-alkane chains. The horizontal lines between bars show the predicted baseline for the far-field ERI timings in the original deMon2k code. .	98
6.2	Computational timings for the ERI calculation per SCF cycle of hydrogen-saturated graphene sheets. The horizontal lines between bars show the predicted baseline for the far-field ERI timings in the original deMon2k code. . . . .	99
6.3	Computational timings for the ERI calculation per SCF cycle of hydrogen-saturated diamond blocks. The horizontal lines between bars show the predicted baseline for the far-field ERI timings in the original deMon2k code. . . . .	100

6.4	Computational timings for the ERI calculation per SCF cycle of n-alkane chains in one processor. The horizontal lines between bars show the predicted baseline for the far-field ERI timings in the original asymptotic expansion implementation in deMon2k. . . . .	101
6.5	Computational timings for the ERI gradients calculation per optimization cycle of n-alkane chains with eight processors. The horizontal lines between bars show the predicted baseline for the far-field ERI timings in the original asymptotic expansion implementation in deMon2k. . .	103
6.6	Comparison of computational timings for the embedding integral calculation in small QM/MM systems. . . . .	106
6.7	Total timings for embedding integral gradients (28 steps) calculation for the MgO cube system. . . . .	107
6.8	Computational timings for the ERI calculation in the single-point SCF of n-alkane chains. The scale is changed for the last few systems since the number of SCF cycles is larger. . . . .	109
6.9	The ribbon model for RNA polymerase II (left) and the embedding system for the QM/MM calculation with 124 QM atoms and 343,176 MM atoms (right). . . . .	111
6.10	Total energy of the RNA polymerase II embedded model for different numbers of point charges. . . . .	112
6.11	ERI timings for $\text{Na}_{55}^+$ BOMD simulations with different numbers of processors. . . . .	114
6.12	Total timings for $\text{Na}_{55}^+$ BOMD simulations with different numbers of processors. . . . .	114
6.13	The insulin monomer model used for geometry optimization. . . . .	116
6.14	SCF ERIs (upper) and ERI gradients (lower) timing for the geometry optimization of insulin in 64 processors using the mixed SCF scheme. . . . .	117

# List of Tables

I	Geometrical parameters for the test systems (distances in Å, angles and dihedrals in degrees). . . . .	94
II	Number of near- and far-field integrals, SCF cycles and absolute total energy differences [a.u.] between the original deMon2k and the new ERI implementation for the n-alkane test systems. . . . .	95
III	Number of near- and far-field integrals, SCF cycles and absolute total energy differences [a.u.] between the original deMon2k and the new ERI implementation for the hydrogen-saturated graphene test systems. . . . .	96
IV	Number of near- and far-field integrals, SCF cycles and absolute total energy differences [a.u.] between the original deMon2k and the new ERI implementation for the hydrogen-saturated diamond test systems. . . . .	96
V	Number of optimization cycles and absolute total energy differences [a.u.] of the converged geometries between the original deMon2k and the new ERI gradients implementation for the first twenty n-alkane chains in the test sets. . . . .	102
VI	Number of near- and far-field integrals (full sum and cut-off sum) and absolute total energy differences [a.u.] between the original deMon2k and the new implementation for the embedded RNA polymerase II fragment. . . . .	105



# List of Acronyms and Symbols

ADFT	Auxiliary density functional theory
AO	Atomic orbital
BOMD	Born-Oppenheimer molecular dynamics
deMon2k	Computational chemistry code: density of Montreal
DFT	Density functional theory
DIIS	Direct inversion in the iterative subspace
DZVP	Double-zeta valence polarization
ERI	Electron repulsion integral
FMM	Fast multipole method
GEN-A2	Automatic generated auxiliary function set of A2 quality
GGA	Generalized gradient approximation
GTO	Gaussian type orbital
HD	Hard disk
HGTF	Hermite Gaussian type function
I/O	Input / Output
LCAO	Linear combination of atomic orbital
LCGTO	Linear combination of Gaussian type orbital
LDA	Local density approximation
MM	Molecular mechanics
MO	Molecular orbital
NAI	Nuclear attraction integral
QM	Quantum mechanics
QM/MM	Quantum mechanics / Molecular mechanics
RAM	Random-access memory

RNA	Ribonucleic acid
SCF	Self consistent field
VFCP	Variational fitting of the Coulomb potential
XC	Exchange-correlation
$\mathbf{a}$	Contracted Gaussian type orbital with angular momentum index $\mathbf{a} = (a_x, a_y, a_z)$
$A, B, C$	Nucleus index
$\hat{A}$	Asymptotic multipole operator
$\hat{A}_C(\bar{\mathbf{c}})$	Nuclear attraction-like operator
$c_{ai}$	Molecular orbital coefficient of AO $\mathbf{a}$ in MO $\psi_i$
$\bar{\mathbf{c}}$	Hermite Gaussian auxiliary function with angular momentum index $\bar{\mathbf{c}} = (\bar{c}_x, \bar{c}_y, \bar{c}_z)$
$d_{cut}$	Cut-off distance
$\hat{D}_C$	Differentiation operator with respect to components of $\vec{C}$
$d_k$	Contraction coefficient
$D$	Point charge index
$\vec{\mathbf{E}}$	Electric field
$E$	Total energy
$E_{el}$	Electronic energy
$E_0$	Ground-state electronic energy
$E_H$	Coulombic electron repulsion (Hartree) energy
$E_{xc}$	Exchange-correlation energy
$\mathcal{E}$	Error of the variational fitting of the Coulomb potential
$F_n$	Boys function of order $n$
$G$	Number of grid points for numerical integration
$G_{\bar{c}\bar{d}}$	Coulomb matrix element
$g_{A_x}$	Gradient contribution of integral derivatives with respect to $A_x$
$H_{ab}$	Core hamiltonian matrix element
$\hat{H}$	Hamiltonian operator
$\hat{H}_{el}$	Electronic Hamiltonian operator
$i, j$	Electron index
$K_a$	Contraction degree of orbital $\mathbf{a}$

$K_{ab}$	Kohn-Sham matrix element
$\mathcal{L}$	Lagrange function
$M$	Number of nuclei or auxiliary functions
$M_A$	Mass of nucleus $A$
$\hat{M}$	Multipole operator
$N$	Number of electrons or orbitals
$P_{\bar{a}}$	Transformed density matrix element
$P_{ab}$	Density matrix element
$\vec{P}$	Gaussian product center
$q_D$	Charge of embedding point $D$
$r_\chi$	Atomic radius
$\vec{r}_i$	Spatial position vector of electron $i$
$\vec{R}_A$	Spatial position vector of nucleus $A$
$r_\phi$	Electrostatic potential near-field radius
$S_{ab}$	Overlap matrix element
$T_{AC}$	Diatomic Cartesian tensor
$\hat{T}_{el}$	Kinetic energy operator of electrons
$\hat{T}_{Nu}$	Kinetic energy operator of nuclei
$T_s$	Kohn-Sham kinetic energy
$\mathcal{U}$	Coulomb energy
$v$	External potential
$v_{\text{eff}}$	Kohn-Sham effective potential
$v_{xc}$	Exchange-correlation potential
$\hat{V}_{el\text{el}}$	Electron-electron interaction operator
$\hat{V}_{el\text{Nu}}$	Electron-nucleus interaction operator
$\hat{V}_{\text{NuNu}}$	Nucleus-nucleus interaction operator
$W_{ab}$	Energy-weighted density matrix element
$x_{\bar{c}}$	Density (Coulomb) fitting coefficient
$z_{\bar{c}}$	Exchange-correlation fitting coefficient
$Z_A$	Charge of nucleus $A$
$\delta_{ij}$	Kronecker delta
$\nabla$	Gradient or nabla operator

$\nabla^2$	Laplacian operator
$\lambda_n$	Hermite polynomial of order $n$
$\lambda_{ij}$	Lagrange multiplier
$\mu$	Generalized atomic orbital
$\phi_{\bar{c}}$	Electrostatic potential of auxiliary function $\bar{c}$
$\Phi$	Total wavefunction
$\Psi$	Electronic wavefunction
$\Psi_0$	Ground-state electronic wavefunction
$\Psi_t$	Trial electronic wavefunction
$\psi$	Molecular orbital
$\tilde{\rho}$	Approximated electron density
$\rho$	Electron density
$\rho_s$	Kohn-Sham electron density
$\rho_t$	Trial electron density
$\Theta$	Nuclear wavefunction
$\tau$	Integral calculation threshold
$\zeta$	Gaussian function exponent
<b>C</b>	Molecular orbital coefficient matrix
$\epsilon$	Diagonal Lagrange multiplier matrix
<b>G</b>	Coulomb matrix
<b>J</b>	Coulomb vector
<b>K</b>	Kohn-Sham matrix
$\lambda$	Lagrange multiplier matrix
<b>S</b>	Overlap matrix
<b>x</b>	Density fitting coefficient vector

# Related work

Publications related to the thesis:

- Asymptotic expansion for electrostatic embedding integrals in QM/MM calculations  
A. Alvarez-Ibarra, A. M. Köster, R. Zhang and D. R. Salahub  
*J. Chem. Theor. Comput.* **8**, 4232 (2012)
- Double asymptotic expansion of three-center electronic repulsion integrals  
A. Alvarez-Ibarra and A. M. Köster  
*J. Chem. Phys.* accepted (2013)
- A new mixed SCF scheme for electronic repulsion integrals  
A. Alvarez-Ibarra and A. M. Köster  
In preparation (2013)
- First-principles computational biochemistry with deMon2k  
A. Alvarez-Ibarra, P. Calaminici, C. Z. Gómez-Castro, R. Grande-Aztatzi, D. R. Salahub, J. M. Vásquez-Pérez, A. Vela, R. Zhang and A. M. Köster  
In preparation (2013)

Parts of the thesis have been shown as oral and poster presentations in national and international scientific lectures:

- Invited lecture: Expansión en multipolos de integrales de repulsión electrónica de largo alcance  
A. Álvarez Ibarra and A. M. Köster  
VIII Reunión Mexicana de Fisicoquímica Teórica  
Universidad de Colima  
November 12th-14th 2009, Colima, México
- Poster: Multipole expansion of electron repulsion integrals in the asymptotic limit  
A. Alvarez-Ibarra and A. M. Köster  
International Workshop on Density Functional Theory - Present and future challenges  
Universidade Federal de Minas Gerais  
May 14th-15th 2010, Belo Horizonte, Brazil
- Poster: Implementación de la expansión en multipolos para el cálculo de integrales de repulsión electrónica en el límite asintótico  
A. Álvarez Ibarra and A. M. Köster  
IX Reunión Mexicana de Fisicoquímica Teórica  
Universidad Autónoma del Estado de Hidalgo  
November 11th-13h 2010, Pachuca, México
- Poster: Desarrollo de software de simulación de primeros principios para nanomateriales  
V. Domínguez, B. Zúñiga, A. Álvarez, A. Goursot, E. Orgaz, P. Calaminici and A. Köster  
1ª Feria de Innovación Tecnológica de la Ciudad de México  
Instituto de Ciencia y Tecnología del Distrito Federal  
March 14th-17th 2011, Ciudad de México, México

- Seminar: Asymptotic expansion for MM embedding integrals  
 A. Alvarez-Ibarra  
 Theoretical Chemistry Mini-Symposium: QM/MM Developments in deMon2k  
 Centro de Investigación y de Estudios Avanzados del I.P.N  
 May 17th 2011, Ciudad de México, México
- Invited lecture: Asymptotic expansion of MM embedding integrals  
 A. Alvarez-Ibarra and A. M. Köster  
 XI deMon developers workshop  
 Jacobs University  
 July 1st-3rd 2011, Bremen, Germany
- Poster: Double asymptotic expansion of electron repulsion integrals  
 A. Alvarez-Ibarra and A. M. Köster  
 WE Heraeus Summer School for Physics 2011  
 Jacobs University  
 July 3rd-15th 2011, Bremen, Germany
- Poster: Expansión en multipolos de integrales de embebido electrostático con mecánica molecular  
 A. Alvarez-Ibarra and A. M. Köster  
 X Reunión Mexicana de Fisicoquímica Teórica  
 Universidad Autónoma del Estado de Hidalgo  
 November 10th-12h 2011, Pachuca, México
- Poster: Un nuevo procedimiento: el campo autoconsistente mixto  
 A. Alvarez-Ibarra and A. M. Köster  
 XI Reunión Mexicana de Fisicoquímica Teórica  
 Universidad Autónoma del Estado de México  
 November 8th-10th 2012, Toluca, México

Software development contribution:

- deMon2k

A. M. Koster, G. Geudtner, A. Alvarez-Ibarra, P. Calaminici, M. E. Casida, J. Carmona-Espindola, V. Dominguez, R. Flores-Moreno, G. U. Gamboa, A. Goursot, T. Heine, A. Ipatov, A. de la Lande, F. Janetzko, J. M. del Campo, J. U. Reveles, J. M. Vasquez-Perez, A. Vela, B. Zuniga-Gutierrez and D. R. Salahub

The deMon developers community 2013

# Abstract

This thesis presents the derivation and implementation of new methodologies for the rapid and efficient computation of molecular electrostatic interaction integrals in all-electron density functional theory calculations. This contribution is most significant for large-scale quantum chemistry calculations in which the molecular integral evaluation represents a large portion of the computational time. For long-range interactions, the double asymptotic expansion of electron repulsion integrals (ERI) is derived from the asymptotic expansion implemented in the electronic structure program deMon2k using the same algorithms for the near- and far-field region definition. The double asymptotic expansion achieves a simplification which reduces the formal cubic scaling of the ERI evaluation in auxiliary density functional theory to a formal quadratic scaling. The scaling reduction results from shifting the ERI auxiliary function contributions to the atomic level. As a consequence, the electrostatic interaction integrals are transformed into modified overlap integrals. Using similar arguments and formulas from the double asymptotic expansion of ERIs, an asymptotic expansion for nuclear attraction-like integrals can be obtained. This implementation is particularly useful for so-called Quantum mechanics / Molecular mechanics calculations in which the electrostatic interactions are very important.

Since the new asymptotic expansion solves the computational bottleneck for the far-field region interaction integrals, a new self-consistent field (SCF) methodology was derived to solve the computational bottleneck for the near-field ERI calculation. The so-called mixed SCF scheme is a combination of the conventional and direct SCF approaches. It uses the memory available in the computational architecture to store near-field ERIs prior to the SCF, hence they have to be calculated only once for a

given structure, similar as the conventional SCF. The far-field ERIs are re-calculated every SCF step employing the double asymptotic expansion similar as the direct SCF.

The contributions achieved in this thesis open the avenue for large-scale calculations with reasonable timings using all-electron density functional theory methods. Examples of this new possibility are shown in collaborations in the area of biochemistry and nanotechnology currently taking place using the program deMon2k. The results of these collaborations indicate a remarkable reduction in the ERI and embedding integrals computation time, showing that the electrostatic interaction calculations are no longer a bottleneck in large-scale quantum chemistry studies.

# Resumen

Esta tesis presenta la derivación e implementación de nuevas metodologías para la computación rápida y eficiente de integrales moleculares de interacción electrostática en cálculos de teoría de funcionales de la densidad con todos los electrones. Esta contribución es más significativa para cálculos de química cuántica de gran escala en las cuales la evaluación de integrales moleculares representa una gran parte del tiempo computacional. Para interacciones de largo alcance, la expansión asintótica doble de integrales de repulsión electrónica se deriva de la expansión asintótica implementada en el programa de estructura electrónica deMon2k usando los mismos algoritmos para la definición de regiones de campo cercano y campo lejano. La expansión asintótica doble logra una simplificación que reduce el escalamiento formal cúbico en la evaluación de las integrales de repulsión electrónica en la teoría de funcionales de la densidad auxiliar a un escalamiento formalmente cuadrático. La reducción de escalamiento resulta de desplazar las contribuciones de funciones auxiliares en las integrales de repulsión electrónica al nivel atómico. Como consecuencia, las integrales de interacción electrostática son transformadas en integrales de traslape modificadas. Usando argumentos y fórmulas similares de la expansión asintótica doble de las integrales de repulsión electrónica se obtiene una expansión asintótica para integrales de tipo atracción nuclear. Esta implementación es particularmente útil para los llamados cálculos de mecánica cuántica / mecánica molecular en los cuales las interacciones electrostáticas son muy importantes.

Puesto que la nueva expansión asintótica resuelve el cuello de botella computacional de las integrales de interacción en regiones de campo lejano, una nueva metodología de campo autoconsistente fue derivada para resolver el cuello de botella computacional.

cional para el cálculo de las integrales de repulsión electrónica de campo cercano. El llamado esquema de campo autoconsistente mixto es una combinación de los enfoques de campo autoconsistente convencional y directo. Se usa la memoria disponible en la arquitectura computacional para almacenar integrales de repulsión electrónica de campo cercano previo al campo autoconsistente y por lo tanto deben ser calculadas sólo una vez para una estructura dada, similar al campo autoconsistente convencional. Las integrales de repulsión electrónica de campo lejano son recalculadas en cada paso de campo autoconsistente empleando la expansión asintótica doble, similar al campo autoconsistente directo.

Las contribuciones logradas en esta tesis abren el camino para cálculos de gran escala en tiempos razonables usando métodos de teoría de funcionales de la densidad con todos los electrones. Se muestran ejemplos de esta nueva posibilidad con colaboraciones en el área de la bioquímica y la nanotecnología que actualmente se llevan a cabo usando el programa deMon2k. Los resultados de estas colaboraciones indican una reducción notable en el cómputo de integrales de repulsión electrónica e integrales de embebido, mostrando que el cálculo de interacciones electrostáticas no son más un cuello de botella en estudios de química cuántica de gran escala.

# Introduction

With the rise of consciousness in humans beings, their interest in the composition and change of their environment started. This led to the birth of natural sciences. Chemistry, as one of them, deals with the composition, structure and properties of substances and of the transformations that they undergo. The questions about the composition of matter can be traced back to ancient Greece. One of the schools on the structure of matter was started by Leucippus and further developed by his successor Democritus. They postulated that matter is made of small, inseparable particles called *atoms* (without division, indivisible) [1,2]. Aristotle, on the other hand, supported the belief in the four-element nature of matter [3] and attacked and discredited the atomistic school. Since Aristotle was very respected, his ideas remained accepted for centuries. However, during the Renaissance several scientists criticized the work of Aristotle, thereby starting the return of the atomistic ideas.

At the end of the XVIII century, the developments in mathematics and physics motivated studies of matter in a corpuscular fashion. Guided by the work of Lavoisier on mass conservation during a chemical reaction [4] in the first decades of the XIX century, Proust and Dalton stated that compounds were constituted by combinations of indivisible particles [5–7]. Proust enunciated the concept that a given compound can be formed only by a specific combination of elements. Dalton claimed that when two or more different atoms combine to form more than one compound they always do it in ratios of simple integer numbers. After further works by Avogadro and Cannizzaro on the structure of gases, Newlands in 1864 [8,9] and Mendeleev in 1869 [10] independently presented an organized chart of the elements known at that time that reflected the periodicity of their properties. With these works the atomistic nature of

matter became a cornerstone of modern chemistry.

However, further studies indicated that these elementary particles, still called atoms, are not indivisible constituents of matter. In 1887, Thomson discovered a negatively charged particle when working with a cathodic ray tube [11,12]. This particle was later called *electron* and was thought to be a constituent of atoms. Thus, a new round in the quest about the nature of matter was opened. In 1909, Geiger and Marsden, under the direction of Rutherford, bombarded a sheet of gold foil with alpha rays (positively charged helium atoms). A small percentage of these particles was deflected through larger angles than expected according to the standard model of matter at that time. Rutherford interpreted the gold foil experiment by suggesting that the positive charge and most of the mass of an atom are concentrated in a nucleus at the center of the atom which is surrounded by an electron cloud. This was called the *Rutherford model of the atom* [13]. Later, in 1932, Chadwick reported the existence of a third subatomic particle, which he called *neutron* [14].

The Rutherford model of the atom was further elaborated by his student Bohr who postulated that the electrons travel around the nucleus in circular orbits somehow equivalent to planets around the sun [15]. Even though the so-called *Bohr model* was really successful in the prediction of the spectral emission lines of the hydrogen atom it was doomed by its incompatibility with the Maxwell's theory of electromagnetism. Accordingly, the model included the idea that electrons can only orbit stably at certain distances from the nucleus and thus having definite energies. This introduced the idea of quantized energy levels in the electron orbits. Bohr determined the energy spacing between levels by stating that the angular momentum of the electron is an integer multiple of  $h/2\pi$ , where  $h$  is Planck's constant. The Bohr model was further extended by Sommerfeld to include elliptical orbits [16]. In 1925 Goudsmit and Uhlenbeck proposed that the electrons do not only travel around the nucleus but also rotate around themselves [17] in order to explain ferromagnetism and paramagnetism in atoms. Also in 1925 Pauli gave the foundations of the electronic structure of atoms with more than one electron [18] giving birth to the famous *Pauli's principle* or *exclusion principle*.

The success of the Bohr model, despite its less than satisfying foundation in contemporary physics, motivated a whole generation of theoretical physicists to turn their attention to this problem. In 1925 de Broglie, inspired by Einstein's work on the photoelectric effect [19], proposed the dual nature of matter [20]. The next pioneering step in this quest was the formulation of a new mechanics in matrix equations by Heisenberg [21]. This so-called *matrix mechanics* already had introduced commutators and expectation values but raised skepticism due to its abstract formulation. This was overcome by the alternative formulation from Schrödinger in terms of differential equations that underscored the proximity of quantum mechanics to classical wave mechanics [22].

In theoretical chemistry, so-called *ab initio* (meaning from first principles) methods mostly are based on the many electron Schrödinger equation. The most elementary approximation for the wavefunction is obtained by the Hartree-Fock approach [23]. In this approximation the correlation between electrons of opposite spins is completely neglected. The systematic incorporation of electron correlation in wavefunction methods result in algorithms with computational costs that scale badly with the number of electrons. Hence they become unsuitable for molecules with hundreds of atoms. An interesting alternative to wavefunction methods was born from the ideas of Thomas [24] and Fermi [25]. They suggested use of the electronic density instead of the wavefunction for electronic structure calculations. However, the Thomas-Fermi model failed to give quantitative results of the shell structure of atoms or the bonding in molecules, among other drawbacks. Nevertheless, it established an interesting alternative to wavefunction calculations. Further works by Dirac [26] as well as Wigner and Seitz [27,28] improved the model by introducing a local expression for the exchange potential.

Several years later, Slater introduced the idea of approximating the Hartree-Fock exchange operator by an average local potential [29] based on the free-electron gas model. The result is an exchange potential expressed solely in terms of the electron density  $\rho$ . Using a different derivation, Gaspar [30] obtained the same  $\rho^{1/3}$  form of

Slater's expression but with a prefactor of  $2/3$ . This prefactor was a topic of debate for many years. Further development by Slater and Johnson resulted in the so-called  $X\alpha$  methodology [31], a self-consistent field (SCF) methodology using the muffin-tin approximation and the multiple-scattering method [32,33]. Even though this methodology was developed mainly for solid-state physics applications, it started to be applied to molecules, building a bridge between solid-state physics and chemistry.

In the sixties of the twentieth century, along with the  $X\alpha$  development, another theory arose from the ideas of Thomas and Fermi. With the formulation of the Hohenberg-Kohn theorems [34], a solid theoretical framework for *density functional theory* (DFT) was given. Although this turned DFT into an exact theory, the missing knowledge of the form of the universal Hohenberg-Kohn functional hampered direct applications. In the pioneering papers of Kohn and Sham [35] in 1965 this obstacle was circumvented by the introduction of an artificial non-interacting reference system. In it, the determination of an unknown exchange-correlation (XC) functional replaces the task of determination of the unknown Hohenberg-Kohn functional. However, the approximation of the XC functional turned out to be much easier due to the reduced kinetic energy dependency (in fact, the kinetic energy contribution is often completely neglected in exchange-correlation functionals).

Computationally, the Kohn-Sham method resembles the well-studied Hartree-Fock method. The Kohn-Sham equations can be cast in a similar matrix form as the Roothan-Hall equations [36,37]. Therefore, many algorithms from Hartree-Fock wavefunction calculations can be used in Kohn-Sham calculations. In particular, the linear combination of Gaussian type orbitals (LCGTO) approximation can be used in Kohn-Sham density functional theory calculations. As a result, many, but not all, molecular integrals can be either calculated analytically or reduced to the calculation of an incomplete gamma function [38]. In addition, the use of Gaussians as basis functions allows the implementation of recurrence relations for the molecular integrals, which permits the construction of efficient algorithms for their calculation.

Obviously, there are differences between the Hartree-Fock and the Kohn-Sham methods. The most noticeable one is how they treat the quantum interactions between electrons. While the Hartree-Fock method includes only exchange (which is treated exactly), Kohn-Sham calculations usually include both exchange and correlation but, in the vast majority of cases, with an approximate XC functional. This term usually requires numerical integration techniques which represent another technical difference from LCGTO Hartree-Fock methods. Even though linear scaling algorithms for numerical integration are well established they usually come with large prefactors and, therefore, represent computationally demanding tasks.

With the incorporation of electron correlation, albeit approximately, at the SCF level of theory the Kohn-Sham DFT methodology is well suited for large-scale calculations. To this end, Baerends [40], Sambe, [41], Dunlap [42] and Mintmire [43] introduced auxiliary density fitting techniques. In the framework of LCGTO-DFT the variational fitting of the Coulomb potential has proven most successful to reduce the computational effort in large-scale calculations. More recently, this has been also extended to the calculation of the exchange correlation energy [44], giving birth to the so-called auxiliary density functional theory (ADFT). Even though the numerical integration of exchange-correlation energy and potential are not avoided in ADFT, the use of the auxiliary density reduces the computational effort substantially. In combination with efficient adaptive grid techniques [45] as implemented in the current version of deMon2k [46], the numerical integration of the ADFT exchange-correlation energy and potential is one order of magnitude faster than the corresponding calculation of the analytical three-center electron repulsion integrals. Thus, by its construction, ADFT permits large-scale parallel DFT calculations in reasonable times with the typical accuracy and reliability of *ab initio* methods.

The present work is a contribution to the long-time effort of whole generations of theoretical chemists seeking new methodologies and computational algorithms that allow us to gain deeper insight into the structure and properties of more and more complex systems. The aim of this work is to extend the scope of ADFT by applying asymptotic expansions in the calculation of electrostatic interaction integrals. This

includes the calculation of three-center electron repulsion integrals which represents the current computational bottleneck in the construction of the ADFT Kohn-Sham matrix. The result of this development is to move *ab initio* quantum chemistry to its next stage in which DFT calculations of molecular systems with thousands of atoms become regular applications.

# Chapter 1

## Quantum chemistry fundamentals

### 1.1 The Schrödinger equation

The time-independent, non-relativistic Schrödinger equation is an eigenvalue equation of the form:

$$\hat{H}\Phi(\vec{\tau}) = E\Phi(\vec{\tau}), \quad (1.1)$$

where  $\hat{H}$  is the Hamiltonian operator,  $\Phi$  the wavefunction and  $E$  the total energy of the system. The variable  $\vec{\tau}$  represents the spatial coordinates and spins of all particles in the system [47]. For simplicity, the following equations only treat spatial coordinates and consider all wavefunctions normalized unless otherwise stated. The form of the Hamiltonian operator in atomic units for an isolated molecule with  $N$  electrons and  $M$  nuclei is:

$$\begin{aligned} \hat{H} = & -\frac{1}{2} \sum_i^N \nabla_i^2 - \sum_A^M \frac{1}{2M_A} \nabla_A^2 + \sum_i^N \sum_{j>i}^N \frac{1}{|\vec{r}_i - \vec{r}_j|} - \sum_i^N \sum_A^M \frac{Z_A}{|\vec{r}_i - \vec{R}_A|} + \\ & \sum_A^M \sum_{B>A}^M \frac{Z_A Z_B}{|\vec{R}_A - \vec{R}_B|}, \end{aligned} \quad (1.2)$$

where  $\vec{r}$  and  $\vec{R}$  are the spatial coordinates of electrons and nuclei, respectively. The indices  $i$  and  $j$  denote electrons whereas  $A$  and  $B$  denote nuclei. The atomic mass of nucleus  $A$  is given by  $M_A$  and the corresponding nuclear charge by  $Z_A$ . Respectively,

the terms in the above Hamiltonian operator are: The kinetic energy of the electrons, the kinetic energy of the nuclei, the electrostatic repulsion between electrons, the electrostatic attraction between electrons and nuclei and the electrostatic repulsion between nuclei. Eq. (1.2) can be rewritten as:

$$\hat{H} = \hat{T}_{el} + \hat{T}_{Nu} + \hat{V}_{elel} + \hat{V}_{elNu} + \hat{V}_{NuNu}. \quad (1.3)$$

The term  $\hat{V}_{elNu}$  prevents the separation of the Hamiltonian operator into distinct nuclear and electronic contributions, complicating the solution of the Schrödinger equation. In order to alleviate this problem, we can apply the Born-Oppenheimer approximation [48]. Its semiclassical interpretation assumes that the electronic and nuclear motions can be separated since the nuclei are much more massive than the electrons. Then, the electrons will respond instantaneously to the motion of nuclei so, in terms of the electrons' motion, nuclei can be considered fixed. With this consideration, the Hamiltonian operator is reduced to an electronic operator with an external field:

$$\hat{H}_{el} = \hat{T}_{el} + \hat{V}_{elel} + \hat{V}_{elNu} + \hat{V}_{NuNu}. \quad (1.4)$$

As a consequence, the total wavefunction can be written as an infinite expansion with products of two factors, a complete set of electronic wavefunctions  $\Psi_i$  (with parametric dependence on the nuclear coordinates) and a set of nuclear wavefunctions  $\Theta_i$  (that can be interpreted as expansion coefficients):

$$\Phi(\vec{r}, \vec{R}) = \sum_i^{\infty} \Theta_i(\vec{R}) \Psi_i(\vec{r}; \vec{R}). \quad (1.5)$$

In the adiabatic approximation [49,50] we restrict consideration to one state function, *i.e.*

$$\Phi(\vec{r}, \vec{R}) \approx \Psi(\vec{r}; \vec{R}) \Theta(\vec{R}). \quad (1.6)$$

The corresponding electronic Schrödinger equation is then given by:

$$\hat{H}_{el}\Psi(\vec{r}; \vec{R}) = E_{el}(\vec{R})\Psi(\vec{r}; \vec{R}), \quad (1.7)$$

where the electronic energy,  $E_{el}$ , has also a dependence on the nuclear coordinates. Although the term  $\hat{V}_{NuNu}$  in Eq. (1.4) depends only on nuclear coordinates, it is included in the electronic Hamiltonian operator since, at a fixed nuclear configuration, it only adds a constant that shifts the energy values of Eq. (1.7). Inserting Eq. (1.6) into the Schrödinger equation (1.1) yields:

$$\begin{aligned} (\hat{T}_{Nu} + \hat{H}_{el}) \Psi(\vec{r}; \vec{R}) \Theta(\vec{R}) &= \hat{T}_{Nu}\Psi(\vec{r}; \vec{R}) \Theta(\vec{R}) + \Theta(\vec{R})\hat{H}_{el}\Psi(\vec{r}; \vec{R}) \\ &= \hat{T}_{Nu}\Psi(\vec{r}; \vec{R}) \Theta(\vec{R}) + \Theta(\vec{R})E_{el}(\vec{R})\Psi(\vec{r}; \vec{R}) \\ &= \Theta(\vec{R})\hat{T}_{Nu}\Psi(\vec{r}; \vec{R}) + \Psi(\vec{r}; \vec{R})\hat{T}_{Nu}\Theta(\vec{R}) + \\ &\quad 2(\nabla_M\Psi(\vec{r}; \vec{R}))(\nabla_M\Theta(\vec{R})) + \Theta(\vec{R})E_{el}(\vec{R})\Psi(\vec{r}; \vec{R}) \\ &= E\Psi(\vec{r}; \vec{R})\Theta(\vec{R}), \end{aligned} \quad (1.8)$$

where  $\nabla_M = -\sum_A^M \frac{1}{2M_A} \nabla_A$ . In the Born-Oppenheimer approximation the derivatives of the electronic wavefunction with respect to the nuclear coordinates are neglected. Thus, Eq. (1.8) simplifies to

$$\begin{aligned} (\hat{T}_{Nu} + \hat{H}_{el}) \Psi(\vec{r}; \vec{R}) \Theta(\vec{R}) &= \Psi(\vec{r}; \vec{R})\hat{T}_{Nu}\Theta(\vec{R}) + \Theta(\vec{R})E_{el}(\vec{R})\Psi(\vec{r}; \vec{R}) \\ &= E\Psi(\vec{r}; \vec{R})\Theta(\vec{R}). \end{aligned} \quad (1.9)$$

Multiplying the above equation from the left with  $\Psi^*(\vec{r}; \vec{R})$  and integrating over the electronic coordinates yields

$$(\hat{T}_{Nu} + E_{el}(\vec{R})) \Theta(\vec{R}) = E \Theta(\vec{R}). \quad (1.10)$$

This represents the nuclear Schrödinger equation. The usual procedure to solve Eq. (1.10) is to solve first the electronic Schrödinger equation (1.7), then substitute its energy value into the foregoing nuclear Born-Oppenheimer Schrödinger equation and solve it. Thus, solving Eq. (1.7) for several (fixed) nuclei configurations generates the

potential energy surface on which the molecular nuclei move. It is at this level of theory that the molecular structure concept appears in the quantum mechanical description of matter. For more details on the adiabatic and non-adiabatic forms of the Schrödinger equation we refer the interested reader to more specialized literature [51,52]. Since the main scope of the present work is the solution of the electronic Schrödinger equation, the notation is simplified by dropping the parametric dependence on the nuclear coordinates of the electronic wavefunction.

The development so far is for an isolated molecule. Once the Born-Oppenheimer approximation is applied, it can be stated that since the electronic degrees of freedom are the main variables, they are subject to an *external potential* generated by the nuclei field. In a general situation, such an external potential could be provided not only the nuclei configuration but also from a non-molecular source like an external electromagnetic field. Since this is not the case here, the term

$$v(\vec{r}) = - \sum_A^M \frac{Z_A}{|\vec{r} - \vec{R}_A|} \quad (1.11)$$

will be considered the external potential unless otherwise stated.

Even with the Born-Oppenheimer approximation, the Schrödinger equation cannot be solved analytically for an atom or molecule with two or more electrons. Thus, only approximate solutions are available for most chemical systems of interest. Several methods have been developed for this purpose [53,54], the most relevant being the ones based on the *variational principle* [55]. It states that the energy calculated by a trial wavefunction  $\Psi_t$  is always greater than or equal to the value corresponding to the one calculated by the true ground state wavefunction  $\Psi_0$ , *i.e.*

$$E[\Psi_t] \geq E[\Psi_0]. \quad (1.12)$$

Thus, according to the variational principle, the energy calculated by a trial wavefunction is an upper bound to the real energy of the system.

## 1.2 Density functional theory

For a system with  $N$  electrons, the wavefunction  $\Psi$  depends on  $3N$  spatial variables. Thus, even for very simple molecules the number of variables becomes large. As remarked already, Thomas and Fermi suggested use of the electronic density instead of the wavefunctions to calculate the atomic properties [24,25]. Although the results from the so-called Thomas-Fermi model were inaccurate, it was the precursor of what we now know as *density functional theory* (DFT). The success of DFT lies in the fact that the (one-particle) electronic density,  $\rho(\vec{r})$ , depends only on 3 instead of  $3N$  spatial variables. In terms of the wavefunction, the electronic density is defined as:

$$\rho(\vec{r}) = N \int \dots \int |\Psi(\vec{r}, \vec{r}_2, \dots, \vec{r}_N)|^2 d\vec{r}_2 d\vec{r}_3 \dots d\vec{r}_N. \quad (1.13)$$

Thus, the electronic density is obtained by integrating  $N - 1$  electrons out of the wavefunction. It represents the probability of finding an electron in position  $\vec{r}$  when the other  $N - 1$  electrons are in arbitrary positions. From this equation, it can be noticed that the integration of the electronic density in the whole space returns the number of electrons:

$$\int \rho(\vec{r}) d\vec{r} = N. \quad (1.14)$$

### 1.2.1 Hohenberg-Kohn theorems

DFT was stated in its modern form by Hohenberg and Kohn [34]. It was developed in the framework of solid-state physics but chemistry found it very useful due to its capability of handling many-particle quantum mechanical systems. Hohenberg and Kohn gave the theorems that put DFT in the framework of *ab initio* quantum mechanics methods. The first one arises from the one-to-one mapping of the electronic density with the external potential.

**First Hohenberg-Kohn theorem:** *The external potential  $v(\vec{r})$  is a unique functional of the electronic density,  $\rho(\vec{r})$ , apart from a trivial additive constant.*

So, the electronic density can be taken as the key variable for the calculation of the

ground-state energy of a quantum mechanical system. This is done by introducing a functional dependence of the energy on the electronic density [56,57]:

$$E[\rho] = T_{el}[\rho] + V_{el}[\rho] + \int \rho(\vec{r})v(\vec{r})d\vec{r} \quad (1.15)$$

where  $T_{el}[\rho]$  and  $V_{el}[\rho]$  are the expectation values of the kinetic energy and the electron-electron interaction, respectively, both functionals of the electronic density. The third term is the expectation value of the external potential. The correspondence between  $\rho(\vec{r})$  and  $v(\vec{r})$  is proven by *reductio ad absurdum*. Assume that two different external potentials  $v(\vec{r})$  and  $v'(\vec{r})$  correspond to the same electronic density  $\rho(\vec{r})$ . Two external potentials also correspond to two different Hamiltonian operators,  $\hat{H}$  and  $\hat{H}'$ , and two different solutions of the Schrödinger equation, *i.e.* two different wavefunctions,  $\Psi$  and  $\Psi'$ . However, since both wavefunctions are valid solutions, we can apply one's wavefunction, say  $\Psi'$ , as a trial function for the Hamiltonian operator of the other wavefunction,  $\hat{H}$ . Employing the variational principle according to Eq. (1.12) we then find for the expectation value of the energy:

$$\begin{aligned} E_0 &< \langle \Psi' | \hat{H} | \Psi' \rangle \\ &< \langle \Psi' | \hat{H}' | \Psi' \rangle + \langle \Psi' | \hat{H} - \hat{H}' | \Psi' \rangle \\ &< E'_0 + \langle \Psi' | \hat{H} - \hat{H}' | \Psi' \rangle \\ &< E'_0 + \int \rho(\vec{r}) (v(\vec{r}) - v'(\vec{r})) d\vec{r} \end{aligned} \quad (1.16)$$

The *less-than* sign in the relationship arises because, by construction, the trial wavefunction *is not* the ground-state solution of the Schrödinger equation with  $\hat{H}$  as Hamiltonian operator. Interchanging wavefunction and Hamiltonian operator we find:

$$\begin{aligned} E'_0 &< \langle \Psi | \hat{H}' | \Psi \rangle \\ &< \langle \Psi | \hat{H} | \Psi \rangle + \langle \Psi | \hat{H}' - \hat{H} | \Psi \rangle \\ &< E_0 + \langle \Psi | \hat{H}' - \hat{H} | \Psi \rangle \\ &< E_0 + \int \rho(\vec{r}) (v'(\vec{r}) - v(\vec{r})) d\vec{r} = E_0 - \int \rho(\vec{r}) (v(\vec{r}) - v'(\vec{r})) d\vec{r} \end{aligned} \quad (1.17)$$

Adding both inequalities yields the contradiction:

$$E_0 + E'_0 < E'_0 + E_0. \quad (1.18)$$

This contradiction confirms that knowledge of the ground-state electronic density is sufficient to obtain the ground-state energy of a non-degenerate quantum mechanical system. Thus, the following mapping can be defined based on the first Hohenberg-Kohn theorem:

$$\rho(\vec{r}) \longleftrightarrow N, v(\vec{r}) \longrightarrow \hat{H} \longrightarrow \Psi[\rho] \longrightarrow E[\rho] \quad (1.19)$$

Therefore, the ground-state wavefunction and the corresponding energy can be expressed as functionals of the electronic density:

$$E = E[\rho] \quad ; \quad \Psi = \Psi[\rho]. \quad (1.20)$$

The variational nature of  $E[\rho]$  is established by the second Hohenberg-Kohn theorem.

**Second Hohenberg-Kohn theorem:** *For a positive semi-semidefinite trial density  $\rho_t(\vec{r})$  that integrates to the number of electrons of the system,  $E[\rho_t] \geq E_0$ , where  $E_0$  is the ground state energy of the system.*

The ground-state energy as a functional of the electronic density can be written as:

$$E_0[\rho] = F[\rho] + \int \rho(\vec{r})v(\vec{r})d\vec{r} = \langle \Psi[\rho] | \hat{H} | \Psi[\rho] \rangle \quad (1.21)$$

where  $F[\rho]$  is the universal (and unfortunately unknown) Hohenberg-Kohn functional, given by:

$$F[\rho] = T_{el}[\rho] + V_{el}[\rho] = \langle \Psi[\rho] | \hat{T}_{el} | \Psi[\rho] \rangle + \langle \Psi[\rho] | \hat{V}_{el} | \Psi[\rho] \rangle. \quad (1.22)$$

It is universal because it does not depend on the external potential  $v(\vec{r})$  and, thus, it is system independent. For a well-behaved trial density  $\rho_t$  that is not the ground-state

density, the first Hohenberg-Kohn theorem states that  $\rho_t$  corresponds to a different external potential  $v_t$  and, therefore, to a different Hamiltonian operator  $\hat{H}_t$  and wavefunction  $\Psi_t$ . If we use  $\rho_t$  as the density for the calculation of the ground-state energy, it follows from the variational principle:

$$\begin{aligned} E[\rho_t] &= F[\rho_t] + \int \rho_t(\vec{r})v(\vec{r})d\vec{r} = \langle \Psi_t[\rho] | \hat{H} | \Psi_t[\rho] \rangle > E_0 \text{ if } \rho_t(\vec{r}) \neq \rho(\vec{r}) \\ &= E_0 \text{ if } \rho_t(\vec{r}) = \rho(\vec{r}) \end{aligned} \quad (1.23)$$

This theorem guarantees that one can find the ground-state electronic density by minimizing the energy functional by varying electronic densities. An electronic density different from the non-degenerate ground-state one will always yield a higher energy than the one from the ground-state for a given external potential. Further developments extended the application range of DFT to degenerate ground states and excited states [58,59].

### 1.2.2 The Kohn-Sham method

Since the form of  $F[\rho]$  is unknown, approximations to this functional are needed in order to apply DFT to specific problems. The Thomas-Fermi model and methods deduced from it [60] suggest approximate forms for  $T[\rho]$  and  $V_{el}[\rho]$  that involve the electronic density alone in the calculations. However, these methods do not yield results with chemical accuracy [61], since the formulation of an accurate kinetic energy functional represents an enormous challenge [62,63]. Kohn and Sham [35] suggested an approach that avoids the explicit use of  $T[\rho]$ . To do so, they introduced a fictitious, non-interacting reference system with an antisymmetric wavefunction given by a single Slater determinant. By construction, the density of the non-interacting reference system,  $\rho_s(\vec{r})$ , must be equal to that of the real system:

$$\rho(\vec{r}) \equiv \rho_s(\vec{r}) = \sum_i^{occ} |\psi_i(\vec{r})|^2. \quad (1.24)$$

The upper index of the sum, *occ*, means that the sum goes over the occupied orbitals in the system. Introducing orbitals is seemingly at odds with to the DFT philosophy given by Hohenberg and Kohn, namely to calculate the ground-state energy of a

system without the explicit knowledge of the wavefunction. However, the Kohn-Sham method has been a success since it provides a practical way to implement the DFT methodology in an accurate and simple fashion. The kinetic energy of the reference system,  $T_s[\rho]$ , can then be calculated from the orbitals of this non-interacting system as:

$$T_s[\rho] = \sum_i^{occ} -\frac{1}{2} \langle \psi_i | \nabla^2 | \psi_i \rangle. \quad (1.25)$$

Obviously the quantity  $T_s[\rho]$  is not the kinetic energy  $T_{el}[\rho]$  of the interacting electrons of the real system. There is a correlation term that is neglected due to the non-interacting system *ansatz*. However, this term is rather small [60]. In addition, the explicit form of the non-classical interaction between the electrons is not known. Thus, the form of the universal Hohenberg-Kohn functional in the Kohn-Sham method is given by:

$$F[\rho] = T_{el}[\rho] + V_{el}[\rho] = T_s[\rho] + E_H[\rho] + E_{xc}[\rho], \quad (1.26)$$

where  $E_H[\rho]$  is the energy due to the Coulombic electron repulsion and  $E_{xc}[\rho]$  is the newly introduced *exchange-correlation energy functional* given as:

$$E_{xc}[\rho] = T_{el}[\rho] - T_s[\rho] + V_{el}[\rho] - E_H[\rho]. \quad (1.27)$$

Eq. (1.27) shows that  $E_{xc}[\rho]$  collects all energy contributions of the real system neglected by the non-interacting nature of the reference system, namely the correlation of the kinetic energy and the non-classical contribution of the electron-electron interactions, *i.e.* exchange and correlation. Thus, the Kohn-Sham energy expression takes the form:

$$E[\rho] = T_s[\rho] + \int v(\vec{r})\rho(\vec{r})d\vec{r} + E_H[\rho] + E_{xc}[\rho]. \quad (1.28)$$

At first glance, it seems little has been gained because the form of the exchange-correlation energy functional,  $E_{xc}[\rho]$ , is as unknown as the form of the Hohenberg-Kohn universal functional,  $F[\rho]$ . However, this impression is misleading. By extract-

ing the major part of the kinetic energy from the universal functional, a functional form that permits rather simple approximations is achieved. The most prominent of such approximations is the local density approximation (LDA) in which the exchange energy expression from Dirac [26] is combined with a correlation energy interpolation for the ideal electron gas, *e.g.* the one given by Vosko, Wilk and Nusair [64]. In the generalized gradient approximation (GGA)  $E_{xc}[\rho]$  is approximated by a functional of  $\rho$  and its gradient  $\nabla\rho$ . Examples include BLYP [65,66], BP91 [67,68] and PBE [69]. The hybrid GGAs combine a fraction of exact exchange with the GGA exchange. Examples include B3LYP [70], PBE0 [71] and B97 [72]. Meta-GGAs and hybrid meta-GGAs introduce second-order derivatives of the density or the kinetic energy density to the GGAs. Examples include B98 [73], PKZB [74] and VS98 [75]. Extensive reviews on exchange-correlation functionals are given by Cohen and Handy [76] and by Scuseria and Staroverov [77].

Once a form of the exchange-correlation functional is chosen, one can formulate the equations for the Kohn-Sham method. The variation of Eq. (1.28) subject to the constraints,

$$\langle \psi_i | \psi_j \rangle = \delta_{ij}, \quad (1.29)$$

yields the following set of one-particle equations:

$$\left( -\frac{1}{2}\nabla^2 + v_{\text{eff}}(\vec{r}) \right) \psi_i(\vec{r}) = \epsilon_i \psi_i(\vec{r}). \quad (1.30)$$

Here  $v_{\text{eff}}(\vec{r})$  is the Kohn-Sham effective potential defined by:

$$v_{\text{eff}}(\vec{r}) = \int \frac{\rho(\vec{r}')}{|\vec{r} - \vec{r}'|} d\vec{r}' + v(\vec{r}) + v_{xc}(\vec{r}). \quad (1.31)$$

The newly introduced exchange-correlation potential,  $v_{xc}(\vec{r})$ , is defined as the functional derivative of the exchange-correlation energy:

$$v_{xc}(\vec{r}) = \frac{\delta E_{xc}[\rho]}{\delta \rho(\vec{r})}. \quad (1.32)$$

The solution of the Kohn-Sham equations in the framework of the linear combination of Gaussian type orbitals approximation will be discussed in the next chapter.



# Chapter 2

## Methodology for DFT calculations

### 2.1 Linear combination of atomic orbitals

Today, the most common computational approach for first-principle electronic structure calculations is *molecular orbital theory*. It states that when a molecule is formed, orbitals from individual atoms combine in order to form orbitals that cover the whole molecule. So, the individuality of atomic orbitals (AO) is lost and the molecule as a whole contains a set of molecular orbitals (MO). Mathematically, MOs are represented as a *linear combination of atomic orbitals* (LCAO):

$$\psi_i(\vec{r}) = \sum_{\mu} c_{\mu i} \mu(\vec{r}) \quad (2.1)$$

where  $\psi_i(\vec{r})$  is a MO,  $\mu(\vec{r})$  is an AO or, more generally, a basis function and  $c_{\mu i}$  is the MO coefficient. The sum runs over the number of AOs used for the calculation.

#### 2.1.1 Gaussian type orbitals

Different kind of functions can be employed to represent AOs. One of the most used is the Gaussian type function, proposed by Boys in 1950 [78]. The great advantage of this kind of functions is that the product of two Gaussians yields another Gaussian centered between the original ones. This eases the calculation of molecular integrals since it reduces all kinds of multi-center integrals to one-center integrals. In quantum

chemistry it is common to call Gaussian functions *Gaussian type orbitals*, GTOs, since they are representing orbitals. An unnormalized primitive Cartesian GTO is defined as follows:

$$g(\mathbf{a}, \vec{r}) = (x - A_x)^{a_x} (y - A_y)^{a_y} (z - A_z)^{a_z} e^{-\zeta(\vec{r}-\vec{A})^2}. \quad (2.2)$$

One of the disadvantages of GTOs is that they do not represent important characteristics of hydrogen-like orbitals, like function decay and cusp. In order to mitigate the impact of these deficiencies, GTOs are commonly used in contracted form:

$$\mathbf{a}(\vec{r}) = (x - A_x)^{a_x} (y - A_y)^{a_y} (z - A_z)^{a_z} \sum_k^{K_a} d_k e^{-\zeta_k(\vec{r}-\vec{A})^2}. \quad (2.3)$$

A contracted GTO is defined by its center  $\vec{A}$ , the triad of non-negative integers  $(a_x, a_y, a_z)$  related to the angular momentum index of the function, exponents  $\zeta_k$ , contraction degree  $K_a$  and contraction coefficients  $d_k$ . In deMon2k [46] contracted atom-centered Cartesian GTOs are used as basis functions for the so-called *linear combination of Gaussian type orbitals* (LCGTO) approximation. Other types of GTOs can be defined. A review on GTOs is given by Saunders in Ref. [79].

### 2.1.2 The LCGTO Kohn-Sham method

For the sake of simplicity, the following part of the work considers a closed-shell electronic configuration. Generalizations to open-shell systems can be found in Refs. [80–82]. When the LCGTO expansion in Eq. (2.1) using atomic orbitals of the form in Eq. (2.3) is applied to the definition of Kohn-Sham orbitals in Eq. (1.24), the form of the density,  $\rho(\vec{r})$ , is given by:

$$\rho(\vec{r}) = 2 \sum_i^{occ} |\psi_i(\vec{r})|^2 = 2 \sum_i^{occ} \sum_{a,b} c_{ai} c_{bi} \mathbf{a}(\vec{r}) \mathbf{b}(\vec{r}) = \sum_{a,b} P_{ab} \mathbf{a}(\vec{r}) \mathbf{b}(\vec{r}), \quad (2.4)$$

where  $\mathbf{a}(\vec{r})$  and  $\mathbf{b}(\vec{r})$  are orbital basis functions and  $P_{ab}$  is an element of the (closed-shell) density matrix defined as:

$$P_{ab} = 2 \sum_i^{occ} c_{ai} c_{bi}. \quad (2.5)$$

Using GTOs and the density as defined previously, the Kohn-Sham energy expression in Eq. (1.28) becomes:

$$E = \sum_{a,b} P_{ab} H_{ab} + \frac{1}{2} \sum_{a,b} \sum_{c,d} P_{ab} P_{cd} \langle \mathbf{ab} || \mathbf{cd} \rangle + E_{xc}[\rho], \quad (2.6)$$

where

$$H_{ab} = -\frac{1}{2} \langle \mathbf{a} | \nabla^2 | \mathbf{b} \rangle - \sum_A \left\langle \mathbf{a} \left| \frac{Z_A}{|\vec{r} - \vec{A}|} \right| \mathbf{b} \right\rangle \quad (2.7)$$

and

$$\langle \mathbf{ab} || \mathbf{cd} \rangle = \iint \frac{\mathbf{a}(\vec{r}_1) \mathbf{b}(\vec{r}_1) \mathbf{c}(\vec{r}_2) \mathbf{d}(\vec{r}_2)}{|\vec{r}_1 - \vec{r}_2|} d\vec{r}_1 d\vec{r}_2. \quad (2.8)$$

$H_{ab}$  is an element of the core Hamiltonian matrix that collects all the one-electron contributions to the energy. The two-electron integral in Eq. (2.8) is called an *electron repulsion integral* (ERI). The double bar  $||$  represents the Coulomb operator  $1/|\vec{r}_1 - \vec{r}_2|$ . The functions in the bra depend on electron coordinate  $\vec{r}_1$  and the functions in the ket depend on electron coordinate  $\vec{r}_2$ .

For a given number of basis functions  $N_{bas}$  the computation of  $H_{ab}$  scales formally as  $N_{bas}^2$ . The ERI calculation scales formally as  $N_{bas}^4$ . The calculation of  $E_{xc}[\rho]$  usually requires numerical integration on a grid and, therefore, has a formal scaling of  $N_{bas}^2 \times G$ , where  $G$  is the number of grid points. This is the reason why the ERI calculation for large systems is the computationally most demanding task in the energy calculation. Of course, a lot of work has been devoted to the development of efficient algorithms for the ERI calculation (including the present effort). In the following chapters we will present methodologies that reduce the computational burden of ERI calculations.

The derivation of the LCGTO-Kohn-Sham equations follows the same line as for the LCGTO-Hartree-Fock equations. As a result, the Kohn-Sham equation system is very similar to the commonly known Roothaan-Hall equation system [36,37]. The difference is in the electronic interaction part. As mentioned already, in contrast with the structure of the Hartree-Fock equations, the Kohn-Sham equations include an exchange-correlation term which almost always must be approximated. Distinct from the Hartree-Fock case, the great majority of those exchange-correlation approximations do not cancel self-interaction from the Hartree energy completely, so that residual self-interaction frequently is a matter of concern in practical Kohn-Sham calculations. The Kohn-Sham equations are derived by minimizing Eq. (2.6) subject to the constraint of orthonormal molecular orbitals from Eq. (1.29). This constraint takes the following form in the LCGTO approach:

$$\langle \psi_i | \psi_j \rangle = \sum_{a,b} c_{ai} c_{bj} \langle \mathbf{a} | \mathbf{b} \rangle \equiv \sum_{a,b} c_{ai} c_{bj} S_{ab} = \delta_{ij}, \quad (2.9)$$

where  $S_{ab}$  is an element of the overlap matrix. The corresponding Lagrange function takes the form:

$$\mathcal{L} = E - 2 \sum_{i,j} \lambda_{ij} \left( \sum_{a,b} c_{ai} c_{bj} S_{ab} - \delta_{ij} \right), \quad (2.10)$$

with  $\lambda_{ij}$  being undetermined Lagrange multipliers and  $E$  the Kohn-Sham energy given by Eq. (2.6). The variation of the Lagrange function with respect to the MO coefficients yields:

$$\frac{1}{4} \frac{\partial \mathcal{L}}{\partial c_{ai}} = \sum_b \left( H_{ab} + \sum_{c,d} P_{cd} \langle \mathbf{a} \mathbf{b} | | \mathbf{c} \mathbf{d} \rangle + \langle \mathbf{a} | v_{xc} | \mathbf{b} \rangle - \sum_j \lambda_{ij} S_{ab} \right) c_{bi}, \quad (2.11)$$

where the term involving the exchange-correlation potential,  $v_{xc}$ , was developed as follows:

$$\frac{\partial E_{xc}[\rho]}{\partial c_{ai}} = \int \frac{\delta E_{xc}[\rho]}{\delta \rho(\vec{r})} \frac{\partial \rho(\vec{r})}{\partial c_{ai}} d\vec{r} = \sum_b \langle \mathbf{a} | v_{xc} | \mathbf{b} \rangle c_{bi}. \quad (2.12)$$

Solving Eq. (2.11) yields the LCGTO Kohn-Sham equations which, written in matrix form, are:

$$\mathbf{K}\mathbf{C} = \mathbf{S}\mathbf{C}\boldsymbol{\lambda} \quad (2.13)$$

with  $\mathbf{S}$  being the overlap matrix,  $\mathbf{C}$  a matrix built from the molecular orbital coefficients,  $\boldsymbol{\lambda}$  the matrix of undetermined Lagrange multipliers and  $\mathbf{K}$  the Kohn-Sham matrix with elements given by:

$$K_{ab} = H_{ab} + \sum_{c,d} P_{cd} \langle \mathbf{a}\mathbf{b} | | \mathbf{c}\mathbf{d} \rangle + \langle \mathbf{a} | v_{xc} | \mathbf{b} \rangle \quad (2.14)$$

Since the electronic density is invariant under unitary transformation of the occupied MOs, it is possible and convenient to choose a set of molecular orbitals for which the off-diagonal elements of the undetermined Lagrange multipliers vanish. Such MOs are called *canonical MOs* and the corresponding equations are called *canonical Kohn-Sham equations*. In matrix form, these equations are:

$$\mathbf{K}\mathbf{c} = \mathbf{S}\mathbf{c}\boldsymbol{\epsilon}, \quad (2.15)$$

where  $\mathbf{c}$  collects the canonical molecular orbital coefficients and  $\boldsymbol{\epsilon}$  is a diagonal matrix of Lagrange multipliers that represent the Kohn-Sham orbital energies.

## 2.2 Variational fitting of the Coulomb potential

An important approach for the ERI calculation is the so-called *variational fitting of the Coulomb potential*, VFCP [39]. It was initialized by Baerends *et al.* who proposed the use of auxiliary functions to represent the electronic density in the two-electron Coulomb integrals [40]. Later, Sambe and Felton suggested the use of contracted Gaussian functions for the electronic density fitting [41]. Dunlap *et al.* developed a variational fitting procedure for the electrostatic potential [42,43] that is particularly well suited for density fitting in Kohn-Sham DFT implementations employing the LCAO approximation. The variational fitting reduces the formal  $N^4$  scaling of the ERI calculation in Kohn-Sham DFT to  $N^2 \times M$ , where  $M$  is the number of auxi-

liary functions. This reduction of the formal scaling is achieved by transforming the underlying ERIs from four-center to three-center integrals. In deMon2k the VFCEP is implemented by the minimization of the following error:

$$\mathcal{E} = \frac{1}{2} \iint \frac{[\rho(\vec{r}_1) - \tilde{\rho}(\vec{r}_1)][\rho(\vec{r}_2) - \tilde{\rho}(\vec{r}_2)]}{|\vec{r}_1 - \vec{r}_2|} d\vec{r}_1 d\vec{r}_2. \quad (2.16)$$

The approximate density is defined by a linear combination of auxiliary functions:

$$\tilde{\rho}(\vec{r}) = \sum_{\bar{c}} x_{\bar{c}} \bar{c}(\vec{r}), \quad (2.17)$$

where  $x_{\bar{c}}$  is a density fitting coefficient and  $\bar{c}$  an auxiliary function. As auxiliary functions we employ here primitive Hermite Gaussian type functions (HGTF). These functions differ from the Cartesian GTOs in the form of the polynomial prefactor of the exponential function. An unnormalized primitive Hermite Gaussian auxiliary function has the form:

$$\begin{aligned} \bar{c}(\vec{r}) &= \left( \frac{\partial}{\partial C_x} \right)^{\bar{c}_x} \left( \frac{\partial}{\partial C_y} \right)^{\bar{c}_y} \left( \frac{\partial}{\partial C_z} \right)^{\bar{c}_z} e^{-\zeta_{\bar{c}}(\vec{r}-\vec{C})^2} \\ &= \lambda_{\bar{c}_x}(x - A_x) \lambda_{\bar{c}_y}(y - A_y) \lambda_{\bar{c}_z}(z - A_z) e^{-\zeta_{\bar{c}}(\vec{r}-\vec{C})^2} \end{aligned} \quad (2.18)$$

with

$$\lambda_n(x) = \zeta_{\bar{c}}^{(n/2)} H_n(\sqrt{\zeta_{\bar{c}}}x), \quad (2.19)$$

where  $H_n$  is a Hermite polynomial of degree  $n$ . An auxiliary function is defined by its center  $\vec{C}$ , the triad of non-negative integers  $(\bar{c}_x, \bar{c}_y, \bar{c}_z)$  related to the angular momentum index of the function and exponent  $\zeta_{\bar{c}}$ .

The current deMon2k implementation uses primitive HGTF to fit the density since efficient recurrence relations can be derived for integrals involving this kind of functions [83,84]. In addition, it has been shown that the use of primitive Hermite Gaussian auxiliary functions with the same exponents but different angular momentum indices reduces the computational effort considerably without affecting the quality of the calculation [84,85]. Therefore, auxiliary functions may be grouped together in sets, that

consist of different shells sharing the same exponent. For example, a *s* set contains one shell with one auxiliary function, a *spd* set contains three shells with a total of ten functions, namely one *s*, three *p* and six *d* functions, and a *spdfg* set contains five shells with a total of thirty-five functions, namely one *s*, three *p*, six *d*, ten *f* and fifteen *g* functions.

Applying the LCGTO expansion in the expression for the error  $\mathcal{E}$ , Eq. (2.16), yields:

$$\begin{aligned}\mathcal{E} &= \frac{1}{2}\langle\rho-\tilde{\rho}|\rho-\tilde{\rho}\rangle = \frac{1}{2}\langle\rho|\rho\rangle - \langle\rho|\tilde{\rho}\rangle + \frac{1}{2}\langle\tilde{\rho}|\tilde{\rho}\rangle \\ &= \frac{1}{2}\sum_{a,b}\sum_{c,d}P_{ab}P_{cd}\langle\mathbf{ab}|\mathbf{cd}\rangle - \sum_{a,b}\sum_{\bar{c}}P_{ab}\langle\mathbf{ab}|\bar{\mathbf{c}}\rangle x_{\bar{c}} + \frac{1}{2}\sum_{\bar{c},\bar{d}}x_{\bar{c}}x_{\bar{d}}\langle\bar{\mathbf{c}}|\bar{\mathbf{d}}\rangle\end{aligned}\quad (2.20)$$

Since  $\mathcal{E} \geq 0$  holds (see appendix A) the following inequality is obtained:

$$\frac{1}{2}\sum_{a,b}\sum_{c,d}P_{ab}P_{cd}\langle\mathbf{ab}|\mathbf{cd}\rangle \geq \sum_{a,b}\sum_{\bar{c}}P_{ab}\langle\mathbf{ab}|\bar{\mathbf{c}}\rangle x_{\bar{c}} - \frac{1}{2}\sum_{\bar{c},\bar{d}}x_{\bar{c}}x_{\bar{d}}\langle\bar{\mathbf{c}}|\bar{\mathbf{d}}\rangle\quad (2.21)$$

Substituting Eq. (2.21) into the energy expression, Eq. (2.6), yields:

$$E = \sum_{a,b}P_{ab}H_{ab} + \sum_{a,b}\sum_{\bar{c}}P_{ab}\langle\mathbf{ab}|\bar{\mathbf{c}}\rangle x_{\bar{c}} - \frac{1}{2}\sum_{\bar{c},\bar{d}}x_{\bar{c}}x_{\bar{d}}\langle\bar{\mathbf{c}}|\bar{\mathbf{d}}\rangle + E_{xc}[\rho],\quad (2.22)$$

where  $E$  is now the energy for the VFCP implementation. This form of the Kohn-Sham energy is called the *BASIS* approach in deMon2k since the basis set density,  $\rho(\vec{r})$ , is used to calculate the exchange-correlation energy. The corresponding Kohn-Sham matrix for the BASIS approach is given by:

$$K_{ab} = H_{ab} + \sum_{\bar{c}}\langle\mathbf{ab}|\bar{\mathbf{c}}\rangle x_{\bar{c}} + \langle\mathbf{a}|v_{xc}|\mathbf{b}\rangle.\quad (2.23)$$

The fitting coefficients  $x_{\bar{c}}$  are obtained by minimizing  $\mathcal{E}$ :

$$\frac{\partial\mathcal{E}}{\partial x_{\bar{m}}} = -\sum_{a,b}P_{ab}\langle\mathbf{ab}|\bar{\mathbf{m}}\rangle + \sum_{\bar{l}}x_{\bar{l}}\langle\bar{\mathbf{l}}|\bar{\mathbf{m}}\rangle = 0 \quad \forall \quad \bar{\mathbf{m}}\quad (2.24)$$

For the efficient calculation of these newly introduced three-center ERIs integral recurrence relations have been developed [84,86]. In order to simplify the notation, the matrix form of this set of  $\bar{m}$  equations is used. To do so, we introduce the Coulomb matrix  $\mathbf{G}$  as

$$\mathbf{G} = \begin{pmatrix} \langle \bar{\mathbf{1}} | \bar{\mathbf{1}} \rangle & \langle \bar{\mathbf{1}} | \bar{\mathbf{2}} \rangle & \cdots & \langle \bar{\mathbf{1}} | \bar{\mathbf{m}} \rangle \\ \langle \bar{\mathbf{2}} | \bar{\mathbf{1}} \rangle & \langle \bar{\mathbf{2}} | \bar{\mathbf{2}} \rangle & \cdots & \langle \bar{\mathbf{2}} | \bar{\mathbf{m}} \rangle \\ \vdots & \vdots & \ddots & \vdots \\ \langle \bar{\mathbf{m}} | \bar{\mathbf{1}} \rangle & \langle \bar{\mathbf{m}} | \bar{\mathbf{2}} \rangle & \cdots & \langle \bar{\mathbf{m}} | \bar{\mathbf{m}} \rangle \end{pmatrix}, \quad (2.25)$$

and the Coulomb vector  $\mathbf{J}$  as:

$$\mathbf{J} = \begin{pmatrix} \sum_{a,b} P_{ab} \langle \mathbf{ab} | \bar{\mathbf{1}} \rangle \\ \sum_{a,b} P_{ab} \langle \mathbf{ab} | \bar{\mathbf{2}} \rangle \\ \vdots \\ \sum_{a,b} P_{ab} \langle \mathbf{ab} | \bar{\mathbf{m}} \rangle \end{pmatrix}. \quad (2.26)$$

Rearranging Eq. (2.24) the following inhomogeneous equation is obtained:

$$\mathbf{G}\mathbf{x} = \mathbf{J}. \quad (2.27)$$

One obvious solution of Eq. (2.27) is

$$\mathbf{x} = \mathbf{G}^{-1}\mathbf{J}. \quad (2.28)$$

When  $\mathbf{G}$  is normalized with respect to the Coulomb norm (as is done in deMon2k),  $0 < G_{\bar{i}\bar{m}} \leq 1$  holds. Despite this bracketing  $\mathbf{G}$  can become ill-conditioned if large auxiliary function sets are used and its inversion can become numerically unstable [87]. An efficient and stable algorithm for the solution of Eq. (2.27) is given by Domínguez in Refs. [88,89].

## 2.3 Auxiliary density functional theory

When the VFCP is applied, the computational bottleneck in the construction of the Kohn-Sham matrix is the numerical integration for the calculation of the exchange-correlation potential. Köster *et al.* implemented the use of auxiliary functions in the calculation of the exchange-correlation potential,  $v_{xc}$ , and showed that one can obtain improved performance at the cost of increasing the auxiliary functions angular momentum index [44]. They named the whole implementation *auxiliary density functional theory*, ADFT. When the approximate density is used for the evaluation of  $v_{xc}$  then it is essential that  $\tilde{\rho}(\vec{r}) > 0$  and integrates to the number of electrons. The normalization to the number of electrons can be included but even without this the number of electrons is conserved to a high degree. In fact, the current version of deMon2k does not include such normalization. The introduction of the positive definiteness of the approximate density,  $\tilde{\rho}(\vec{r})$ , is less straightforward. In principle it is possible to define an alternative fitting of the Coulomb potential that guarantees positive definite auxiliary densities. However, this has been so far not explored due to its cumbersome implementation. A more practical approach involves fine adjustments to the auxiliary basis [90] or screening of improper points on the numerical grid. In deMon2k the latter is used. Grid points with negative  $\tilde{\rho}(\vec{r})$  values are simply screened out. Because these points are very rare due to the self-adjustment of the variational fitting [91] the algorithm forces the variational fitting away from spurious negative auxiliary densities by an energy penalty. Thus, both basic conditions for the approximate density can be fulfilled, at least approximately, without changing the computationally advantageous implementation structure of the VFCP.

When using  $\tilde{\rho}(\vec{r})$  in the calculation of  $v_{xc}$  and, therefore,  $E_{xc}$ , the Kohn-Sham energy expression takes the form:

$$E = \sum_{a,b} P_{ab} H_{ab} + \sum_{a,b} \sum_{\bar{c}} P_{ab} \langle \mathbf{a} \mathbf{b} | | \bar{\mathbf{c}} \rangle x_{\bar{c}} - \frac{1}{2} \sum_{\bar{c}, \bar{d}} x_{\bar{c}} x_{\bar{d}} \langle \bar{\mathbf{c}} | | \bar{\mathbf{d}} \rangle + E_{xc}[\tilde{\rho}]. \quad (2.29)$$

This is the so-called *AUXIS* approach, where the name indicates that the approximate density, given by auxiliary functions, is used for the calculation of the exchange-correlation contributions. This is the default in deMon2k calculations. The correspon-

ding Kohn-Sham matrix elements are given by:

$$K_{ab} = H_{ab} + \sum_{\bar{c}} \langle \mathbf{ab} | \bar{\mathbf{c}} \rangle x_{\bar{c}} + \frac{\partial E_{xc}[\tilde{\rho}]}{\partial P_{ab}}. \quad (2.30)$$

To further proceed, we now show the calculation of the exchange-correlation contribution to the Kohn-Sham matrix assuming a local functional:

$$\frac{\partial E_{xc}[\tilde{\rho}]}{\partial P_{ab}} = \int \frac{\delta E_{xc}[\tilde{\rho}]}{\delta \tilde{\rho}(\vec{r})} \frac{\partial \tilde{\rho}(\vec{r})}{\partial P_{ab}} d\vec{r} = \sum_{\bar{c}} \frac{\partial x_{\bar{c}}}{\partial P_{ab}} \int v_{xc}[\tilde{\rho}] \bar{\mathbf{c}}(\vec{r}) d\vec{r}, \quad (2.31)$$

with

$$v_{xc}[\tilde{\rho}] \equiv \frac{\delta E_{xc}[\tilde{\rho}]}{\delta \tilde{\rho}(\vec{r})}. \quad (2.32)$$

The extension to other "pure" density functionals, *e.g.* the generalized gradient approximation (GGA), is straightforward. Simply the approximated density and its derivatives have to be inserted into the corresponding exchange-correlation potential expression. From Eqs. (2.26) and (2.28) we obtain:

$$\frac{\partial x_{\bar{c}}}{\partial P_{ab}} = \sum_{\bar{l}} G_{\bar{c}\bar{l}}^{-1} \langle \bar{\mathbf{l}} | \mathbf{ab} \rangle. \quad (2.33)$$

With this, Eq. (2.31) can be formulated as:

$$\frac{\partial E_{xc}[\tilde{\rho}]}{\partial P_{ab}} = \sum_{\bar{c}, \bar{l}} \langle \mathbf{ab} | \bar{\mathbf{c}} \rangle G_{\bar{c}\bar{l}}^{-1} \langle \bar{\mathbf{l}} | v_{xc} \rangle \quad (2.34)$$

For convenience of notation, we now introduce the exchange-correlation coefficients,  $z_{\bar{c}}$ , defined as:

$$z_{\bar{c}} = \sum_{\bar{l}} G_{\bar{c}\bar{l}}^{-1} \langle \bar{\mathbf{l}} | v_{xc} \rangle. \quad (2.35)$$

These coefficients are calculated from numerical integrals  $\langle \bar{\mathbf{1}} | v_{xc} \rangle$  and depend on the electron spin. Thus, the final form of the Kohn-Sham matrix is given by:

$$K_{ab} = H_{ab} + \sum_{\bar{c}} \langle \mathbf{ab} | | \bar{\mathbf{c}} \rangle (x_{\bar{c}} + z_{\bar{c}}). \quad (2.36)$$

It is important to note that the Coulomb fitting coefficients entering Eq. (2.35) via the  $v_{xc}[\tilde{\rho}]$  calculation must be taken unaltered from Eq. (2.28). However, this is not mandatory for the calculation of the Coulomb contribution to energy. Therefore SCF stabilization and acceleration techniques like density mixing [92,93] or the direct inversion in the iterative subspace (DIIS) [94,95] are restricted to the Coulomb fitting coefficients or density matrix elements and must leave the exchange-correlation fitting coefficients untouched.

The result of this implementation is the reduction of the computational effort in the calculation of the exchange-correlation terms in the Kohn-Sham matrix. The consequence is that ERIs become once again the computational bottleneck for the Kohn-Sham matrix construction. The following chapters present a new solution to this bottleneck.



# Chapter 3

## Molecular integral evaluation

This chapter discusses the evaluation of molecular integrals of interest for the development of this work. For a detailed review on the calculation methods of these and other integrals, see chapter 9 of Ref. [38].

### 3.1 Notation

As stated in chapter 2,  $\mathbf{a}$  and  $\mathbf{b}$  denote basis functions and  $\bar{\mathbf{c}}$  denotes an auxiliary function. In agreement with the notation for the angular momentum quantum number in quantum mechanics,  $\mathbf{s}$  and  $\bar{\mathbf{s}}$  will represent basis and auxiliary functions with angular momentum index 0,  $\mathbf{p}_i$  and  $\bar{\mathbf{p}}_i$  will represent basis and auxiliary functions with angular momentum index 1 in the  $i$ -component,  $i$  being  $x$ ,  $y$  or  $z$ , and so on.

In general a modified Dirac notation is used for the molecular integrals. In the case of ERIs, a notation similar to the one of Mulliken is used wherein the double bar  $||$  represents the Coulomb operator for two electrons,  $1/|\vec{r}_1 - \vec{r}_2|$ . The basis functions are usually contracted GTOs and their integrals are denoted by angle brackets  $\langle \rangle$ . In the case of primitive GTOs their integrals will be denoted by brackets  $[ ]$ . The auxiliary functions are always primitive HGTF and their integral symbols usually depend on the ones for the basis functions with which they are to be integrated. The number of functions in an integral will be also named after the number of centers involved in it, *e.g.* an overlap integral  $\langle \mathbf{a} | \mathbf{b} \rangle$  involves two functions, so in general it is a two-center

integral.

During the explanation of the integral calculation algorithms, recurrence relations between integrals of lower and higher angular momentum indices will be shown. When such relations are depicted in equations and diagrams, the function symbols  $\mathbf{a}$  and  $\bar{\mathbf{c}}$  will also act as a representation of the angular momentum index triads  $(a_x, a_y, a_z)$  and  $(\bar{c}_x, \bar{c}_y, \bar{c}_z)$ , respectively, in order to avoid lengthy forms of the recurrence relations. Increase and decrease of the angular momentum index of basis functions will be represented by  $\mathbf{a} + \mathbf{1}_i$  and  $\mathbf{a} - \mathbf{1}_i$ , respectively. For example,  $\mathbf{a} + \mathbf{1}_x$  represents an increment by unit in the  $x$ -component of the angular momentum index of  $\mathbf{a}$ . Thus, the angular momentum index triad of  $\mathbf{a} + \mathbf{1}_x$  is  $(a_x + 1, a_y, a_z)$ . Equivalent representations will be used for the increase and decrease of the angular momentum index of auxiliary functions  $\bar{\mathbf{c}}$ . Nuclear centers will be represented as vectors with capital letters. For example, the nuclear center  $\vec{A}$  has components  $(A_x, A_y, A_z)$ . Electron coordinates will be represented by  $\vec{r}$  with components  $(x, y, z)$ .

## 3.2 The Gaussian product theorem

As mentioned in chapter 2 a very important property of GTOs is given by the *Gaussian product theorem* which states that the product of two GTOs located at centers

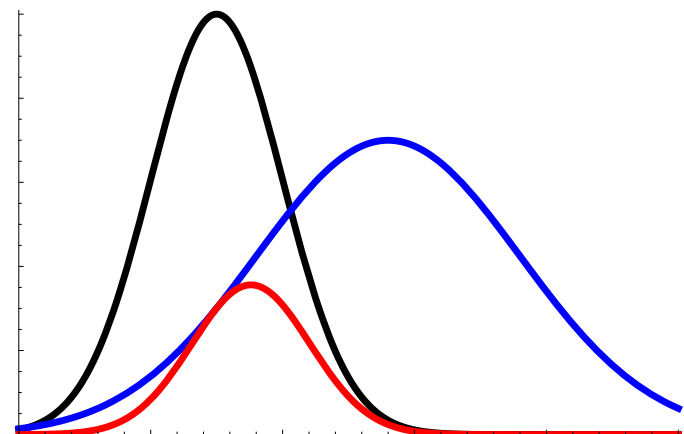


Figure 3.1: The Gaussian product theorem. The product of two Gaussian functions (blue and black) results in a third Gaussian function (red).

$\vec{A}$  and  $\vec{B}$  is itself a GTO multiplied by a factor related to the centers of the original GTOs and located at a point  $\vec{P}$  along the line that connects  $\vec{A}$  and  $\vec{B}$  (see Figure 3.1)

$$e^{-\zeta_a(\vec{r}-\vec{A})^2} e^{-\zeta_b(\vec{r}-\vec{B})^2} \equiv \kappa_{AB} e^{-\zeta_p(\vec{r}-\vec{P})^2}, \quad (3.1)$$

where

$$\zeta_p = \zeta_a + \zeta_b, \quad \vec{P} = \frac{\zeta_a \vec{A} + \zeta_b \vec{B}}{\zeta_p}, \quad \xi = \frac{\zeta_a \zeta_b}{\zeta_p} \quad \text{and} \quad \kappa_{AB} = e^{-\xi(\vec{A}-\vec{B})^2}. \quad (3.2)$$

The successive application of the Gaussian product theorem allows the transformation of multiple Gaussian products in one-center functions. Thus, all integrals involving Gaussian products alone can be turned into one-center integrals.

### 3.3 Overlap integrals

Formulas for the calculation of overlap integrals over Cartesian GTOs were given by several authors [78,96,97], more recently using efficient recurrence relations by Obara and Saika (OS) [98]. A two-center overlap integral between primitive GTOs has the form

$$[\mathbf{a}|\mathbf{b}] = \int \mathbf{a}(\vec{r})\mathbf{b}(\vec{r})d\vec{r}. \quad (3.3)$$

When contracted GTOs are used, the overlap integral reads

$$\langle \mathbf{a}|\mathbf{b} \rangle = \sum_k^{K_a} \sum_l^{K_b} d_k d_l [\mathbf{a}_k|\mathbf{b}_l], \quad (3.4)$$

where the subscript in the orbitals in the primitive integral on the right-hand side of Eq. (3.4) indicates that different exponents occur in the contraction but the orbitals have the same center and angular momentum index. The pathway diagram for the calculation of the overlap integrals, a simplification of the one in Ref. [99], is depicted in Figure 3.2. The diagram is read from the lower-left corner to the upper-right corner, where the target overlap integral appears. The vertical arrow denotes the contraction step whereas the horizontal arrows denote transformation steps as described below.

$$\begin{array}{c}
\langle \mathbf{s} | \mathbf{s} \rangle_{(u,v)} \xrightarrow{\mathbf{V}} \langle \mathbf{a} | \mathbf{s} \rangle \xrightarrow{\mathbf{H}} \langle \mathbf{a} | \mathbf{b} \rangle \\
\uparrow \mathbf{C} \\
[\mathbf{s} | \mathbf{s}]
\end{array}$$

Figure 3.2: Pathway diagram for the calculation of the overlap integrals.

In general, the function on the left of the integral is centered on  $\vec{A} = (A_x, A_y, A_z)$  and the function on the right is centered on  $\vec{B} = (B_x, B_y, B_z)$ . The basic overlap integrals are between primitive  $s$  functions on  $\vec{A}$  and  $\vec{B}$ :

$$[\mathbf{s} | \mathbf{s}] = \left( \frac{\pi}{\zeta_p} \right)^{\frac{3}{2}} \kappa_{AB}, \quad (3.5)$$

where  $\kappa_{AB}$  is given in Eq. (3.2). In order to avoid applying transformation relations on primitive integrals, the contraction step is performed as soon as possible in the integral calculation. A consequence of this early contraction is the need of scaled integrals in the following step. Scaled integrals are contracted integrals in which each term of the contraction has a pre-factor which depends on the exponents of the functions in the primitive integral. The scaled integrals have the following form

$$\langle \mathbf{s} | \mathbf{s} \rangle_{(u,v)} = \sum_k^{K_a} \sum_l^{K_b} d_k d_l \frac{\zeta_l^u}{(\zeta_k + \zeta_l)^v} [\mathbf{s}_k | \mathbf{s}_l], \quad (3.6)$$

where  $\zeta_k$  and  $\zeta_l$  are the exponents of the primitive functions  $\mathbf{s}_k$  and  $\mathbf{s}_l$ , respectively, and the subscript  $(u, v)$  of the scaled integral indicates the power of the exponents in such pre-factor. In the following step the angular momentum index is built up on center  $\mathbf{a}$  (left bra side) employing the vertical recurrence relation (V) from Obara and Saika [98]

$$\langle \mathbf{a} + \mathbf{1}_i | \mathbf{s} \rangle_{(u,v)} = (B_i - A_i) \langle \mathbf{a} | \mathbf{s} \rangle_{(u+1,v+1)} + \frac{N_i(\mathbf{a})}{2} \langle \mathbf{a} - \mathbf{1}_i | \mathbf{s} \rangle_{(u,v+1)}. \quad (3.7)$$

Here  $i$  stands for  $x, y$ , or  $z$ ,  $A_i$  and  $B_i$  are the corresponding components of the vectors which define the orbital centers and  $N_i(\mathbf{a})$  is a function that returns the

value of the angular momentum index  $i$  element of the function  $\mathbf{a}$ , e.g.  $N_i(\mathbf{1}_j)$  is equivalent to Kronecker's delta  $\delta_{ij}$ . Different from the original formulation of Obara and Saika, the vertical recurrence relation in Eq. (3.7) contains scaled integrals (due to the early contraction in the pathway diagram given in Fig. 3.2) and only two terms because only the  $\mathbf{a}$  angular momentum index is increased. The results of the vertical recurrence steps are overlap integrals that possess the angular momentum index of both functions at the center of orbital  $\mathbf{a}$ . The angular momentum index can be shifted with the horizontal recurrence relation ( $H_1$ ) [100] to obtain the target overlap integrals

$$\langle \mathbf{a} | \mathbf{b} + \mathbf{1}_i \rangle = \langle \mathbf{a} + \mathbf{1}_i | \mathbf{b} \rangle + (A_i - B_i) \langle \mathbf{a} | \mathbf{b} \rangle. \quad (3.8)$$

### 3.4 The Boys function

Whereas overlap integrals over GTOs have analytic solutions, the corresponding Coulomb interaction integrals must be built from a non-analytic function, named the *Boys function*. Defined by Boys in 1950 [78] it originates from the Laplace or Fourier transformation of the Coulomb interaction operator in these integrals. The Boys function is also referred to as an *incomplete gamma function* due to its relation to the Euler Gamma function. The Boys function of order  $n$  is defined by

$$F_n(x) = \int_0^1 t^{2n} e^{-xt^2} dt \quad \forall \quad x \geq 0 \quad (3.9)$$

For large values of  $x$  the Boys function can be asymptotically expanded as

$$F_n(x) = \int_0^\infty t^{2n} e^{-xt^2} dt - \int_1^\infty t^{2n} e^{-xt^2} dt \sim \int_0^\infty t^{2n} e^{-xt^2} dt, \quad (3.10)$$

where  $\sim$  means *asymptotically equals to*. The latter can be integrated to obtain

$$F_n(x) \sim \frac{(2n-1)!!}{2^{n+1}} \sqrt{\frac{\pi}{x^{2n+1}}}. \quad (3.11)$$

Eq. (3.11) is extremely important for the development of the present work. A comparison between the forms of the Boys function introduced here is shown in Figure 3.3. The conditions for the applicability of Eq. (3.11) will be explained in section 3.8.

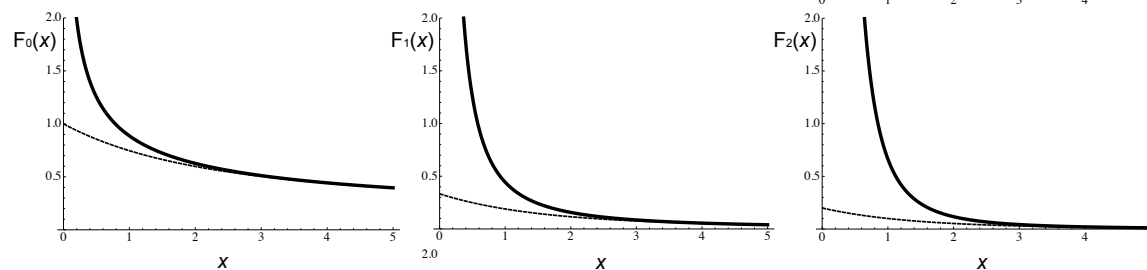


Figure 3.3: The Boys function of orders 0, 1 and 2 calculated with Eq. (3.9) (solid line) and the asymptotic expansion in Eq. (3.11) (dashed lined).

### 3.5 Nuclear attraction integrals

Nuclear attraction integrals refer to the interaction between electrons and nuclei with charge  $Z_C$

$$H_{ab}^{NAI} = \sum_C \left\langle \mathbf{ab} \left| \frac{Z_C}{|\vec{r} - \vec{C}|} \right. \right\rangle. \quad (3.12)$$

where  $NAI$  refers to the nuclear attraction integrals,  $C$  runs over all atoms and  $\vec{C}$  is the position vector of that atom. Efficient recurrence relations based on Hermite Gaussian type orbitals [101] for scaled nuclear attraction integrals were first given by McMurchie and Davidson (MD) [83]. To couple the MD scheme with Cartesian GTOs, the nuclear attraction integrals calculated in the HGTF basis must be transformed to their Cartesian counterparts. The pathway diagram for this algorithm is given in Figure 3.4 [99]. The diagram is read from lower left to upper right. The vertical arrow denotes the contraction step and horizontal arrows denote transformation steps. To

$$\begin{array}{ccccc}
 & & \langle \vec{r} | \sum \hat{\mathcal{A}}_C(\vec{0}) \rangle_{(u,v)} & \xrightarrow{\mathbf{T}} & \langle \mathbf{as} | \sum \hat{\mathcal{A}}_C(\vec{0}) \rangle & \xrightarrow{\mathbf{H}} & \langle \mathbf{ab} | \sum \hat{\mathcal{A}}_C(\vec{0}) \rangle \\
 & & \uparrow \mathbf{C} & & & & \\
 [\bar{s} | \hat{\mathcal{A}}_C(\vec{0})]^{(n)} & \xrightarrow{\mathbf{V}} & [\vec{r} | \hat{\mathcal{A}}_C(\vec{0})] & \xrightarrow{\mathbf{S}} & [\vec{r} | \sum \hat{\mathcal{A}}_C(\vec{0})] & & 
 \end{array}$$

Figure 3.4: Pathway diagram for the calculation of nuclear attraction integrals.

ease the notation, nuclear charges are omitted. The operator  $\hat{\mathcal{A}}_C(\bar{\mathbf{c}})$  is defined by:

$$\hat{\mathcal{A}}_C(\bar{\mathbf{c}}) = \left( \frac{\partial}{\partial C_x} \right)^{\bar{c}_x} \left( \frac{\partial}{\partial C_y} \right)^{\bar{c}_y} \left( \frac{\partial}{\partial C_z} \right)^{\bar{c}_z} \frac{1}{|\vec{r} - \vec{C}|}, \quad (3.13)$$

where the argument  $\bar{\mathbf{c}}$  represents the non-negative integers  $(\bar{c}_x, \bar{c}_y, \bar{c}_z)$ . Thus,  $\hat{\mathcal{A}}_C(\bar{\mathbf{0}})$  is identical with the Coulomb nuclear attraction operator  $1/|\vec{r} - \vec{C}|$ . The basic integrals in the lower-left corner of the pathway diagram are scaled primitive integrals, with  $\bar{\mathbf{s}}$  being located at the center of the orbital product  $\mathbf{ab}$

$$[\bar{\mathbf{s}}|\hat{\mathcal{A}}_C(\bar{\mathbf{0}})]^{(n)} = 2\pi \frac{(-2\zeta_p)^n}{\zeta_p} \kappa_{AB} F_n(T), \quad (3.14)$$

with

$$T = \zeta_p (\vec{P} - \vec{C})^2, \quad (3.15)$$

$(n)$  being a scaling index indicating the power of the pre-factor  $(-2\zeta_p)$  and the remaining quantities as given in Eq. (3.2) and (3.9). The Boys function is calculated with a combination [99] of the methods from MD [83] and Harris [102] in which the scaled integral allows the definition of efficient recurrence relations for the calculation of the nuclear attraction integrals. The next step, as implemented in deMon2k, is the vertical recurrence relation that increases the angular momentum index of the HGTF in the nuclear attraction integrals

$$[\bar{\mathbf{r}} + \bar{\mathbf{1}}_i|\hat{\mathcal{A}}_C(\bar{\mathbf{0}})]^{(n)} = (P_i - C_i)[\bar{\mathbf{r}}|\hat{\mathcal{A}}_C(\bar{\mathbf{0}})]^{(n+1)} + N_i(\bar{\mathbf{r}})[\bar{\mathbf{r}} - \bar{\mathbf{1}}_i|\hat{\mathcal{A}}_C(\bar{\mathbf{0}})]^{(n+1)}, \quad (3.16)$$

where  $i$  stands for  $x$ ,  $y$  or  $z$ ,  $P_i$  and  $C_i$  are the corresponding components of vectors  $\vec{P}$  and  $\vec{C}$  and  $N_i(\bar{\mathbf{r}})$  works as defined in Eq. (3.7). The results of this vertical recurrence relation are primitive HGTF nuclear attraction integrals of the type  $[\bar{\mathbf{r}}|\hat{\mathcal{A}}_C(\bar{\mathbf{0}})]$  in which the angular momentum index of both orbitals in the target integral is collected in  $\bar{\mathbf{r}}$ . The nuclear attraction integrals on different centers  $\vec{C}$  now can be summed, a

step denoted (S)

$$\sum_{\bar{C}} \left[ \bar{\mathbf{r}} \left| \hat{\mathcal{A}}_C(\bar{\mathbf{0}}) \right. \right] \equiv \left[ \bar{\mathbf{r}} \left| \sum \hat{\mathcal{A}}_C(\bar{\mathbf{0}}) \right. \right] \quad (3.17)$$

As a result, subsequent operations are performed with the integral sum rather than individual integrals. Therefore, these steps exhibit a formally quadratic scaling instead of the cubic scaling of the individual integrals. The first step in this formally quadratic scaling part of the pathway diagram (Figure 3.4) is the orbital contraction given by

$$\left\langle \bar{\mathbf{r}} \left| \sum \hat{\mathcal{A}}_C(\bar{\mathbf{0}}) \right. \right\rangle_{(u,v)} = \sum_k^{K_a} \sum_l^{K_b} \frac{\zeta_l^u}{(\zeta_k + \zeta_l)^v} d_k d_l \left[ \bar{\mathbf{r}}_{kl} \left| \sum \hat{\mathcal{A}}_C(\bar{\mathbf{0}}) \right. \right], \quad (3.18)$$

where the  $(u, v)$  scaling subscript is similar to the one in Eq. (3.6). The results of this step are the  $(u, v)$ -scaled contracted nuclear attraction integral sums over HGTF. In the transformation step (T) those Hermite GTOs are transformed to Cartesian GTO products

$$\begin{aligned} \left\langle \mathbf{a}\bar{\mathbf{b}} \left| \sum \hat{\mathcal{A}}_C(\bar{\mathbf{0}}) \right. \right\rangle_{(u,v)} &= (B_i - A_i) \left\langle (\mathbf{a} - \mathbf{1}_i) \bar{\mathbf{b}} \left| \sum \hat{\mathcal{A}}_C(\bar{\mathbf{0}}) \right. \right\rangle_{(u+1, v+1)} + \\ &\quad \frac{1}{2} \left\langle (\mathbf{a} - \mathbf{1}_i) (\bar{\mathbf{b}} + \bar{\mathbf{1}}_i) \left| \sum \hat{\mathcal{A}}_C(\bar{\mathbf{0}}) \right. \right\rangle_{(u, v+1)} + \\ &\quad N_i(\bar{\mathbf{b}}) \left\langle (\mathbf{a} - \mathbf{1}_i) (\bar{\mathbf{b}} - \bar{\mathbf{1}}_i) \left| \sum \hat{\mathcal{A}}_C(\bar{\mathbf{0}}) \right. \right\rangle_{(u, v)}. \end{aligned} \quad (3.19)$$

The recurrence ends with the integral  $\langle \mathbf{a}\bar{\mathbf{s}} \left| \sum \hat{\mathcal{A}}_C(\bar{\mathbf{0}}) \right. \rangle_{(u,v)} = \langle \mathbf{a}\mathbf{s} \left| \sum \hat{\mathcal{A}}_C(\bar{\mathbf{0}}) \right. \rangle_{(u,v)}$ , according to the definitions of Cartesian GTO and HGTF, Eq. (2.3) and (2.18). The results of this step are nuclear attraction integral sums with the entire angular momentum index located at orbital  $\mathbf{a}$ . With the horizontal recurrence relation (H)

$$\left\langle \mathbf{a}(\mathbf{b} + \mathbf{1}_i) \left| \sum \hat{\mathcal{A}}_C(\bar{\mathbf{0}}) \right. \right\rangle = \left\langle (\mathbf{a} + \mathbf{1}_i) \mathbf{b} \left| \sum \hat{\mathcal{A}}_C(\bar{\mathbf{0}}) \right. \right\rangle + (A_i - B_i) \left\langle \mathbf{a}\mathbf{b} \left| \sum \hat{\mathcal{A}}_C(\bar{\mathbf{0}}) \right. \right\rangle, \quad (3.20)$$

the final target integral sum  $\langle \mathbf{a}\mathbf{b} \left| \sum \hat{\mathcal{A}}_C(\bar{\mathbf{0}}) \right. \rangle$  can be obtained. Thus, only the calculation of the basic integrals, the vertical recurrence and the summation step are in the cubic loop whereas all other steps of this algorithm are in a quadratic loop. This illustrates the advantage of working with integral sums rather than individual integrals

in the recurrence relations.

## 3.6 Electron repulsion integrals

For the task discussed next the 1986 article from Obara and Saika (OS) [98] is an important reference point because it discusses ERI recurrence relations for Cartesian GTOs. Following that work, Pople and co-workers showed how the OS recurrence relations can be joined with the ones earlier developed by McMurchie and Davidson (MD) [83] for HGTF [84,100,103]. Over the last two decades several research groups developed and implemented efficient two-electron four-center ERI recurrence relations [104–109] on the basis of this work. On the other hand, Andzelm and coworkers initialized the use of OS-type recurrence relations for the calculation of two-electron three-center ERIs by zeroing out one exponent in the original four-center formulation [110–112]. The first explicit recurrence relations for the two-electron three-center ERIs based on the OS and MD algorithms were given in 1996 [84] and some years later formulated for HGTF [86]. The following sections review these recurrence relations and discuss their implementation in the direct SCF scheme [113] of deMon2k [86].

### 3.6.1 Calculation of the Kohn-Sham matrix elements

In the Kohn-Sham matrix definition, Eq. (2.23) and (2.36), two-electron three-center ERIs appear in a sum over auxiliary functions, multiplied either with the Coulomb (2.23) or with the Coulomb and exchange-correlation (2.36) fitting coefficients. For ease of notation, we use here only the Coulomb fitting coefficient,  $x_{\bar{c}}$ . Inclusion of the exchange-correlation fitting coefficients is straightforward. In Figure 3.5 the pathway diagram for the calculation of the Kohn-Sham matrix ERIs is depicted. The diagram again is read from the lower-left to the upper-right corner. The first step is the calculation of the one-center integral:

$$[\mathbf{s}]^{(n)} = \frac{2\pi^{5/2}}{\sqrt{\zeta_p + \zeta_{\bar{c}}}} \frac{(-2\alpha)^n}{\zeta_p \zeta_{\bar{c}}} \kappa_{AB} F_n(T) \quad (3.21)$$

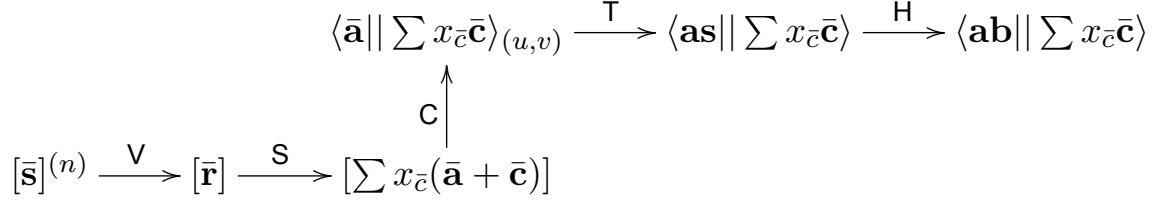


Figure 3.5: Pathway diagram for the calculation of the electron repulsion integrals for the Kohn-Sham matrix.

with

$$\alpha = \frac{\zeta_p \zeta_{\bar{\mathbf{c}}}}{\zeta_p + \zeta_{\bar{\mathbf{c}}}} \quad \text{and} \quad T = \alpha (\vec{P} - \vec{C})^2 \quad (3.22)$$

$(n)$  is a scaling index similar as the one in Eq. (3.14) and the rest of the definitions as given in Eq. (3.2) and (3.9). The center of this integral is the center of the Gaussian product of the orbitals and the auxiliary function. The next step is the vertical recurrence relation (V) for the one-center HGTF integrals

$$[\bar{\mathbf{r}} + \bar{\mathbf{1}}_i]^{(n)} = (P_i - C_i) [\bar{\mathbf{r}}]^{(n+1)} + N_i(\bar{\mathbf{r}}) [\bar{\mathbf{r}} - \bar{\mathbf{1}}_i]^{(n+1)}, \quad (3.23)$$

where  $i$  stands for  $x$ ,  $y$  or  $z$ ,  $P_i$  and  $C_i$  are the corresponding components of vectors  $\vec{P}$  and  $\vec{C}$  and  $N_i(\bar{\mathbf{r}})$  works as defined in Eq. (3.7). The results of the vertical recurrence relation are primitive HGTF integrals of the type  $[\bar{\mathbf{r}}]$  in which  $\bar{\mathbf{r}}$  collects the angular momentum index of the functions  $\mathbf{a}$ ,  $\mathbf{b}$  and  $\bar{\mathbf{c}}$ . Using the following relation given by McMurchie and Davidson [83]

$$[\bar{\mathbf{a}} || \bar{\mathbf{c}}] = (-1)^{\bar{c}} [\bar{\mathbf{r}}], \quad (3.24)$$

with  $\bar{\mathbf{r}} = \bar{\mathbf{a}} + \bar{\mathbf{c}}$  and  $(-1)^{\bar{c}} = (-1)^{\bar{c}_x + \bar{c}_y + \bar{c}_z}$ , we can directly expand the one-center integral into a two-center integral. The next step is the sum (S) over the auxiliary functions  $\bar{\mathbf{c}}$  along with the two-center expansion

$$\sum_{\bar{\mathbf{c}}} x_{\bar{\mathbf{c}}} [\bar{\mathbf{a}} || \bar{\mathbf{c}}] = \sum_{\bar{\mathbf{c}}} (-1)^{\bar{c}} x_{\bar{\mathbf{c}}} [\bar{\mathbf{r}}] \equiv \left[ \sum x_{\bar{\mathbf{c}}} (\bar{\mathbf{a}} + \bar{\mathbf{c}}) \right]. \quad (3.25)$$

Performing the sum step in this part of the algorithm keeps the auxiliary center loop out of all following loops. Thus, all following steps possess a formally quadratic instead of cubic scaling. The summation step produces primitive integral sums of the type  $\left[ \sum x_{\bar{c}}(\bar{\mathbf{a}} + \bar{\mathbf{c}}) \right]$ . The subsequent contraction (C) step is given by

$$\left\langle \bar{\mathbf{a}} \left\| \sum x_{\bar{c}} \bar{\mathbf{c}} \right\rangle_{(u,v)} = \sum_k^{K_a} \sum_l^{K_b} d_k d_l \frac{\zeta_l^u}{(\zeta_k + \zeta_l)^v} \left[ \sum x_{\bar{c}}(\bar{\mathbf{a}}_{kl} + \bar{\mathbf{c}}) \right], \quad (3.26)$$

where the  $(u, v)$  scaling subscript is similar to the one in Eq. (3.6). After the contraction step the Hermite Gaussian product function is transformed (T) into a Cartesian product by the following transformation recurrence relation

$$\begin{aligned} \left\langle (\mathbf{a} + \mathbf{1}_i) \bar{\mathbf{b}} \left\| \sum x_{\bar{c}} \bar{\mathbf{c}} \right\rangle_{(u,v)} &= (B_i - A_i) \left\langle \mathbf{a} \bar{\mathbf{b}} \left\| \sum x_{\bar{c}} \bar{\mathbf{c}} \right\rangle_{(u+1,v+1)} \right. \\ &\quad + \frac{1}{2} \left\langle \mathbf{a}(\bar{\mathbf{b}} + \bar{\mathbf{1}}_i) \left\| \sum x_{\bar{c}} \bar{\mathbf{c}} \right\rangle_{(u,v+1)} \right. \\ &\quad \left. + N_i(\bar{\mathbf{b}}) \left\langle \mathbf{a}(\bar{\mathbf{b}} - \bar{\mathbf{1}}_i) \left\| \sum x_{\bar{c}} \bar{\mathbf{c}} \right\rangle_{(u,v)} \right\rangle, \end{aligned} \quad (3.27)$$

where  $N_i(\bar{\mathbf{b}})$  works as defined in Eq. (3.7). This recurrence relation ends when the total angular momentum index of the orbitals in the target integral is collected in the Cartesian GTO. The result of the transformation are integrals of the type  $\langle \mathbf{a} \bar{\mathbf{s}} \left\| \sum x_{\bar{c}} \bar{\mathbf{c}} \right\rangle = \langle \mathbf{a} \mathbf{s} \left\| \sum x_{\bar{c}} \bar{\mathbf{c}} \right\rangle$ . Finally, the horizontal recurrence relation (H) is used to build the target integral

$$\left\langle \mathbf{a}(\mathbf{b} + \mathbf{1}_i) \left\| \sum x_{\bar{c}} \bar{\mathbf{c}} \right\rangle = \left\langle (\mathbf{a} + \mathbf{1}_i) \mathbf{b} \left\| \sum x_{\bar{c}} \bar{\mathbf{c}} \right\rangle + (A_i - B_i) \left\langle \mathbf{a} \mathbf{b} \left\| \sum x_{\bar{c}} \bar{\mathbf{c}} \right\rangle. \quad (3.28)$$

As this discussion shows, only the basic integral calculation, the integral summation and the vertical recurrence steps are in the auxiliary function loop, with a formal cubic scaling. The rest of the steps scale formally quadratic due to the early execution of the sum step. Moreover, the direct SCF ERI implementation in deMon2k works towards SCF convergence via incremental refinement of the Kohn-Sham matrix. This means that the Kohn-Sham matrix for the current SCF step,  $K_{ab}^{(I)}$ , is built from the addition of the Kohn-Sham matrix from the previous SCF step,  $K_{ab}^{(I-1)}$ , plus an increment  $\Delta K_{ab}$ , being this  $K_{ab}^{(I)} = K_{ab}^{(I-1)} + \Delta K_{ab}$ . Since  $\Delta K_{ab}$  depends on the values

of the difference  $\Delta x_{\bar{c}}$  between the current and previous SCF step fitting coefficients,  $\Delta x_{\bar{c}} = x_{\bar{c}}^{(I)} - x_{\bar{c}}^{(I-1)}$ , if  $\Delta x_{\bar{c}}$  is smaller than a given threshold the integrals related to it can be screened out, further reducing the computational effort in this procedure.

### 3.6.2 Calculation of the Coulomb vector elements

In Figure 3.6 the pathway diagram for the calculation of the Coulomb vector ERIs is depicted. The diagram is read from both ends toward the middle. The reason for this is that recurrence relations for two quantities are required: One for the integrals and one for the density matrix elements. In the lower-left corner the pathway diagram starts with the one-center integrals from Eq. (3.21), followed by the vertical recurrence given in Eq. (3.23) and a contraction step given by

$$\langle \bar{\mathbf{r}} \rangle_{(u,v)} = \sum_k^{K_a} \sum_l^{K_b} d_k d_l \frac{\zeta_l^u}{(\zeta_k + \zeta_l)^v} [\bar{\mathbf{r}}_{kl}], \quad (3.29)$$

where the  $(u, v)$  scaling subscript is similar to the one in Eq. (3.6). The expansion of the one-center integral into a two-center integral is given in Eq. (3.24) and is here used for the  $(u, v)$ -scaled contracted integrals. The results of the left-hand side part of Figure 3.6 are integrals of the type  $\langle \bar{\mathbf{r}} \rangle_{(u,v)}$  with  $\bar{\mathbf{r}} = \bar{\mathbf{a}} + \bar{\mathbf{c}}$ .

The recurrence relations for the density matrix elements are necessary to make their indexing consistent with the one of the  $(u, v)$ -scaled two-center HGTF ERIs. These recurrence relations are obtained from the horizontal and transformation integral recurrence relations by a mapping and filtering process [114]. They can be interpreted as a reverse horizontal recurrence relation ( $H^{-1}$ ) that concentrates the total angular

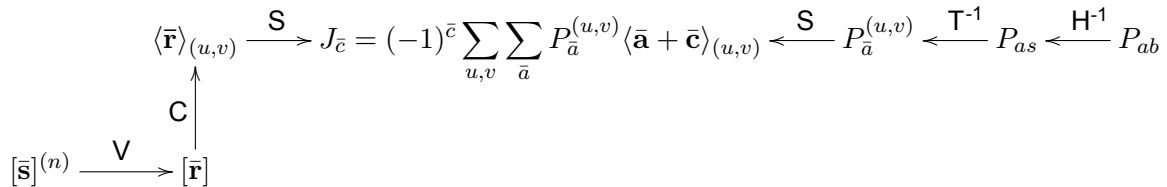


Figure 3.6: Pathway diagram for the calculation of the Coulomb vector. Unlike previous diagrams, this one is read from both ends toward the middle.

momentum on one index of the density matrix elements and a reverse transformation recurrence relation ( $T^{-1}$ ) that changes the Cartesian density matrix element into a Hermite one.

In the reversed horizontal recurrence relation, a density matrix element is involved in two steps: A shifting step that transfers angular momentum from one index to the other,

$$P_{(a+1_i)(b-1_i)} \leftarrow P_{ab}, \quad (3.30)$$

and a compaction step that reduces the total angular momentum of one index

$$P_{a(b-1_i)} \leftarrow (A_i - B_i)P_{ab}. \quad (3.31)$$

The goal of these steps is to transform a density matrix element from  $P_{ab}$  to  $P_{as} = P_{a\bar{s}}$ . Assignment diagrams for this procedure using  $P_{dd}$  and  $P_{ff}$  density matrix elements as examples are given in Figure 3.7. The algorithm starts from the top left and it depicts the results of shift steps (horizontal arrows) and compaction steps (vertical arrows). The horizontal recurrence procedure stops when all possible  $P_{as}$  quantities are formed.

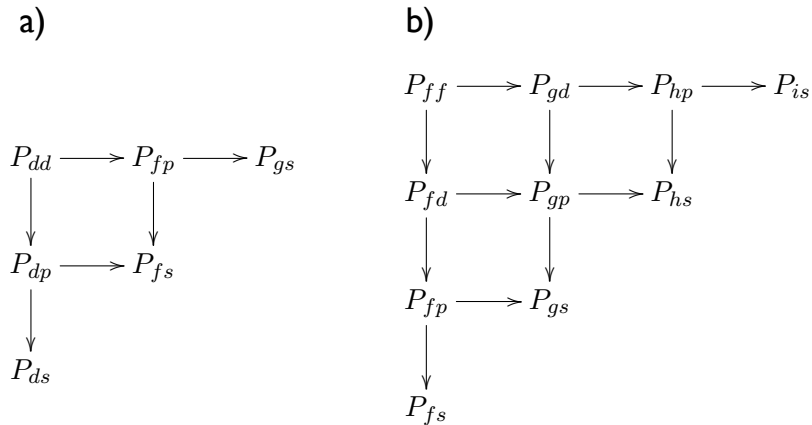


Figure 3.7: Assignment diagrams for the inverse horizontal recurrence relation of a)  $dd$  and b)  $ff$  density matrix elements. The shift steps are represented by horizontal arrows and the compaction steps by vertical arrows.

Once the total angular momentum of the density matrix element is shifted to one center, the transformation step can be started. This transformation involves three steps: A shifting that transfers angular momentum from the Cartesian to the Hermite index,

$$P_{(a-1_i)(\bar{b}+\bar{1}_i)}^{(u,v+1)} \leftarrow \frac{1}{2} P_{ab}^{(u,v)}, \quad (3.32)$$

a compaction step that reduces the Cartesian angular momentum index,

$$P_{(a-1_i)\bar{b}}^{(u+1,v+1)} \leftarrow (B_i - A_i) P_{ab}^{(u,v)}, \quad (3.33)$$

and a reduction that reduces, both Cartesian and Hermite, angular momentum indices,

$$P_{(a-1_i)(\bar{b}-\bar{1}_i)}^{(u,v)} \leftarrow N_i(\bar{b}) P_{ab}^{(u,v)}. \quad (3.34)$$

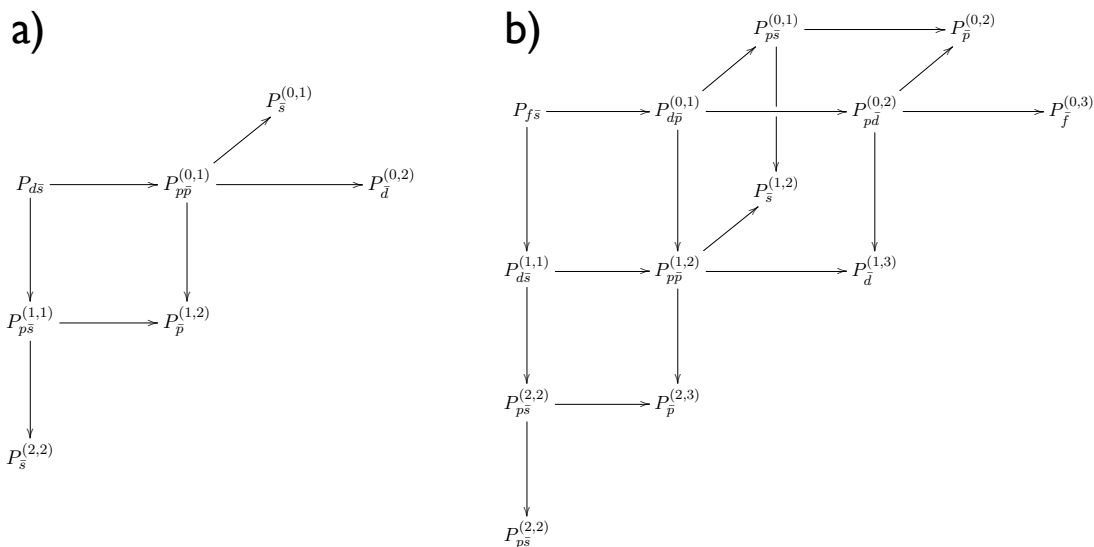


Figure 3.8: Assignment diagrams for the inverse orbital product transformation of a)  $ds$  and b)  $fs$  density matrix elements. Shift steps are represented by horizontal arrows, compaction steps by vertical arrows and reduction steps by out-of-plane arrows.

The goal of these procedures is to transform a density matrix element from  $P_{a\bar{s}}$  to  $P_{s\bar{a}}^{(u,v)} = P_{\bar{a}}^{(u,v)}$ . Assignment diagrams for the inverse orbital product transformation using  $P_{d\bar{s}}$  and  $P_{f\bar{s}}$  quantities as examples are given in Figure 3.8. The algorithm starts from the top left and it depicts the results of shift steps (horizontal arrows), compaction steps (vertical arrows) and reduction steps (out-of-plane arrows). The procedure ends when all possible  $P_{\bar{a}}^{(u,v)}$  quantities are formed. The  $(u,v)$ -scaling in the density matrix elements must not be mistaken with the one of the integrals that involves pre-factors with exponents. Here it is a *passive* scaling with the purpose to match with the corresponding scaled integrals in the summation step (S) of the pathway diagram in Figure 3.6. In the final summation step the Coulomb vector elements are calculated as

$$J_{\bar{c}} = (-1)^{\bar{c}} \sum_{u,v} \sum_{\bar{a}} P_{\bar{a}}^{(u,v)} \langle \bar{\mathbf{a}} || \bar{\mathbf{c}} \rangle_{(u,v)} \quad (3.35)$$

### 3.7 Analytic energy derivative

When a perturbation is applied to a system, the system energy change due to the perturbation is calculated by energy derivatives with respect to the perturbation parameters. In the framework of ADFT, assuming a closed-shell system, the derivative of the energy in Eq. (2.29) can be expressed as

$$\begin{aligned} E^{(\lambda)} &= \sum_{a,b} P_{ab}^{(\lambda)} \left( H_{ab} + \sum_{\bar{c}} \langle \mathbf{ab} || \bar{\mathbf{c}} \rangle x_{\bar{c}} \right) + E_{xc}^{(\lambda)}[\tilde{\rho}] + \\ &\sum_{a,b} P_{ab} \left( H_{ab}^{(\lambda)} + \sum_{\bar{c}} \langle \mathbf{ab} || \bar{\mathbf{c}} \rangle^{(\lambda)} x_{\bar{c}} \right) - \frac{1}{2} \sum_{\bar{c},\bar{d}} x_{\bar{c}} x_{\bar{d}} G_{\bar{c}\bar{d}}^{(\lambda)} + \\ &\sum_{\bar{c}} x_{\bar{c}}^{(\lambda)} \left( \sum_{a,b} P_{ab} \langle \mathbf{ab} || \bar{\mathbf{c}} \rangle - \sum_{\bar{d}} x_{\bar{d}} \langle \bar{\mathbf{c}} || \bar{\mathbf{d}} \rangle \right) \end{aligned} \quad (3.36)$$

Here, the superscript  $\lambda$  denotes the perturbation parameter (that is also the derivative variable) which in our case will be an atomic coordinate. Without going in further details, we note that the derivatives of the density matrix elements and fitting coefficients can be eliminated from Eq. (3.36) due to the  $(2n+1)$  rule for perturbation theory [55,115,116]. Thus, after further algebraic simplifications [51,117,118] we ob-

tain the following expression for the first-order energy derivatives

$$\begin{aligned}
 E^{(\lambda)} = & - \sum_{a,b} W_{ab} S_{ab}^{(\lambda)} + \sum_{a,b} P_{ab} \left( H_{ab}^{(\lambda)} + \sum_{\bar{c}} \langle \mathbf{ab} | | \bar{\mathbf{c}} \rangle^{(\lambda)} (x_{\bar{c}} + z_{\bar{c}}) \right) - \\
 & \sum_{\bar{c},\bar{d}} \left( \frac{1}{2} x_{\bar{c}} + z_{\bar{c}} \right) x_{\bar{d}} G_{\bar{c}\bar{d}}^{(\lambda)} + \sum_{\bar{c}} x_{\bar{c}} \langle v_{xc} | \bar{\mathbf{c}}^{(\lambda)} \rangle, \tag{3.37}
 \end{aligned}$$

where

$$W_{ab} = 2 \sum_i^{occ} \epsilon_i c_{ai} c_{bi} \tag{3.38}$$

is the energy-weighted density matrix and  $\epsilon_i$  is a Kohn-Sham orbital energy. The important conclusion from Eq. (3.37) is that only molecular integral derivatives are needed in order to calculate analytic first derivatives of the energy. This shows that the computational efficiency of the energy gradient calculation is directly proportional to the efficiency of the underlying integral algorithms.

As already noted, in the case of geometry optimizations the perturbation is the displacement of the nuclear coordinates. For a change in the  $x$ -component of the nucleus  $A$  center, the explicit form of Eq. (3.37) is given by

$$\begin{aligned}
 \frac{\partial E}{\partial A_x} = & - \sum_{a,b} W_{ab} \frac{\partial S_{ab}}{\partial A_x} + \sum_{a,b} P_{ab} \left( \frac{\partial H_{ab}}{\partial A_x} + \sum_{\bar{c}} \frac{\partial \langle \mathbf{ab} | | \bar{\mathbf{c}} \rangle}{\partial A_x} (x_{\bar{c}} + z_{\bar{c}}) \right) - \\
 & \sum_{\bar{c},\bar{d}} \left( \frac{1}{2} x_{\bar{c}} + z_{\bar{c}} \right) x_{\bar{d}} \frac{\partial G_{\bar{c}\bar{d}}}{\partial A_x} + \sum_{\bar{c}} x_{\bar{c}} \left\langle v_{xc} \left| \frac{\partial \bar{\mathbf{c}}}{\partial A_x} \right. \right\rangle. \tag{3.39}
 \end{aligned}$$

Equivalent equations for any other Cartesian coordinate in a molecular system can be obtained straightforwardly. The evaluation of Eq. (3.39) requires the knowledge of both basis set and approximate densities. Thus, the density matrix and fitting coefficients must be taken from a converged SCF in order to apply this equation correctly. We must discuss in more detail the molecular integral derivatives in Eq. (3.39) that will be relevant for the gradient contributions obtained with the newly developed double asymptotic expansion. Before we discuss individual integral derivatives we first review relevant properties of GTO derivatives in general.

### 3.7.1 GTO derivatives

When a Cartesian GTO, like the one in Eq. (2.3), is differentiated with respect to one of the components of its center vector, in general the result is a combination of two Cartesian GTOs, one with an increased angular momentum index and another one with a decreased angular momentum index

$$\frac{\partial \mathbf{a}(\vec{r})}{\partial A_x} = 2\zeta_a[\mathbf{a} + \mathbf{1}_x |(\vec{r}) - N_x(\mathbf{a})[\mathbf{a} - \mathbf{1}_x |(\vec{r})], \quad (3.40)$$

where the bras  $[\mathbf{a} + \mathbf{1}_x |$  and  $[\mathbf{a} - \mathbf{1}_x |$  indicate the increase and decrease, respectively, of the angular momentum index of the Cartesian GTO (see section 3.1) and  $N_x(\mathbf{a})$  works as defined in Eq. (3.7). When the angular momentum index of the differentiated function is zero the second term in Eq. (3.40) is to be omitted. The terms involving functions  $[\mathbf{a} + \mathbf{1}_x |$  and  $[\mathbf{a} - \mathbf{1}_x |$  will be referred as *up-shift term* and *down-shift term*, respectively. This equation is the origin of the OS recurrence relations [98] for Cartesian GTOs because it connects GTOs of higher angular momentum index with the ones of lower angular momentum index. Such a connection is obviously advantageous for the calculation of integral derivatives over Cartesian GTOs since it reduces these derivatives to modified standard integrals that have been already discussed.

In the case of a HGTF, as defined in Eq. (2.18), the derivative with respect to the  $x$ -component of its center yields

$$\frac{\partial \bar{\mathbf{c}}(\vec{r})}{\partial C_x} = [\bar{\mathbf{c}} + \bar{\mathbf{1}}_x |(\vec{r}), \quad (3.41)$$

where the bra  $[\bar{\mathbf{c}} + \bar{\mathbf{1}}_x |$  indicates the increase of  $x$ -component of the angular momentum index of the HGTF (see section 3.1). Thus, the differentiation with respect to a center coordinate yields only one HGTF with an increased angular momentum index. This feature will be important for the algorithms used for the calculation of electrostatic interaction integral derivatives in the next sections.

### 3.7.2 Overlap integral derivatives

The primitive overlap integral derivative can be obtained straightforwardly from Eq. (3.40) and is given by

$$\frac{\partial[\mathbf{a}|\mathbf{b}]}{\partial A_x} = 2\zeta_a[\mathbf{a} + \mathbf{1}_x|\mathbf{b}] - N_x(\mathbf{a})[\mathbf{a} - \mathbf{1}_x|\mathbf{b}]. \quad (3.42)$$

Since the exponent  $\zeta_a$  is characteristic for each primitive function, as seen in Eq. (2.3), the contracted integral derivative must be built with a scaling at the primitive level. We therefore introduce for the contracted overlap integral derivative the notation

$$\frac{\partial\langle\mathbf{a}|\mathbf{b}\rangle}{\partial A_x} = 2\langle\mathbf{a} + \mathbf{1}_x|\mathbf{b}\rangle_{(1)} - N_x(\mathbf{a})\langle\mathbf{a} - \mathbf{1}_x|\mathbf{b}\rangle, \quad (3.43)$$

with

$$\langle\mathbf{a}|\mathbf{b}\rangle_{(1)} = \sum_k^{K_a} \sum_l^{K_b} d_k d_l \zeta_k[\mathbf{a}_k|\mathbf{b}_l], \quad (3.44)$$

where  $\zeta_k$  is the exponent of the primitive function  $\mathbf{a}_k$  and the subscript (1) is related to the power of such exponent. We will use this notation for all contracted integral derivatives in the following sections. Since the overlap integral of  $\mathbf{a}$  and  $\mathbf{b}$  does not change under translation of the system as a whole (since the quantity  $(\vec{A} - \vec{B})^2$  does not change with the translation) [119], we have

$$\frac{\partial\langle\mathbf{a}|\mathbf{b}\rangle}{\partial A_x} + \frac{\partial\langle\mathbf{a}|\mathbf{b}\rangle}{\partial B_x} = 0, \quad (3.45)$$

the corresponding derivative with respect to the  $B$  center can be calculated as

$$\frac{\partial\langle\mathbf{a}|\mathbf{b}\rangle}{\partial B_x} = -\frac{\partial\langle\mathbf{a}|\mathbf{b}\rangle}{\partial A_x} = -2\langle\mathbf{a} + \mathbf{1}_x|\mathbf{b}\rangle_{(1)} + N_x(\mathbf{a})\langle\mathbf{a} - \mathbf{1}_x|\mathbf{b}\rangle. \quad (3.46)$$

Thus, only the overlap integral derivatives with respect to the components of  $\vec{A}$  are explicitly calculated. The other derivatives can be obtained from the translational invariance relation, Eq. (3.45).

$$\begin{array}{c}
 \langle \mathbf{s} | \mathbf{s} \rangle_{(u,v,1)} \xrightarrow{\text{V}} \langle \mathbf{a} + \mathbf{1}_i | \mathbf{s} \rangle_{(1)} \xrightarrow{\text{H}} \langle \mathbf{a} + \mathbf{1}_i | \mathbf{b} \rangle_{(1)} \\
 \uparrow \text{C} \\
 [\mathbf{s} | \mathbf{s}]
 \end{array}$$

Figure 3.9: Pathway diagram for the calculation of the overlap integral derivative up-shift term.

The pathway diagram for the calculation of the overlap integral derivative up-shift term is given in Figure 3.9. The diagram starts in the lower-left corner and ends in the upper-right corner. The first step is the calculation of the basic integral given in Eq. (3.5). This is followed by the contraction step (C). In order to take advantage of the  $(u, v)$ -scaling procedure, the scaling given by the integral derivative can be applied in this step as follows:

$$\langle \mathbf{s} | \mathbf{s} \rangle_{(u,v,1)} = \sum_k^{K_a} \sum_l^{K_b} d_k d_l \frac{\zeta_k \zeta_l^u}{(\zeta_k + \zeta_l)^v} [\mathbf{s}_k | \mathbf{s}_l], \quad (3.47)$$

where the scaling indices  $(u, v)$  are the same from Eq. (3.6) and the scaling index (1) comes from Eq. (3.44). Thus, the full scaling for the integral derivative is done in the contraction step. The vertical recurrence (V) from Eq. (3.7) builds angular momentum index on the orbital at center  $\vec{A}$ . Finally, the horizontal recurrence (H) from Eq. (3.8) shifts the angular momentum index from orbital  $\mathbf{a}$  to orbital  $\mathbf{b}$ . The pathway diagram for the calculation of the overlap integral derivative down-shift term is given in Figure 3.10. The diagram starts in the lower-left corner and ends in the upper-right corner. Again the same integral recurrence relations as for the calculation of the overlap integrals (see section 3.3) are used. The difference is that the angular

$$\begin{array}{c}
 \langle \mathbf{s} | \mathbf{s} \rangle_{(u,v)} \xrightarrow{\text{V}} \langle \mathbf{a} - \mathbf{1}_i | \mathbf{s} \rangle \xrightarrow{\text{H}} \langle \mathbf{a} - \mathbf{1}_i | \mathbf{b} \rangle \\
 \uparrow \text{C} \\
 [\mathbf{s} | \mathbf{s}]
 \end{array}$$

Figure 3.10: Pathway diagram for the calculation of the overlap integral derivative down-shift term.

momentum is reduced in the target overlap integral according to Eq. (3.43). Thus, the calculation of the overlap integral derivatives rely on the same integral recurrence relations that are used for the overlap integrals.

### 3.7.3 Nuclear attraction integral derivatives

The relevant terms for the asymptotic expansion of the core Hamiltonian derivative  $\partial H_{ab}/\partial A_x$  in Eq. (3.39) are the nuclear attraction integral (NAI) derivatives. The NAIs are differentiated with respect to three atomic centers, two at which the orbitals are located and one at which the operator is located. These three derivatives are again connected by translational invariance [119]

$$\frac{\partial}{\partial A_x} \langle \mathbf{ab} | \sum \hat{\mathcal{A}}_C(\bar{\mathbf{0}}) \rangle + \frac{\partial}{\partial B_x} \langle \mathbf{ab} | \sum \hat{\mathcal{A}}_C(\bar{\mathbf{0}}) \rangle + \frac{\partial}{\partial C_x} \langle \mathbf{ab} | \sum \hat{\mathcal{A}}_C(\bar{\mathbf{0}}) \rangle = 0. \quad (3.48)$$

Therefore, only two of them must be explicitly calculated. For a derivative with respect to a component of center coordinate  $\vec{A}$ , one has

$$\begin{aligned} \frac{\partial}{\partial A_x} \langle \mathbf{ab} | \sum \hat{\mathcal{A}}_C(\bar{\mathbf{0}}) \rangle &= 2 \langle (\mathbf{a} + \mathbf{1}_x) \mathbf{b} | \sum \hat{\mathcal{A}}_C(\bar{\mathbf{0}}) \rangle_{(1)} - \\ &N_x(\mathbf{a}) \langle (\mathbf{a} - \mathbf{1}_x) \mathbf{b} | \sum \hat{\mathcal{A}}_C(\bar{\mathbf{0}}) \rangle, \end{aligned} \quad (3.49)$$

where

$$\langle \mathbf{ab} | \sum \hat{\mathcal{A}}_C(\bar{\mathbf{0}}) \rangle_{(1)} = \sum_k^{K_a} \sum_l^{K_b} d_k d_l \zeta_k \left[ \mathbf{ab} | \sum \hat{\mathcal{A}}_C(\bar{\mathbf{0}}) \right], \quad (3.50)$$

where the sums run over the number of nuclei as given in Eq. (3.17), the subscript (1) is the scaling explained for Eq. (3.44) and  $N_x(\mathbf{a})$  works as defined in Eq. (3.7). The corresponding derivatives with respect to the other components of  $\vec{A}$  and for center  $\vec{B}$  can be obtained in the same form. The derivative with respect to the  $x$ -component of the operator center yields

$$\frac{\partial}{\partial C_x} \langle \mathbf{ab} | \sum \hat{\mathcal{A}}_C(\bar{\mathbf{0}}) \rangle = \langle \mathbf{ab} | \sum \hat{\mathcal{A}}_C(\bar{\mathbf{1}}_x) \rangle, \quad (3.51)$$

where  $\hat{\mathcal{A}}_C(\bar{\mathbf{c}})$  has the form given in Eq. (3.13). The operator derivative can be easily included at the level of HGTF integrals due to the relation,

$$\left[\bar{\mathbf{r}}\left|\hat{\mathcal{A}}_C(\bar{\mathbf{1}}_i)\right.\right]^{(n)} = -\left[\bar{\mathbf{r}} + \bar{\mathbf{1}}_i\left|\hat{\mathcal{A}}_C(\bar{\mathbf{0}})\right.\right]^{(n)}, \quad (3.52)$$

where  $i$  stands for  $x$ ,  $y$  and  $z$  and the scaling index  $(n)$  is the same as given in Eq. (3.14). Thus, the nuclear attraction gradient component is formed in deMon2k by an orbital and an operator center derivative. The other orbital derivative is calculated from these two quantities by the translational invariance condition, Eq (3.48), yielding the following relation for the gradient contributions

$$g_{B_x}^{NAI} = -g_{A_x}^{NAI} - g_{C_x}^{NAI}, \quad (3.53)$$

with

$$g_{A_x}^{NAI} = 2 \sum_{a,b} P_{ab} \left\langle (\mathbf{a} + \mathbf{1}_x)\mathbf{b} \left| \sum \hat{\mathcal{A}}_C(\bar{\mathbf{0}}) \right. \right\rangle_{(1)} - \sum_{a,b} P_{ab} N_x(\mathbf{a}) \left\langle (\mathbf{a} - \mathbf{1}_x)\mathbf{b} \left| \sum \hat{\mathcal{A}}_C(\bar{\mathbf{0}}) \right. \right\rangle, \quad (3.54)$$

and

$$g_{C_x}^{NAI} = \sum_{a,b} P_{ab} \left\langle \mathbf{ab} \left| \sum \hat{\mathcal{A}}_C(\bar{\mathbf{1}}) \right. \right\rangle, \quad (3.55)$$

where the superscript *NAI* refers to the nuclear attraction contribution. Equivalent equations can be defined straightforwardly for the other components of  $\vec{A}$ ,  $\vec{B}$  and  $\vec{C}$ . The pathway diagram for the calculation of the up-shift term in the nuclear attraction integral derivative, Eq. (3.49), is depicted in Figure 3.11. The diagram starts in the lower-left corner and ends in the upper-right corner. The first step is the calculation of the basic integral as given in Eq. (3.14). The vertical recurrence relation (V) from Eq. (3.16) builds angular momentum at the one-center function  $\bar{\mathbf{r}}$ . Next, the summation step (S) collects the contributions from all the nuclear centers as shown in Eq. (3.17). The contraction step (C) now includes an additional scaling value as follows:

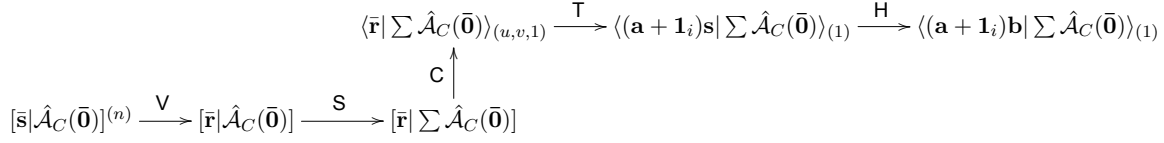


Figure 3.11: Pathway diagram for the calculation of the nuclear attraction integral derivative up-shift term.

$$\left\langle \bar{\mathbf{r}} \left| \sum \hat{\mathcal{A}}_C(\bar{\mathbf{0}}) \right. \right\rangle_{(u,v,1)} = \sum_k^{K_a} \sum_l^{K_b} d_k d_l \frac{\zeta_k \zeta_l^u}{(\zeta_k + \zeta_l)^v} \left[ \bar{\mathbf{r}}_{kl} \left| \sum \hat{\mathcal{A}}_C(\bar{\mathbf{0}}) \right. \right]. \quad (3.56)$$

The scaling indicated by the subscript  $(u, v, 1)$  is similar as the one in Eq. (3.47). Once the contracted integral has been correctly scaled, the transformation step (T) from Eq. (3.19) is used to change the HGTFs in the bra to Cartesian GTO products. Finally, the horizontal recurrence step (H) shifts the angular momentum index from orbital  $\mathbf{a}$  to orbital  $\mathbf{b}$  using Eq. (3.20).

The pathway diagram for the calculation of the down-shift term in the nuclear attraction integral derivative, Eq. (3.49), is depicted in Figure 3.12. The diagram starts in the lower-left corner and ends in the upper-right corner. This diagram relies on the same integral recurrence relations that are used for the calculation of the core nuclear attraction integrals in section 3.5 (see also Figure 3.4 for the corresponding diagram). The only difference is that the angular momentum index for orbital  $\mathbf{a}$  is reduced according to Eq. (3.49).

The pathway diagram for the calculation of the nuclear attraction integral derivative with respect to the operator center, Eq. (3.51), is depicted in Figure 3.13. The diagram is read from both ends toward the middle. The integral calculation starts in

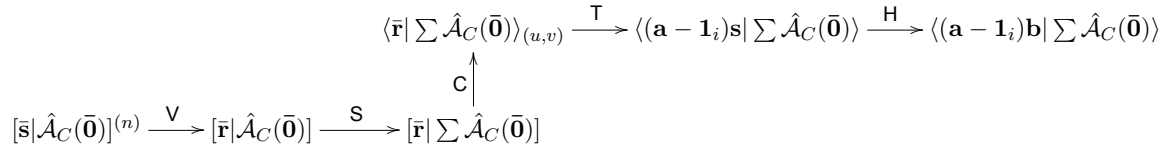


Figure 3.12: Pathway diagram for the calculation of the nuclear attraction integral derivative down-shift term.

$$\begin{array}{c}
\langle \bar{\mathbf{r}} | \hat{A}_C(\bar{\mathbf{0}}) \rangle_{(u,v)} \xrightarrow{\text{S}} g_{C_x}^{NAI} = - \sum_{u,v} \sum_{\bar{a}} P_{\bar{a}}^{(u,v)} \langle \bar{\mathbf{a}} + \bar{\mathbf{1}}_x | \hat{A}_C(\bar{\mathbf{0}}) \rangle_{(u,v)} \xleftarrow{\text{S}} P_{\bar{a}}^{(u,v)} \xleftarrow{\text{T}^{-1}} P_{as} \xleftarrow{\text{H}^{-1}} P_{ab} \\
\uparrow \text{C} \\
[\bar{\mathbf{s}} | \hat{A}_C(\bar{\mathbf{0}})]^{(n)} \xrightarrow{\text{V}} [\bar{\mathbf{r}} | \hat{A}_C(\bar{\mathbf{0}})]
\end{array}$$

Figure 3.13: Pathway diagram for the calculation of the nuclear attraction integral derivative with respect to the operator center.

the lower-left corner with the calculation of the basic integral from Eq. (3.14). Next, the vertical recurrence (V) relation, Eq. (3.16), is used to build up the angular momentum index at the one-center function  $\bar{\mathbf{r}}$ . The contraction (C) of the primitive integrals is given by Eq. (3.29). The density matrix recurrence relations start in the upper-right corner and are identical to the ones used for the calculation of the Coulomb vector elements (see section 3.6.2). Thus, the reverse horizontal ( $\text{H}^{-1}$ ) and reverse transformation ( $\text{T}^{-1}$ ) recurrence relations are used to transform the density matrix elements  $P_{ab}$  into  $P_{\bar{a}}^{(u,v)}$ . In the final summation (S) step the transformed density matrix elements and integrals are joined together to form a gradient component.

### 3.7.4 Electron repulsion integral derivatives

Just as with the nuclear attraction integrals, the three-center electron repulsion integrals (ERI) are also differentiated with respect to three atomic centers, two on which the orbitals are located and one on which the auxiliary function is located. Again, these derivatives are connected by translational invariance. For example, differentiation with respect to the  $x$ -component of the function centers

$$\frac{\partial}{\partial A_x} \langle \mathbf{ab} \parallel \sum x_{\bar{c}} \bar{\mathbf{c}} \rangle + \frac{\partial}{\partial B_x} \langle \mathbf{ab} \parallel \sum x_{\bar{c}} \bar{\mathbf{c}} \rangle + \frac{\partial}{\partial C_x} \langle \mathbf{ab} \parallel \sum x_{\bar{c}} \bar{\mathbf{c}} \rangle = 0. \quad (3.57)$$

Thus, the explicit calculation of two of these derivatives is sufficient, with the third obtained by the translational invariance condition. For the differentiation with respect to the  $x$ -component of center  $\vec{A}$  we find

$$\frac{\partial}{\partial A_x} \langle \mathbf{ab} \parallel \sum x_{\bar{c}} \bar{\mathbf{c}} \rangle = 2 \langle (\mathbf{a} + \mathbf{1}_x) \mathbf{b} \parallel \sum x_{\bar{c}} \bar{\mathbf{c}} \rangle_{(1)} - N_x(\mathbf{a}) \langle (\mathbf{a} - \mathbf{1}_x) \mathbf{b} \parallel \sum x_{\bar{c}} \bar{\mathbf{c}} \rangle. \quad (3.58)$$

The up-shift scaled integral is given by

$$\left\langle \mathbf{ab} \left\| \sum x_{\bar{c}} \bar{\mathbf{c}} \right\rangle_{(1)} = \sum_k^{K_a} \sum_l^{K_b} d_k d_l \zeta_k \left[ \mathbf{ab} \left\| \sum x_{\bar{c}} \bar{\mathbf{c}} \right\rangle \right]. \quad (3.59)$$

where the subscript (1) is explained in Eq. (3.44). The derivative with respect to  $B_x$  is obtained in the same form. On the other hand, the differentiation with respect to the  $x$ -component of the auxiliary function center  $\vec{C}$  yields

$$\frac{\partial}{\partial C_x} \left\langle \mathbf{ab} \left\| \sum x_{\bar{c}} \bar{\mathbf{c}} \right\rangle = \left\langle \mathbf{ab} \left\| \sum x_{\bar{c}} (\bar{\mathbf{c}} + \bar{\mathbf{1}}_x) \right\rangle \right\rangle. \quad (3.60)$$

Since the differentiation with respect to the auxiliary function center yields only one term, it is preferred to calculate the derivatives with respect to the components of  $\vec{A}$  and  $\vec{C}$  and obtain the derivatives with respect to the components of  $\vec{B}$  using the translational invariance condition, Eq. (3.57). Thus, the gradient contributions from the ERI derivatives are given by

$$g_{B_x}^{ERI} = -g_{A_x}^{ERI} - g_{C_x}^{ERI}, \quad (3.61)$$

where

$$g_{A_x}^{ERI} = 2 \sum_{a,b} P_{ab} \left\langle (\mathbf{a} + \mathbf{1}_x) \mathbf{b} \left\| \sum x_{\bar{c}} \bar{\mathbf{c}} \right\rangle_{(1)} - \sum_{a,b} P_{ab} N_x(\mathbf{a}) \left\langle (\mathbf{a} - \mathbf{1}_x) \mathbf{b} \left\| \sum x_{\bar{c}} \bar{\mathbf{c}} \right\rangle \right\rangle. \quad (3.62)$$

and

$$g_{C_x}^{ERI} = \sum_{a,b} P_{ab} \left\langle \mathbf{ab} \left\| \sum x_{\bar{c}} (\bar{\mathbf{c}} + \bar{\mathbf{1}}_x) \right\rangle \right\rangle. \quad (3.63)$$

Equivalent equations can be obtained for the  $y$ - and  $z$ -component of the atomic centers. The pathway diagram for the calculation of the up-shift term in the ERI derivative, Eq. (3.58), is depicted in Figure 3.14. The diagram starts in the lower-left corner and finishes in the upper-right corner. The first step is the calculation of the basic integral given in Eq. (3.21). The angular momentum index of the one-center function is built by vertical recurrence steps (V) using Eq. (3.23). Using the relation from Eq. (3.24) the summation step (S) is performed as described in Eq. (3.25). The contraction step

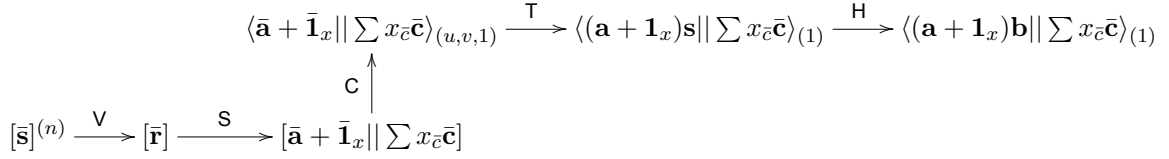


Figure 3.14: Pathway diagram for the calculation of the electron repulsion integral derivative up-shift term.

(C) for the scaled ERI derivative is given by

$$\left\langle \bar{\mathbf{a}} \left\| \sum x_{\bar{\mathbf{c}}} \bar{\mathbf{c}} \right\rangle_{(u,v,1)} = \sum_k^{K_a} \sum_l^{K_b} d_k d_l \frac{\zeta_k \zeta_l^u}{(\zeta_k + \zeta_l)^v} \left[ \sum x_{\bar{\mathbf{c}}} (\bar{\mathbf{a}} + \bar{\mathbf{c}}) \right], \quad (3.64)$$

where the  $(u, v, 1)$  subscript is the one explained in Eq. (3.47). The transformation step from Eq. (3.27) is applied to transform the HGTFs to Cartesian GTO products. Finally, the horizontal recurrence step (H) from Eq. (3.28) yields the target integral. The pathway diagram for the calculation of the down-shift term in the ERI derivative, Eq. (3.58), is depicted in Figure 3.15. The diagram starts in the lower-left corner and finishes in the upper-right corner. This diagram employs the same integral recurrence relations as given in section 3.6.1 (see also Figure 3.5 for the corresponding pathway diagram). The only difference is the reduced angular momentum index on orbital  $\mathbf{a}$ .

The pathway diagram for the calculation of the ERI derivative with respect to the auxiliary function center, Eq. (3.60), is depicted in Figure 3.16. The diagram is read from both ends toward the middle. The integral calculation starts in the lower-left corner with the calculation of the basic integral, Eq. (3.21). Next, the vertical recurrence relation (V), Eq. (3.23), builds up angular momentum index at the one-center

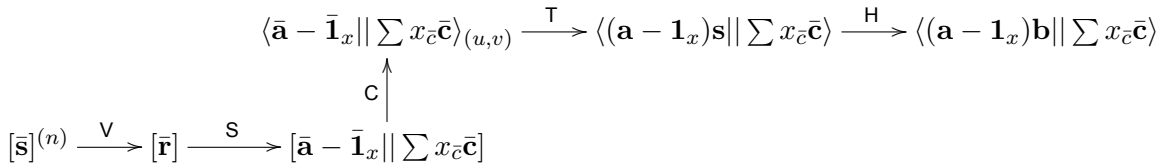


Figure 3.15: Pathway diagram for the calculation of the electron repulsion integral derivative down-shift term.

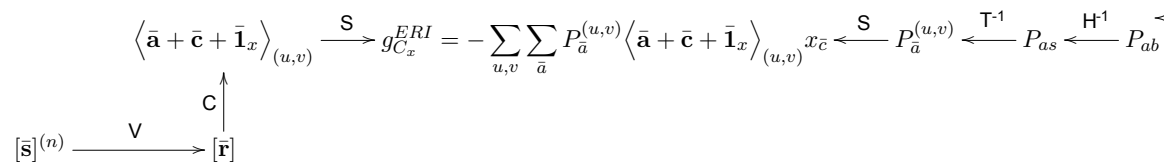


Figure 3.16: Pathway diagram for the calculation of the electron repulsion integral derivative with respect to the auxiliary function center.

function. The contraction of the primitive integrals is given by Eq. (3.29). The density matrix recurrence relations are identical to the ones for the corresponding nuclear attraction integral derivatives, Fig. 3.13. In the summation step (S) the transformed density matrix elements and integrals are joined to form the gradient component. This discussion underscores the similarities in the calculation of nuclear attraction integral derivatives and three-center ERI derivatives.

## 3.8 Asymptotic expansion of electron repulsion integrals

Within the ADFT implementation, the three-center ERIs become a bottleneck in the calculations of large molecular systems. However, when the overlap between two electron densities  $\rho_A$  and  $\rho_B$  is negligible, the electrostatic Coulomb energy of their interaction,

$$E_{el-el} = \iint \frac{\rho_A(\vec{r}_1)\rho_B(\vec{r}_2)}{|\vec{r}_1 - \vec{r}_2|} d\vec{r}_1 d\vec{r}_2, \quad (3.65)$$

may be approximated accurately by expanding  $1/|\vec{r}_1 - \vec{r}_2|$  in a multipole series [120]. A breakthrough algorithm for the handling of long-range interactions came with the introduction and development of the Fast Multipole Method (FMM) by Greengard and Rokhlin [121–124]. Several methods have been created in order to adapt the FMM for electronic structure calculations [125–127]. One of the main features of the method is the division of the system in boxes to a certain level to define regions of nearest neighbors. In such regions, interactions between the particles of the central box and the nearest neighbors are handled directly. For the boxes outside such re-

gions, interactions between particles of the central box and the further neighbors are calculated using multipole expansions. In deMon2k, this fact is used in another way [86]. The three-center ERIs are written as one-electron integrals. Then, near- and far-field regions are defined. Integrals in the near-field are calculated using the methods in sections 3.5 and 3.6 and integrals in the far-field are calculated using the asymptotic expansion of the Boys function, Eq. (3.10). Details of the far-field calculation are given below.

The three-center ERI can be written as a one-electron integral with the following definition

$$\langle \mathbf{a}\mathbf{b} || \bar{\mathbf{c}} \rangle = \int \mathbf{a}(\vec{r})\mathbf{b}(\vec{r})\phi_{\bar{\mathbf{c}}}(\vec{r})d\vec{r}, \quad (3.66)$$

where

$$\phi_{\bar{\mathbf{c}}}(\vec{r}) = \int \frac{\bar{\mathbf{c}}(\vec{r}')}{|\vec{r} - \vec{r}'|} d\vec{r}' \equiv ||\bar{\mathbf{c}}], \quad (3.67)$$

is the electrostatic potential generated by  $\bar{\mathbf{c}}(\vec{r}')$  at position  $\vec{r}$ . The last equation resembles a nuclear attraction integral, Eq. (3.12), where the "center" of the operator defined in Eq (3.13) is at  $\vec{r}$ . Thus, an equivalent of the recurrence relation in Eq. (3.16) is valid for the electrostatic potential

$$||\bar{\mathbf{c}} + \bar{\mathbf{1}}_i]^{(n)} = (C_i - r_i) ||\bar{\mathbf{c}}]^{(n+1)} + N_i(\bar{\mathbf{c}}) ||\bar{\mathbf{c}} - \bar{\mathbf{1}}_i]^{(n+1)}, \quad (3.68)$$

where  $i = x, y, z$  and  $N_i(\bar{\mathbf{c}})$  is the same function given in Eq. (3.7) acting on the angular momentum index triad of function  $\bar{\mathbf{c}}$ . The basic integral is

$$||\bar{\mathbf{s}}]^{(n)} = \frac{2\pi}{\zeta_{\bar{\mathbf{c}}}} (-2\zeta_{\bar{\mathbf{c}}})^n F_n(T), \quad (3.69)$$

with  $F_n(T)$  defined in Eq. (3.9) and

$$T = \zeta_{\bar{\mathbf{c}}}(\vec{r} - \vec{C})^2. \quad (3.70)$$

From Eq. (3.11) we find the asymptotic expansion for the basic electrostatic potential integral

$$||\bar{\mathbf{s}}] \sim \left(\frac{\pi}{\zeta_{\bar{c}}}\right)^{\frac{3}{2}} \frac{1}{|\vec{r} - \vec{C}|}. \quad (3.71)$$

From the definition of the auxiliary functions, Eq. (2.18), higher angular momentum index integrals for the electrostatic potential and its asymptotic expansion can be found straightforwardly

$$\begin{aligned} ||\bar{\mathbf{c}}] &= \left(\frac{\partial}{\partial C_x}\right)^{\bar{c}_x} \left(\frac{\partial}{\partial C_y}\right)^{\bar{c}_y} \left(\frac{\partial}{\partial C_z}\right)^{\bar{c}_z} ||\bar{\mathbf{s}}] \\ &\sim \left(\frac{\pi}{\zeta_{\bar{c}}}\right)^{\frac{3}{2}} \left(\frac{\partial}{\partial C_x}\right)^{\bar{c}_x} \left(\frac{\partial}{\partial C_y}\right)^{\bar{c}_y} \left(\frac{\partial}{\partial C_z}\right)^{\bar{c}_z} \frac{1}{|\vec{r} - \vec{C}|}. \end{aligned} \quad (3.72)$$

In general, the asymptotic expansion of the three-center ERI can be written as [86]:

$$\langle \mathbf{ab} || \bar{\mathbf{c}} \rangle \sim \left(\frac{\pi}{\zeta_{\bar{c}}}\right)^{\frac{3}{2}} \langle \mathbf{ab} | \hat{\mathcal{A}}_C(\bar{\mathbf{c}}) \rangle. \quad (3.73)$$

where  $\hat{\mathcal{A}}_C(\bar{\mathbf{c}})$  is defined in Eq. (3.13).

Now it is appropriate to define the conditions under which the asymptotic expansion for the ERIs can be applied. This is accomplished by defining extents for the potential and orbitals in Eq. (3.66). Strictly, orbitals and potential have infinite extent but the following definitions are based on tolerances to maintain the accuracy of the ERI calculation. According to Eq. (3.11), the asymptotic expansion of the zeroth-order Boys function is

$$F_0(T) \sim \frac{1}{2} \sqrt{\frac{\pi}{T}}. \quad (3.74)$$

Let  $\tau$  be the desired accuracy for the three-center ERI given in Eq. (3.73). In Ref. [86] it is shown that the ERI error tolerance can be represented by an exponential

fitting in terms of  $T$  as

$$\tau = \frac{1}{2} \sqrt{\frac{\pi}{T}} - F_0(T) \simeq e^{-(a+bT)}, \quad (3.75)$$

with  $a = 2.038972$  and  $b = 1.069227$  [86]. Rearranging Eq. (3.75) we find

$$T = \frac{-a - \ln \tau}{b} \quad (3.76)$$

Substituting  $T$  from Eq. (3.70) in Eq. (3.76) and setting  $r_\phi = |\vec{r} - \vec{C}|$ , we can now define an asymptotic radius for the primitive HGTF electrostatic potential (3.67) as:

$$r_\phi = \sqrt{\frac{-a - \min(\ln \tau, -10)}{\zeta_{\bar{c}}^{\min} b}} \quad (3.77)$$

with  $\zeta_{\bar{c}}^{\min}$  being the smallest auxiliary function set exponent at the atom. The changes on Eq. (3.77) with respect to Eq. (3.76) are for accuracy reasons. Since the HGTF electrostatic potential has an infinite extension due to the behavior of the Coulomb operator,  $r_\phi$  defines a *near-field* interaction region. For an orbital a finite extension is defined as:

$$r_\chi = \sqrt{\frac{\ln\left(\frac{d_{\min}}{\tau}\right)}{\zeta_\chi^{\min}}}. \quad (3.78)$$

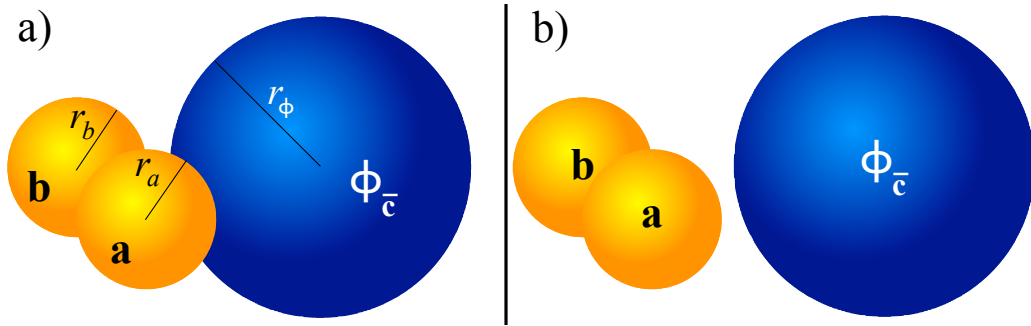


Figure 3.17: Conditions for the application of the asymptotic expansion of ERIs. a) One of the atoms overlaps with the near-field region of the potential  $\phi_{\bar{c}}(\vec{r})$  thus the asymptotic expansion is not feasible. b) Both atoms are outside the near-field region of the potential  $\phi_{\bar{c}}(\vec{r})$ , thus the asymptotic expansion can be applied.

This radius is the one defined for the numerical integration for the calculation of the exchange correlation potential [86]. Here,  $\tau$  is the desired accuracy for the integral calculation,  $d_{min}$  is the contraction coefficient for the primitive basis function with the smallest exponent,  $\zeta_{\chi}^{min}$ , contributing to the orbital  $\chi$ . For a given atom, the largest  $r_{\chi}$  defines its atomic radius. Thus, both  $r_{\phi}$  and  $r_{\chi}$  are atomic properties.

These radii define interaction regions in the following way: The asymptotic expansion for a three-center ERI  $\langle \mathbf{ab} || \bar{\mathbf{c}} \rangle$  is used when distance  $\overline{AC}$  is larger than  $r_a + r_{\phi}$  and distance  $\overline{BC}$  is larger than  $r_b + r_{\phi}$ , that is, the asymptotic expansion is used when both atoms are outside the near-field region of the electrostatic potential of the HGTF. These conditions are depicted in Figure 3.17. This idea defines the nearest neighbors for orbital products and potentials and is the foundation of the spatial division of a molecule in the asymptotic expansion as implemented in deMon2k. Distinct from the FMM, the division of space is not performed over a systematic hierarchy of mesh levels, but taking into account the extension of atomic orbitals and electrostatic potentials centered on atoms. The ERIs between near-neighbors are called *near-field ERIs* and are calculated by conventional recurrence relations [84,86]. The ERIs between far-neighbors are called *far-field ERIs* and for their calculation the asymptotic expansion in Eq. (3.73) is used.

### 3.8.1 Asymptotic expansion of the Kohn-Sham matrix elements

For the calculation of the ERIs in construction of the Kohn-Sham matrix the application of the asymptotic expansion yields the following result

$$\begin{aligned} \sum_{\bar{\mathbf{c}}} \langle \mathbf{ab} || x_{\bar{\mathbf{c}}} \bar{\mathbf{c}} \rangle &= \sum_{\bar{\mathbf{c}}}^{near} \langle \mathbf{ab} || x_{\bar{\mathbf{c}}} \bar{\mathbf{c}} \rangle + \sum_{\bar{\mathbf{c}}}^{far} \langle \mathbf{ab} || x_{\bar{\mathbf{c}}} \bar{\mathbf{c}} \rangle \\ &\sim \sum_{\bar{\mathbf{c}}}^{near} \langle \mathbf{ab} || x_{\bar{\mathbf{c}}} \bar{\mathbf{c}} \rangle + \langle \mathbf{ab} || \hat{\mathcal{A}} \rangle \end{aligned} \quad (3.79)$$

where the operator  $\hat{\mathcal{A}}$ , the asymptotic multipole operator, is defined as [86]

$$\hat{\mathcal{A}} = \sum_C^{far} \sum_{\bar{c} \in C} Q_C^{\bar{c}} \hat{\mathcal{A}}_C(\bar{c}) \quad (3.80)$$

with

$$Q_C^{\bar{c}} = \sum_{k \in \bar{c}} (-1)^{\bar{c}} \left( \frac{\pi}{\zeta_k} \right)^{\frac{3}{2}} x_k \quad (3.81)$$

and  $\hat{\mathcal{A}}_C(\bar{c})$  defined in Eq. (3.13). Here  $x_k$  refers to the Coulomb fitting coefficients or the sum of Coulomb and exchange-correlation coefficients. In Eq. (3.81)  $Q_C^{\bar{c}}$  collects all the scaled fitting coefficients of the auxiliary functions from atom  $C$  with the same angular momentum index  $\bar{c}$ . The limit of the sums in Eq. (3.79) refer to integrals belonging to the near- and far-field regions. Eq. (3.79) also shows that the calculation of the integrals in the near- and far-field can be independently done. However, in deMon2k these integrals are calculated in the same step since their calculation starts in the same way. This can be seen in the pathway diagram depicted in Figure 3.18 for the far-field contribution to the Kohn-Sham matrix elements. The diagram is read from the lower-left corner to the upper-right corner. It starts with the basic scaled integrals of the form:

$$[\bar{\mathbf{s}}|\hat{\mathcal{A}}_C(\bar{\mathbf{0}})]^{(n)} = \frac{2\pi}{\zeta_p} (-2\zeta_p)^n F_n(T) \quad (3.82)$$

with  $T = \zeta_p(\vec{P} - \vec{C})^2$ ,  $\vec{P}$  being the center of the orbital product  $\mathbf{ab}$ , as in Eq. (3.2), and  $(n)$  a scaling index similar as the one from Eq. (3.14). The vertical recurrence

$$\begin{array}{c} \langle \bar{\mathbf{r}}|\hat{\mathcal{A}} \rangle_{(u,v)} \xrightarrow{\mathbf{T}} \langle \mathbf{as}|\hat{\mathcal{A}} \rangle \xrightarrow{\mathbf{H}} K_{ab} \sim \langle \mathbf{ab}|\hat{\mathcal{A}} \rangle \\ \uparrow \mathbf{C} \\ [\bar{\mathbf{s}}|\hat{\mathcal{A}}_C(\bar{\mathbf{0}})]^{(n)} \xrightarrow{\mathbf{V}} [\bar{\mathbf{r}}|\hat{\mathcal{A}}_C(\bar{\mathbf{c}})] \xrightarrow{\mathbf{S}} [\bar{\mathbf{r}}|\hat{\mathcal{A}}] \end{array}$$

Figure 3.18: Pathway diagram for the calculation of the far-field ERIs for the Kohn-Sham matrix elements using the asymptotic expansion.

step (V) increases the angular momentum of the basic integral in the following way

$$[\bar{\mathbf{r}} + \bar{\mathbf{1}}_i | \hat{\mathcal{A}}_C(\bar{\mathbf{0}})]^{(n)} = (P_i - C_i) [\bar{\mathbf{r}} | \hat{\mathcal{A}}_C(\bar{\mathbf{0}})]^{(n+1)} + N_i(\bar{\mathbf{r}}) [\bar{\mathbf{r}} - \bar{\mathbf{1}}_i | \hat{\mathcal{A}}_C(\bar{\mathbf{0}})]^{(n+1)}. \quad (3.83)$$

where  $i$  is  $x$ ,  $y$  or  $z$  and  $N_i(\bar{\mathbf{r}})$  as defined in Eq. (3.68). Using the relation

$$[\bar{\mathbf{r}} | \hat{\mathcal{A}}_C(\bar{\mathbf{c}})] = (-1)^{\bar{c}} [\bar{\mathbf{r}} + \bar{\mathbf{c}} | \hat{\mathcal{A}}_C(\bar{\mathbf{0}})], \quad (3.84)$$

where  $(-1)^{\bar{c}} = (-1)^{\bar{c}_x + \bar{c}_y + \bar{c}_z}$ , that can be obtained straightforwardly from the definition of the operator  $\hat{\mathcal{A}}_C$  in Eq. (3.13), we can shift angular momentum index values from the Hermite function  $\bar{\mathbf{r}}$  to the operator  $\hat{\mathcal{A}}_C(\bar{\mathbf{c}})$ , resulting in integrals of the type  $[\bar{\mathbf{r}} | \hat{\mathcal{A}}_C(\bar{\mathbf{c}})]$ . The next step is the summation (S) over the auxiliary functions on atoms  $C$  in the far-field region

$$[\bar{\mathbf{r}} | \hat{\mathcal{A}}] = \sum_C^{far} \sum_{\bar{\mathbf{c}} \in C} Q_C^{\bar{\mathbf{c}}} [\bar{\mathbf{r}} | \hat{\mathcal{A}}_C(\bar{\mathbf{c}})]. \quad (3.85)$$

The following steps, contraction (C), transformation (T) and horizontal recurrence (H) relations, are analogous to the ones in the integrals for the near-field region (see section 3.6.1). These steps contract and transform the one-center function  $\bar{\mathbf{r}}$  to the orbital product  $\mathbf{ab}$  in the target integral. Since all these steps are outside the three-center loop they have a formal quadratic scaling. This discussion shows that the complexity of the far-field ERI calculation for Kohn-Sham matrix elements is reduced to the complexity of nuclear attraction integrals thanks to the asymptotic expansion.

### 3.8.2 Asymptotic expansion of the Coulomb vector elements

The application of the asymptotic expansion for the Coulomb vector yields the following equation:

$$\begin{aligned}
\sum_{a,b} P_{ab} \langle \mathbf{ab} \parallel \bar{\mathbf{c}} \rangle &= \sum_{a,b}^{near} P_{ab} \langle \mathbf{ab} \parallel \bar{\mathbf{c}} \rangle + \sum_{a,b}^{far} P_{ab} \langle \mathbf{ab} \parallel \bar{\mathbf{c}} \rangle \\
&\sim \sum_{a,b}^{near} P_{ab} \langle \mathbf{ab} \parallel \bar{\mathbf{c}} \rangle + \\
&\quad (-1)^{\bar{c}} \left( \frac{\pi}{\zeta_{\bar{c}}} \right)^{\frac{3}{2}} \sum_{\bar{a}} \sum_{u,v} P_{\bar{a}}^{(u,v)} \langle \bar{\mathbf{a}} \mid \hat{\mathcal{A}}_C(\bar{\mathbf{c}}) \rangle_{(u,v)}, \quad (3.86)
\end{aligned}$$

where  $(-1)^{\bar{c}} = (-1)^{\bar{c}_x + \bar{c}_y + \bar{c}_z}$ . The pathway diagram for the calculation of the far-field contribution to the Coulomb vector is depicted in Figure 3.19. The diagram is read from both ends toward the middle. On the left-hand side, the basic integral and the vertical recurrence step are the same as the ones in Eq. (3.82) and (3.83), respectively. The contraction step is given by

$$\langle \bar{\mathbf{a}} \mid \hat{\mathcal{A}}_C(\bar{\mathbf{c}}) \rangle_{(u,v)} = \sum_k^{K_a} \sum_l^{K_b} \frac{\zeta_l^u}{(\zeta_k + \zeta_l)^v} d_k d_l \left[ \bar{\mathbf{a}}_{kl} \mid \hat{\mathcal{A}}_C(\bar{\mathbf{c}}) \right]. \quad (3.87)$$

with the  $(u, v)$  scaling explained in Eq. (3.6). From the upper-right corner, the density matrix elements have their angular momentum index shifted according to the inverse horizontal recurrence relation from Eq. (3.30) and (3.31). Next, the transformation recurrence relations from Eq. (3.32), (3.33) and (3.34) produce the final form of the density matrix elements in order to match the integral sum index. Finally, the far-field contribution to the Coulomb vector is calculated by

$$J_{\bar{c}} \sim (-1)^{\bar{c}} \left( \frac{\pi}{\zeta_{\bar{c}}} \right)^{\frac{3}{2}} \sum_{u,v} \sum_{\bar{a}} P_{\bar{a}}^{(u,v)} \langle \bar{\mathbf{a}} \mid \hat{\mathcal{A}}_C(\bar{\mathbf{c}}) \rangle_{(u,v)} \quad (3.88)$$

$$\begin{array}{c}
\langle \bar{\mathbf{a}} \mid \hat{\mathcal{A}}_C(\bar{\mathbf{c}}) \rangle_{(u,v)} \xrightarrow{\mathbf{S}} J_{\bar{c}} \sim (-1)^{\bar{c}} \left( \frac{\pi}{\zeta_{\bar{c}}} \right)^{\frac{3}{2}} \sum_{u,v} \sum_{\bar{a}} P_{\bar{a}}^{(u,v)} \langle \bar{\mathbf{a}} \mid \hat{\mathcal{A}}_C(\bar{\mathbf{c}}) \rangle_{(u,v)} \xleftarrow{\mathbf{S}} P_{\bar{a}}^{(u,v)} \xleftarrow{\mathbf{T}^{-1}} P_{as} \xleftarrow{\mathbf{H}^{-1}} P_{ab} \\
\uparrow \mathbf{C} \\
[\bar{\mathbf{s}} \mid \hat{\mathcal{A}}_C(\bar{\mathbf{0}})]^{(n)} \xrightarrow{\mathbf{V}} [\bar{\mathbf{a}} \mid \hat{\mathcal{A}}_C(\bar{\mathbf{c}})]
\end{array}$$

Figure 3.19: Pathway diagram for the calculation of the electron repulsion integral for the Coulomb vector using the asymptotic expansion.

Since all the auxiliary functions in a given atom  $C$  share the same center, the far-field contribution for  $J_{\bar{c}}$  has to be calculated only once for all the auxiliary functions with angular momentum index  $\bar{\mathbf{c}} = (\bar{c}_x, \bar{c}_y, \bar{c}_z)$ .

# Chapter 4

## Double asymptotic expansion of electron repulsion integrals

The difficulties arising in the calculation of the electrostatic interaction integrals shown in the previous chapter inspired the development of new algorithms to increase the performance of the computation of this kind of integrals. The following chapters show the development, implementation and benchmarking of the double asymptotic expansion for electronic repulsion integrals (ERI) and the asymptotic expansion of nuclear attraction-like integrals, which result in the reduction of computational time for electrostatic interaction integrals in deMon2k without modifying the accuracy and convergence achieved by the previous implementations.

### 4.1 A second asymptotic expansion for ERIs

Based on the discussion in chapter 3, we now seek for a further simplification of the asymptotic three-center ERI calculation. A promising approach is given by the series expansion [120] of  $1/|\vec{r} - \vec{C}|$  in the nuclear attraction-like operator (3.13)

$$\frac{1}{|\vec{r} - \vec{C}|} = \frac{1}{|(\vec{A} - \vec{C}) + \vec{r}_A|} \quad \text{or} \quad \frac{1}{|\vec{r} - \vec{C}|} = \frac{1}{|(\vec{B} - \vec{C}) + \vec{r}_B|}, \quad (4.1)$$

where  $\vec{r}_A = \vec{r} - \vec{A}$  and  $\vec{r}_B = \vec{r} - \vec{B}$ . Due to the far-field integral definition from Eq. (3.77) and (3.78), it always holds that  $|\vec{r}_A| \ll |\vec{A} - \vec{C}|$  and  $|\vec{r}_B| \ll |\vec{B} - \vec{C}|$ . Thus, a

Taylor series expansion of  $1/|\vec{r} - \vec{C}|$  on center  $\vec{A}$  is feasible and yields

$$\frac{1}{|\vec{r} - \vec{C}|} = \frac{1}{|\vec{A} - \vec{C} + \vec{r}_A|} \sim \sum_{m_x, m_y, m_z} (-1)^m \hat{M}_A(m_x, m_y, m_z) T_{AC}(m_x, m_y, m_z) \quad (4.2)$$

with  $m = m_x + m_y + m_z$ .  $\hat{M}_A$  denotes a multipole-type operator of the form

$$\hat{M}_A(m_x, m_y, m_z) = \frac{x_A^{m_x} y_A^{m_y} z_A^{m_z}}{m_x! m_y! m_z!} \equiv \hat{M}_A(\mathbf{m}), \quad (4.3)$$

where  $i_A^{m_i} = (i - A_i)^{m_i}$  and  $i$  stands for  $x$ ,  $y$  and  $z$ .  $T_{AC}$  is the diatomic Cartesian  $T$  tensor

$$T_{AC}(m_x, m_y, m_z) = \left( \frac{\partial}{\partial C_x} \right)^{m_x} \left( \frac{\partial}{\partial C_y} \right)^{m_y} \left( \frac{\partial}{\partial C_z} \right)^{m_z} \frac{1}{|\vec{A} - \vec{C}|} \equiv T_{AC}(\mathbf{m}), \quad (4.4)$$

as introduced by Stone [128]. Inserting Eq. (4.2) in Eq. (3.73) we can define a new asymptotic expansion of the three-center ERI on  $\vec{A}$  as

$$\begin{aligned} \langle \mathbf{ab} || \bar{\mathbf{c}} \rangle^A &= \left( \frac{\pi}{\zeta_{\bar{\mathbf{c}}}} \right)^{\frac{3}{2}} \left\langle \mathbf{ab} \left| \sum_{m_x, m_y, m_z} (-1)^m \hat{M}_A(\mathbf{m}) T_{AC}(\mathbf{m} + \bar{\mathbf{c}}) \right. \right\rangle \\ &= \left( \frac{\pi}{\zeta_{\bar{\mathbf{c}}}} \right)^{\frac{3}{2}} \sum_{m_x, m_y, m_z} (-1)^m T_{AC}(\mathbf{m} + \bar{\mathbf{c}}) \langle \mathbf{a} | \hat{M}_A(\mathbf{m}) | \mathbf{b} \rangle \\ &= \left( \frac{\pi}{\zeta_{\bar{\mathbf{c}}}} \right)^{\frac{3}{2}} \sum_{m_x, m_y, m_z} \frac{(-1)^m}{m_x! m_y! m_z!} T_{AC}(\mathbf{m} + \bar{\mathbf{c}}) \langle \mathbf{a} | x_A^{m_x} y_A^{m_y} z_A^{m_z} | \mathbf{b} \rangle \\ &= \left( \frac{\pi}{\zeta_{\bar{\mathbf{c}}}} \right)^{\frac{3}{2}} \sum_{m_x, m_y, m_z} \frac{(-1)^m}{m_x! m_y! m_z!} T_{AC}(\mathbf{m} + \bar{\mathbf{c}}) \langle \mathbf{a} + \mathbf{m} | \mathbf{b} \rangle, \end{aligned} \quad (4.5)$$

where  $T_{AC}(\mathbf{m} + \bar{\mathbf{c}}) = T_{AC}(m_x + \bar{c}_x, m_y + \bar{c}_y, m_z + \bar{c}_z)$  and the angular momentum index of  $\mathbf{a} + \mathbf{m}$  is  $(a_x + m_x, a_y + m_y, a_z + m_z)$ . An equivalent equation is obtained for the series expansion on center  $\vec{B}$

$$\langle \mathbf{ab} || \bar{\mathbf{c}} \rangle^B = \left( \frac{\pi}{\zeta_{\bar{\mathbf{c}}}} \right)^{\frac{3}{2}} \sum_{m_x, m_y, m_z} \frac{(-1)^m}{m_x! m_y! m_z!} T_{BC}(\mathbf{m} + \bar{\mathbf{c}}) \langle \mathbf{a} | \mathbf{b} + \mathbf{m} \rangle. \quad (4.6)$$

Since the asymptotic expansion in Eq. (4.5) and (4.6) is done after the asymptotic expansion in Eq. (3.73), the name *double asymptotic expansion* is appropriate for this new development. The superscript of the integral on the left-hand side of Eqs. (4.5) and (4.6) denotes the center on which the Taylor series is expanded. The use of different expansion centers is a consequence of the Gaussian Product theorem from Eq. (3.1). The product center of two GTOs is closer to the center of the GTO with larger exponent, as can be seen in Figure 3.1. As a consequence, the Taylor series expansion on center  $\vec{A}$  considers only the primitive products nearest to  $\vec{A}$  in the calculation of  $\langle \mathbf{ab} || \bar{\mathbf{c}} \rangle^A$  whereas the series expansion on center  $\vec{B}$  considers the primitive products nearest to  $\vec{B}$  in the calculation of  $\langle \mathbf{ab} || \bar{\mathbf{c}} \rangle^B$ . This yields faster convergence of the Taylor series expansion and ensures high accuracy with relatively few terms. Thus, the calculation of the far-field three-center ERIs using the double asymptotic expansion can be expressed as

$$\langle \mathbf{ab} || \bar{\mathbf{c}} \rangle \sim \langle \mathbf{ab} || \bar{\mathbf{c}} \rangle^A + \langle \mathbf{ab} || \bar{\mathbf{c}} \rangle^B \quad (4.7)$$

For the sake of simplicity, the equations showing the application of the double asymptotic expansion will be referred to center  $\vec{A}$ . Equivalent equations for center  $\vec{B}$  can be derived straightforwardly. From Eq. (4.5) and (4.6) it is seen that using the double asymptotic expansion reduces the three-center ERIs to a sum of modified two-center overlap integrals over Cartesian GTOs. A number of important features can be deduced from the double asymptotic expansion of the three-center ERIs:

1. The conditions for the application of the double asymptotic ERI expansion are exactly the same as the ones for the application of the asymptotic ERI expansion. Therefore, simple atomic distance criteria can be used to enable the double asymptotic ERI expansion.
2. Because the overlap integrals can be calculated analytically, the double asymptotic ERI expansion does not require the calculation of the non-analytic Boys function.
3. The far-field HGTF calculation is moved to the atomic level since the auxiliary function information is now collected in the diatomic quantity  $T_{AC}(\mathbf{m})$ ,

Eq. (4.4). Since  $T_{AC}(\mathbf{m})$  is not included in the integral calculation, it does not contribute to the formal scaling of the integral. As a consequence, the formal scaling of the far-field ERI calculation is reduced to  $N^2$  where  $N$  is the number of basis functions.

4. The formal scaling of the double asymptotic ERI expansion can be further reduced by screening of the modified overlap integral calculation. As a result, linear scaling is always reached for the far-field ERI calculation if a sufficiently large number of far-field ERIs have to be calculated.
5. An additional advantage of the double asymptotic expansion with respect to fast multipole methods (FMM) is that there is no need of translation nor rotation operators. The only source for charge distribution center displacements is in the choice of the asymptotic expansion center which moves from the primitive product center to one of the orbital centers. This yields high accuracy with considerably fewer terms in the double asymptotic expansion sum than in the corresponding FMM expansion.

What remains to do is to define the expansion order of the multipole sum for the double asymptotic expansion in Eq. (4.2). From our experience, applying the double asymptotic expansion up to 8<sup>th</sup> order is proper to obtain energies consistent with the standard integral calculation. However, the farther away the asymptotic expansion center lies from the auxiliary function center  $\vec{C}$ , the faster is the convergence of the asymptotically expanded integral. Knowing this, one can expect that a reduction in the order of the double asymptotic expansion leads to a still accurate calculation of the integrals with enhanced performance.

In order to take advantage of this fact a new radius, from now on referred to as the *cut-off radius*, is defined. This radius will represent a new region for the far-field from beyond which the double asymptotic expansion is performed only up to a reduced expansion order. Using the result of Eq. (4.5) we write a  $k^{\text{th}}$ -order term of a simple three-center ERI. In order to reduce the double asymptotic expansion order to  $k$ , this term shall have a value below a threshold, namely  $\tau_{\text{cut}}$ . For example, using

$|\vec{A} - \vec{C}| = A_z - C_z$  and  $(m_x, m_y, m_z) = (0, 0, k)$  we have

$$\left(\frac{\pi}{\zeta_{\bar{c}}}\right)^{\frac{3}{2}} \frac{(-1)^k}{k!} \left[ \left(\frac{\partial}{\partial C_z}\right)^k \frac{1}{A_z - C_z} \right] \langle \mathbf{s} + \mathbf{k} | \mathbf{s} \rangle = \left(\frac{\pi}{\zeta_{\bar{c}}}\right)^{\frac{3}{2}} \frac{(-1)^k}{(A_z - C_z)^k} \langle \mathbf{s} + \mathbf{k} | \mathbf{s} \rangle \leq \tau_{cut} \quad (4.8)$$

where the angular momentum index of  $\mathbf{s} + \mathbf{k}$  is  $(0, 0, k)$ . Setting  $d_{cut} = A_z - C_z$  we can solve Eq. (4.8) for  $d_{cut}$  as

$$\sqrt{{}^{(k+1)} \left(\frac{\pi}{\zeta_{\bar{c}}}\right)^{\frac{3}{2}} \frac{(-1)^k \langle \mathbf{s} + \mathbf{k} | \mathbf{s} \rangle}{\tau_{cut}}} \leq d_{cut}. \quad (4.9)$$

In order to match this result with accuracy requirements implemented in the code, we define the new cut-off radius as

$$d_{cut} = \sqrt{{}^{(k+1)} \left(\frac{\pi}{\zeta_{\bar{c}}^{min}}\right)^{\frac{3}{2}} \frac{S^{max}}{\tau_{cut}}}. \quad (4.10)$$

Thus,  $k$  is the highest order in the double asymptotic expansion that will be applied when the distance  $|\vec{A} - \vec{C}|$  is greater than  $d_{cut}$ ,  $\zeta_{\bar{c}}^{min}$  is the smallest exponent in the auxiliary function sets on atom  $C$  and  $S^{max}$  is the largest tensor norm generated by the modified overlap integrals  $\langle \mathbf{a} + \mathbf{m} | \mathbf{b} \rangle$ . As implemented in our present code, the cut-off order  $k$  is set to 2.

## 4.2 Double asymptotic expansion of the Kohn-Sham matrix elements

Applying the double asymptotic expansion, Eq. (4.5), for the far-field contribution of the Kohn-Sham matrix elements, Eq. (3.79), we find

$$\begin{aligned}
\sum_{\bar{c}}^{far} \langle \mathbf{a}\mathbf{b} | | \bar{c} \rangle x_{\bar{c}} &\sim \sum_{\bar{C}}^{far} \sum_{\bar{c} \in \bar{C}} \left( \frac{\pi}{\zeta_{\bar{c}}} \right)^{\frac{3}{2}} \sum_{m_x, m_y, m_z} \frac{(-1)^m}{m_x! m_y! m_z!} T_{AC}(\mathbf{m} + \bar{c}) \langle \mathbf{a} + \mathbf{m} | \mathbf{b} \rangle x_{\bar{c}} \\
&= \sum_{m_x, m_y, m_z} \frac{(-1)^m}{m_x! m_y! m_z!} \sum_{\bar{C}}^{far} \sum_{\bar{c} \in \bar{C}} \left( \frac{\pi}{\zeta_{\bar{c}}} \right)^{\frac{3}{2}} x_{\bar{c}} T_{AC}(\mathbf{m} + \bar{c}) \langle \mathbf{a} + \mathbf{m} | \mathbf{b} \rangle \\
&\equiv \sum_{m_x, m_y, m_z} Q_A(\mathbf{m}) \langle \mathbf{a} + \mathbf{m} | \mathbf{b} \rangle, \tag{4.11}
\end{aligned}$$

with

$$Q_A(\mathbf{m}) = \frac{(-1)^m}{m_x! m_y! m_z!} \sum_{\bar{C}}^{far} \sum_{\bar{c} \in \bar{C}} \left( \frac{\pi}{\zeta_{\bar{c}}} \right)^{\frac{3}{2}} x_{\bar{c}} T_{AC}(\mathbf{m} + \bar{c}), \tag{4.12}$$

where the *far* sum limit in Eq. (4.12) indicates that only atoms  $C$  in the far-field of atoms  $A$  and  $B$  are taken into account for the sum. The pathway diagram for the calculation of the Kohn-Sham matrix using the double asymptotic expansion is given in Figure 4.1. The integral calculation starts in the lower-left corner with the basic overlap integrals given in Eq. (3.5). In the following contraction step (C) the primitive overlap integrals are contracted and scaled with orbital exponents as shown in Eq. (3.6). The resulting  $(u, v)$ -scaled overlap integrals increase the angular momentum index of orbital  $\mathbf{a}$  using the vertical recurrence relation (V) from Eq. (3.7).

$$\begin{array}{c}
\langle \mathbf{s} | \mathbf{s} \rangle_{(u,v)} \xrightarrow{\text{V}} \langle \mathbf{a} + \mathbf{m} + \mathbf{b} | \mathbf{s} \rangle \xrightarrow{\text{H}} \langle \mathbf{a} + \mathbf{m} | \mathbf{b} \rangle \xrightarrow{\text{S}} K_{ab} \sim \sum_{m_x, m_y, m_z} Q_A(\mathbf{m}) \langle \mathbf{a} + \mathbf{m} | \mathbf{b} \rangle \\
\begin{array}{c} \uparrow \\ \text{C} \\ \uparrow \\ [\mathbf{s} | \mathbf{s}] \end{array} \qquad \qquad \qquad \begin{array}{c} \uparrow \\ \text{S} \\ \uparrow \\ Q_A(\mathbf{m}) \end{array}
\end{array}$$

Figure 4.1: Pathway diagram for the calculation of the electron repulsion integral of the Kohn-Sham matrix elements using the double asymptotic expansion.

The vertical recurrence step yields overlap integrals that possess the total angular momentum index at the center of orbital  $\mathbf{a}$ . This can be shifted with the horizontal recurrence relation (H), Eq. (3.8), to obtain the modified target overlap integrals. The second part of the diagram starts in the lower-right corner with the calculation of the atomic quantity  $Q_A(\mathbf{m})$ , Eq. (4.12). This step is performed independently from the modified overlap integral calculation. Once both the modified overlap integrals and  $Q_A(\mathbf{m})$  are calculated, the sum step (S) is performed in order to obtain the target Kohn-Sham matrix far-field contribution.

The pseudocode for the calculation of the far-field contribution to the Kohn-Sham matrix elements is depicted in Figure 4.2. In the first step, the  $Q_A(\mathbf{m})$  field, Eq. (4.12), is initialized. A far-field condition check between atom  $A$  and  $C$  is performed. If the far-field condition is fulfilled then the diatomic Cartesian tensor  $T_{AC}(\mathbf{m}+\bar{\mathbf{c}})$ , Eq. (4.4), and the corresponding  $Q_{AC}(\mathbf{m})$

```

DO ATOM_A
  Initialize  $Q_A(\mathbf{m}) = 0$ 
DO ATOM_C
  IF distance  $\overline{AC}$  is greater than  $r_a + r_\phi$  calculate
     $T_{AC}(\mathbf{m}+\bar{\mathbf{c}})$  and  $Q_{AC}(\mathbf{m})$ ; add  $Q_A(\mathbf{m}) \leftarrow Q_A(\mathbf{m}) + Q_{AC}(\mathbf{m})$ 
END DO
DO ATOM_B
  IF distance  $\overline{AB}$  is greater than  $r_a + r_b$  go to next ATOM_B
  Initialize  $Q_S(\mathbf{m}) = Q_A(\mathbf{m})$ 
DO ATOM_C
  IF distance  $\overline{AC}$  is greater than  $r_a + r_\phi$  but
    distance  $\overline{BC}$  is smaller than or equal  $r_b + r_\phi$  subtract
     $Q_S(\mathbf{m}) \leftarrow Q_S(\mathbf{m}) - Q_{AC}(\mathbf{m})$ 
END DO
DO SHELL_A
  DO SHELL_B
    Calculate  $\langle \mathbf{a} + \mathbf{m} | \mathbf{b} \rangle$ 
    Sum  $K_{ab} \leftarrow K_{ab} + \sum_{m_x, m_y, m_z} Q_S(\mathbf{m}) \langle \mathbf{a} + \mathbf{m} | \mathbf{b} \rangle$ 
  END DO
END DO
END DO
END DO

```

Figure 4.2: Pseudocode for the calculation of the electron repulsion integral for the Kohn-Sham matrix using the double asymptotic expansion.

$$Q_{AC}(\mathbf{m}) = \frac{(-1)^m}{m_x!m_y!m_z!} \sum_{\bar{\mathbf{c}} \in C} \left( \frac{\pi}{\zeta_{\bar{\mathbf{c}}}} \right)^{\frac{3}{2}} x_{\bar{\mathbf{c}}} T_{AC}(\mathbf{m} + \bar{\mathbf{c}}), \quad (4.13)$$

are built. Then,  $Q_{AC}(\mathbf{m})$  is added to  $Q_A(\mathbf{m})$ . After this loop  $Q_A(\mathbf{m})$  includes contributions from every atom  $C$  in the far-field region of atom  $A$  since only the far-field condition between atom  $A$  and  $C$  is checked. After  $Q_A(\mathbf{m})$  is calculated the loop over atom  $B$  is accessed. First, a screening procedure is performed in order to check if atoms  $A$  and  $B$  have a significant overlap. If this is the case, a work field  $Q_S(\mathbf{m})$  is initialized by  $Q_A(\mathbf{m})$ . The use of the work field  $Q_S(\mathbf{m})$  avoids operations with atomic fields inside the shell loops and keep as many operations as possible at the atomic level. A second far-field condition check involving now atoms  $A$ ,  $B$  and  $C$  is performed. For every atom  $C$  in the far-field region of atom  $A$  but not in the far-field region of atom  $B$ , the corresponding  $Q_{AC}(\mathbf{m})$ , Eq. (4.13), is subtracted from  $Q_S(\mathbf{m})$ . This ensures that  $Q_S(\mathbf{m})$  contains only contributions from atoms  $C$  in the far-field regions of both atoms,  $A$  and  $B$ . Thus, the pseudocode structure in Figure 4.2 guarantees the efficient calculation of  $Q_A(\mathbf{m})$  and  $Q_S(\mathbf{m})$  even for hundreds of thousands of atoms. In the second part of the loop structure the modified overlap integrals between atom  $A$  and  $B$  are calculated. The calculated modified overlap integrals are summed together with the corresponding  $Q_S(\mathbf{m})$  elements and added to the Kohn-Sham matrix element. As a result, the far-field ERI calculation for the Kohn-Sham matrix elements is basically reduced to the calculation of modified overlap integrals.

### 4.3 Double asymptotic expansion of the Coulomb vector elements

The double asymptotic expansion, Eq. (4.5) applied to the far-field contributions of the Coulomb vector, Eq. (3.86), yields

$$\sum_{a,b}^{far} P_{ab} \langle \mathbf{a}\mathbf{b} || \bar{\mathbf{c}} \rangle \sim \sum_a^{far} \sum_b^{far} P_{ab} \left( \frac{\pi}{\zeta_{\bar{\mathbf{c}}}} \right)^{\frac{3}{2}} \sum_{m_x, m_y, m_z} \frac{(-1)^m}{m_x!m_y!m_z!} T_{AC}(\mathbf{m} + \bar{\mathbf{c}}) \langle \mathbf{a} + \mathbf{m} | \mathbf{b} \rangle \quad (4.14)$$

where the *far* sum limit in Eq. (4.14) indicates that only orbitals in the far field of atom  $C$  are taken into account for the sum. In order to take advantage of the diatomic

nature of  $T_{AC}(\mathbf{m} + \bar{\mathbf{c}})$ , Eq. (4.14) is rewritten as

$$\begin{aligned} \sum_{a,b}^{far} P_{ab} \langle \mathbf{a} \mathbf{b} | | \bar{\mathbf{c}} \rangle &\sim \left( \frac{\pi}{\zeta \bar{c}} \right)^{\frac{3}{2}} \sum_{m_x, m_y, m_z}^{far} \sum_{A,B} T_{AC}(\mathbf{m} + \bar{\mathbf{c}}) \frac{(-1)^m}{m_x! m_y! m_z!} \sum_{a,b} P_{ab} \langle \mathbf{a} + \mathbf{m} | \mathbf{b} \rangle \\ &\equiv \left( \frac{\pi}{\zeta \bar{c}} \right)^{\frac{3}{2}} \sum_{A,B}^{far} \sum_{m_x, m_y, m_z} T_{AC}(\mathbf{m} + \bar{\mathbf{c}}) F_C(\mathbf{m}) \end{aligned} \quad (4.15)$$

where the sum  $\sum_{a,b}^{far}$  has been split in  $\sum_{A,B}^{far} \sum_{a,b}$  and we have introduced

$$F_C(\mathbf{m}) = \frac{(-1)^m}{m_x! m_y! m_z!} \sum_{a,b} P_{ab} \langle \mathbf{a} + \mathbf{m} | \mathbf{b} \rangle. \quad (4.16)$$

The subscript in  $F_C(\mathbf{m})$  remains since every atom  $C$  has a different *far* field environment, thus different atoms  $A$  and  $B$  in the sum definitions. The pathway diagram for the calculation of the far-field contribution to the Coulomb vector elements given by the double asymptotic expansion is depicted in Figure 4.3. The first part of the diagram starts in the lower-left corner with the calculation of the basic overlap integral. As this diagram shows, the calculation of the modified overlap integrals is identical to the ones for the Kohn-Sham matrix elements (Figure 4.1): The calculation of the basic overlap integral, Eq. (3.5), is followed by the contraction (C), Eq. (3.6), vertical recurrence (V), Eq. (3.7), and horizontal recurrence (H), Eq. (3.8), steps. In addition to the calculation of the modified overlap integrals, a gathering step (G) is performed in which  $F_C(\mathbf{m})$  is built according to Eq. (4.16). The second part of the diagram starts in the lower-right corner with the calculation of the atomic quantity  $T_{AC}(\mathbf{m} + \bar{\mathbf{c}})$ , Eq. (4.4). In the summation step (S), the previously calculated  $F_C(\mathbf{m})$

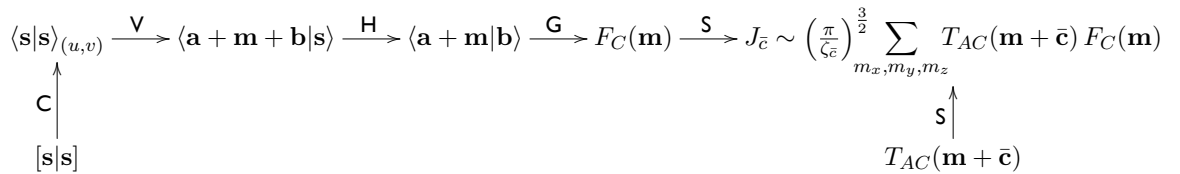


Figure 4.3: Pathway diagram for the calculation of the electron repulsion integral of the Coulomb vector using the double asymptotic expansion.

and  $T_{AC}(\mathbf{m} + \bar{\mathbf{c}})$  elements are summed together and the result added to the corresponding Coulomb vector element.

The pseudocode for the calculation of the far-field contributions to the Coulomb vector is shown in Figure 4.4. The first step is the initialization of the atomic field  $F_C(\mathbf{m})$ , Eq. (4.16). Then, the modified overlap integrals between atom  $A$  and  $B$  are calculated. Only if the overlap between the atomic pair is significant, the diatomic work field  $F_{AB}(\mathbf{m})$  is initialized and the modified overlap integrals calculated. The work field  $F_{AB}(\mathbf{m})$  is built as follows

$$F_{AB}(\mathbf{m}) = \frac{(-1)^m}{m_x!m_y!m_z!} \sum_{a \in A} \sum_{b \in B} P_{ab} \langle \mathbf{a} + \mathbf{m} | \mathbf{b} \rangle. \quad (4.17)$$

```

DO ATOM_A
Initialize  $F_C(\mathbf{m}) = 0$ 
DO ATOM_B
IF distance  $\overline{AB}$  is greater than  $r_a + r_b$  go to next ATOM_B
Initialize  $F_{AB}(\mathbf{m}) = 0$ 
DO SHELL_A
DO SHELL_B
Read  $P_{ab}$ 
Calculate  $\langle \mathbf{a} + \mathbf{m} | \mathbf{b} \rangle$  and build  $F_{AB}(\mathbf{m})$ 
END DO
END DO
DO ATOM_C
IF distance  $\overline{AC}$  is greater than  $r_a + r_\phi$  and
distance  $\overline{BC}$  is greater than  $r_b + r_\phi$  add
 $F_C(\mathbf{m}) \leftarrow F_C(\mathbf{m}) + F_{AB}(\mathbf{m})$ 
END DO
END DO
DO ATOM_C
IF distance  $\overline{AC}$  is greater than  $r_a + r_\phi$  calculate
 $T_{AC}(\mathbf{m} + \bar{\mathbf{c}})$  and sum
 $J_{\bar{\mathbf{c}}} \leftarrow J_{\bar{\mathbf{c}}} + \left(\frac{\pi}{\zeta_{\bar{\mathbf{c}}}}\right)^{\frac{3}{2}} \sum_{m_x, m_y, m_z} T_{AC}(\mathbf{m} + \bar{\mathbf{c}}) F_C(\mathbf{m})$ .
END DO
END DO

```

Figure 4.4: Pseudocode for the calculation of the electron repulsion integral for the Coulomb vector using the double asymptotic expansion.

Different from  $F_C(\mathbf{m})$ ,  $F_{AB}(\mathbf{m})$  collects the products from *all* shell combinations, since no information about the far field of  $C$  has still been analyzed. The work field  $F_{AB}(\mathbf{m})$  allows the algorithm to store all the information from the shell loops in a diatomic field and use it later in the atomic loops. After finishing the shell loops, the far-field condition between atoms  $A$ ,  $B$  and  $C$  is checked. If atoms  $A$  and  $B$  are both in the far field of  $C$ , the corresponding  $F_{AB}(\mathbf{m})$  is added to  $F_C(\mathbf{m})$ . Thus,  $F_C(\mathbf{m})$  is built only with contributions from atoms  $A$  and  $B$  that are both in the far-field region of atom  $C$ . Finally, after the loop over atom  $B$ , the far-field contributions to the Coulomb vector elements are built from the product of  $T_{AC}(\mathbf{m} + \bar{\mathbf{c}})$  and  $F_C(\mathbf{m})$  in a diatomic loop.

## 4.4 Asymptotic expansion of nuclear attraction integrals

The nuclear attraction integral (NAI) given in Eq. (3.12) resembles very much the asymptotically expanded three-center ERI in Eq. (3.73). It is possible to use the arguments in the beginning of this chapter to obtain an asymptotic form of the NAI. Applying Eq. (4.2) on Eq. (3.12) yields

$$\left\langle \mathbf{ab} \left| \frac{Z_C}{|\vec{r} - \vec{C}|} \right. \right\rangle \sim \sum_{m_x, m_y, m_z} \frac{(-1)^m}{m_x! m_y! m_z!} Z_C T_{AC}(\mathbf{m}) \langle \mathbf{a} + \mathbf{m} | \mathbf{b} \rangle. \quad (4.18)$$

An interesting application of this expansion comes in the framework of the point charge embedding scheme implemented in deMon2k. The integrals arising from such implementation have the same form as NAIs. It is common to build systems which contain large numbers of embedding point charges in research of extended crystalline systems [129] or in so-called quantum mechanics / molecular mechanics (QM/MM) studies [130] of very large biomolecules [131].

The introduction of embedding point charges,  $q_D$ , modifies the form of the energy

expression to

$$E^{QM/MM} = E^{QM} + \sum_{a,b}^{QM} \sum_D^{MM} P_{ab} \left\langle \mathbf{ab} \left| \frac{q_D}{|\vec{r} - \vec{D}|} \right. \right\rangle + \sum_A^{QM} \sum_D^{QM} \frac{Z_A q_D}{|\vec{A} - \vec{D}|}, \quad (4.19)$$

where  $E^{QM}$  is the energy of the isolated QM system as given in Eq. (2.6). Thus, the embedding point charges modify the core Hamiltonian matrix elements as follows

$$H_{ab}^{QM/MM} = H_{ab}^{QM} + H_{ab}^{MM} = H_{ab}^{QM} + \sum_D^{MM} \left\langle \mathbf{ab} \left| \frac{q_D}{|\vec{r} - \vec{D}|} \right. \right\rangle. \quad (4.20)$$

$H_{ab}^{QM}$  is a core Hamiltonian matrix element of the isolated QM system as given in Eq. (2.7). The algorithm for the calculation of the embedding contributions to the core Hamiltonian matrix is the same as the one for the nuclear attraction integrals from section 3.5. The difference is that, instead of positive nuclear charges, these integrals deal with embedding charges that can be positive or negative.

Since the purpose of the point charge embedding is to represent the electrostatic behavior of a very large region, the use of the asymptotic expansion is ideal for the calculations required for Eq. (4.20) because the calculation of the core Hamiltonian matrix can rapidly become the bottleneck in DFT calculations when the number of embedding charges goes above the order of hundreds of thousands [131]. The asymptotic expansion of the embedding integrals for the core Hamiltonian matrix is

$$\sum_D^{MM} \left\langle \mathbf{ab} \left| \frac{q_D}{|\vec{r} - \vec{D}|} \right. \right\rangle \sim \sum_{m_x, m_y, m_z} Q_A^{MM}(\mathbf{m}) \langle \mathbf{a} + \mathbf{m} | \mathbf{b} \rangle \quad (4.21)$$

with

$$Q_A^{MM}(\mathbf{m}) = \sum_D^{MM} \frac{(-1)^m}{m_x! m_y! m_z!} q_D T_{AD}(\mathbf{m}). \quad (4.22)$$

The pathway diagram for the calculation of the far-field embedding contribution to the core Hamiltonian matrix elements is depicted in Figure 4.5. The first part of the diagram, the integral calculation, starts in the lower-left corner just as in the Kohn-Sham



tributions from every point charge  $D$  in the far-field region of atom  $A$  since only the far-field condition between atom  $A$  and point charge  $D$  is checked. Then, in the loop over atom  $B$ , a screening procedure between atom  $A$  and  $B$  is performed. If  $A$  and  $B$  have significant overlap, a work field  $Q_S^{MM}(\mathbf{m})$  is initialized by  $Q_A^{MM}(\mathbf{m})$ . The use of the work field  $Q_S^{MM}(\mathbf{m})$  avoids operations with atomic fields inside the shell loops and keep as many operations as possible at the atomic level. A second far-field condition check involving now atom  $A$  and  $B$  and point charge  $D$  is performed. For every point charge  $D$  in the far-field region of atom  $A$  but not in the far-field region of atom  $B$ , the corresponding  $Q_{AD}^{MM}(\mathbf{m})$  is subtracted from  $Q_S^{MM}(\mathbf{m})$ . This ensures that  $Q_S^{MM}(\mathbf{m})$  contains only contributions from charges  $D$  in the far-field regions of both atoms,  $A$  and  $B$ . This pseudocode structure allows an efficient calculation of the atomic quantity  $Q_A^{MM}(\mathbf{m})$  even for hundreds of thousands of point charges. In the second part of the loop structure the modified overlap integrals between atom  $A$  and  $B$  are calculated. The modified overlap integrals are summed together with the corresponding  $Q_S^{MM}(\mathbf{m})$  elements and added to the core Hamiltonian matrix element.

```

DO ATOM_A
  Initialize  $Q_A^{MM}(\mathbf{m}) = 0$ 
  DO POINT_D
    IF distance  $\overline{AD}$  is greater than  $r_a + r_d$  calculate
       $T_{AD}(\mathbf{m})$  and  $Q_{AD}^{MM}(\mathbf{m})$ ; add  $Q_A^{MM}(\mathbf{m}) \leftarrow Q_A^{MM}(\mathbf{m}) + Q_{AD}^{MM}(\mathbf{m})$ 
    END DO
  DO ATOM_B
    IF distance  $\overline{AB}$  is greater than  $r_a + r_b$  go to next ATOM_B
    Initialize  $Q_S^{MM}(\mathbf{m}) = Q_A^{MM}(\mathbf{m})$ 
    DO POINT_D
      IF distance  $\overline{AD}$  is greater than  $r_a + r_d$  but
        distance  $\overline{BD}$  is smaller than or equal  $r_b + r_d$  subtract
           $Q_S^{MM}(\mathbf{m}) \leftarrow Q_S^{MM}(\mathbf{m}) - Q_{AD}^{MM}(\mathbf{m})$ 
      END DO
    DO SHELL_A
      DO SHELL_B
        Calculate  $\langle \mathbf{a} + \mathbf{m} | \mathbf{b} \rangle$ 
        Sum  $H_{ab}^{MM} \leftarrow H_{ab}^{MM} + \sum_{m_x, m_y, m_z} Q_S^{MM}(\mathbf{m}) \langle \mathbf{a} + \mathbf{m} | \mathbf{b} \rangle$ 
      END DO
    END DO
  END DO
END DO

```

Figure 4.6: Pseudocode for the calculation of embedding integrals using the asymptotic expansion.

## 4.5 Double asymptotic expansion for ERI derivatives

The double asymptotic expansion has also been implemented for the electron repulsion integrals (ERI) derivatives. The derivative with respect to the  $x$  coordinate of  $\vec{A}$  within the ERI double asymptotic expansion, Eq. (4.5), is given by

$$\begin{aligned} \frac{\partial}{\partial A_x} \sum_{m_x, m_y, m_z} \frac{(-1)^m}{m_x! m_y! m_z!} T_{AC}(\mathbf{m} + \bar{\mathbf{c}}) \langle \mathbf{a} + \mathbf{m} | \mathbf{b} \rangle = \\ \sum_{m_x, m_y, m_z} \frac{(-1)^m}{m_x! m_y! m_z!} \left( \frac{\partial}{\partial A_x} T_{AC}(\mathbf{m} + \bar{\mathbf{c}}) \right) \langle \mathbf{a} + \mathbf{m} | \mathbf{b} \rangle + \\ \sum_{m_x, m_y, m_z} \frac{(-1)^m}{m_x! m_y! m_z!} T_{AC}(\mathbf{m} + \bar{\mathbf{c}}) \left( \frac{\partial \langle \mathbf{a} + \mathbf{m} | \mathbf{b} \rangle}{\partial A_x} \right). \end{aligned} \quad (4.24)$$

The derivative of  $T_{AC}(\mathbf{m} + \bar{\mathbf{c}})$  with respect to the  $x$  coordinate of center  $A$  is

$$\frac{\partial}{\partial A_x} T_{AC}(\mathbf{m} + \bar{\mathbf{c}}) = -\frac{\partial}{\partial C_x} T_{AC}(\mathbf{m} + \bar{\mathbf{c}}) = -T_{AC}(\mathbf{m} + \bar{\mathbf{c}} + \mathbf{1}_x). \quad (4.25)$$

According to Eq. (3.43) the derivative of the second term on the right-hand side of Eq. (4.24) is

$$\begin{aligned} \frac{\partial \langle \mathbf{a} + \mathbf{m} | \mathbf{b} \rangle}{\partial A_x} &= 2 \langle \mathbf{a} + \mathbf{m} + \mathbf{1}_x | \mathbf{b} \rangle_{(1)} - N_x(\mathbf{a} + \mathbf{m}) \langle \mathbf{a} + \mathbf{m} - \mathbf{1}_x | \mathbf{b} \rangle \\ &= 2 \langle \mathbf{a} + \mathbf{m} + \mathbf{1}_x | \mathbf{b} \rangle_{(1)} - N_x(\mathbf{a}) \langle \mathbf{a} + \mathbf{m} - \mathbf{1}_x | \mathbf{b} \rangle - \\ &\quad m_x \langle \mathbf{a} + \mathbf{m} - \mathbf{1}_x | \mathbf{b} \rangle, \end{aligned} \quad (4.26)$$

since  $N_x(\mathbf{a} + \mathbf{m}) = N_x(\mathbf{a}) + N_x(\mathbf{m})$  and  $N_x(\mathbf{m}) = m_x$  (see the description of Eq. (3.7) as a reference). The up-shift modified scaled integral is given by

$$\langle \mathbf{a} + \mathbf{m} | \mathbf{b} \rangle_{(1)} = \sum_k^{K_a} \sum_l^{K_b} d_k d_l \zeta_k [\mathbf{a}_k + \mathbf{m} | \mathbf{b}_l] \quad (4.27)$$

very similar as Eq. (3.44). Inserting Eq. (4.25) and (4.26) in Eq. (4.24) yields

$$\begin{aligned}
\frac{\partial}{\partial A_x} \sum_{m_x, m_y, m_z} \frac{(-1)^m}{m_x! m_y! m_z!} T_{AC}(\mathbf{m} + \bar{\mathbf{c}}) \langle \mathbf{a} + \mathbf{m} | \mathbf{b} \rangle &= \\
&- \sum_{m_x, m_y, m_z} \frac{(-1)^m}{m_x! m_y! m_z!} T_{AC}(\mathbf{m} + \mathbf{1}_x + \bar{\mathbf{c}}) \langle \mathbf{a} + \mathbf{m} | \mathbf{b} \rangle + \\
&2 \sum_{m_x, m_y, m_z} \frac{(-1)^m}{m_x! m_y! m_z!} T_{AC}(\mathbf{m} + \bar{\mathbf{c}}) \langle \mathbf{a} + \mathbf{m} + \mathbf{1}_x | \mathbf{b} \rangle_{(1)} - \\
N_x(\mathbf{a}) \sum_{m_x, m_y, m_z} \frac{(-1)^m}{m_x! m_y! m_z!} T_{AC}(\mathbf{m} + \bar{\mathbf{c}}) \langle \mathbf{a} + \mathbf{m} - \mathbf{1}_x | \mathbf{b} \rangle &- \\
\sum_{m_x, m_y, m_z} \frac{(-1)^m m_x}{m_x! m_y! m_z!} T_{AC}(\mathbf{m} + \bar{\mathbf{c}}) \langle \mathbf{a} + \mathbf{m} - \mathbf{1}_x | \mathbf{b} \rangle. &\quad (4.28)
\end{aligned}$$

The last term on the right-hand side in Eq. (4.28) is 0 for  $m_x = 0$ . Thus, the sum over  $m_x$  starts with  $m_x = 1$  instead of 0

$$\begin{aligned}
\sum_{m_x, m_y, m_z} \frac{(-1)^m m_x}{m_x! m_y! m_z!} T_{AC}(\mathbf{m} + \bar{\mathbf{c}}) \langle \mathbf{a} + \mathbf{m} - \mathbf{1}_x | \mathbf{b} \rangle &= \\
\sum_{m_x=1, m_y, m_z} \frac{(-1)^m m_x}{m_x! m_y! m_z!} T_{AC}(\mathbf{m} + \bar{\mathbf{c}}) \langle \mathbf{a} + \mathbf{m} - \mathbf{1}_x | \mathbf{b} \rangle. &\quad (4.29)
\end{aligned}$$

Re-indexing the lower sum limit for  $m_x$  to 0 then yields

$$\begin{aligned}
\sum_{m_x=1, m_y, m_z} \frac{(-1)^m m_x}{m_x! m_y! m_z!} T_{AC}(\mathbf{m} + \bar{\mathbf{c}}) \langle \mathbf{a} + \mathbf{m} - \mathbf{1}_x | \mathbf{b} \rangle &= \\
\sum_{m_x, m_y, m_z} \frac{(-1)^{m+1} (m_x + 1)}{(m_x + 1)! m_y! m_z!} T_{AC}(\mathbf{m} + \mathbf{1}_x + \bar{\mathbf{c}}) \langle \mathbf{a} + \mathbf{m} | \mathbf{b} \rangle &= \\
- \sum_{m_x, m_y, m_z} \frac{(-1)^m}{m_x! m_y! m_z!} T_{AC}(\mathbf{m} + \mathbf{1}_x + \bar{\mathbf{c}}) \langle \mathbf{a} + \mathbf{m} | \mathbf{b} \rangle. &\quad (4.30)
\end{aligned}$$

Inserting the result of Eq. (4.30) into Eq. (4.28), we find the following double asymptotic expansion for the ERI derivative with respect to the  $x$  coordinate of  $\vec{A}$

$$\begin{aligned} \frac{\partial}{\partial A_x} \langle \mathbf{ab} | \bar{\mathbf{c}} \rangle &\sim 2 \sum_{m_x, m_y, m_z} T_{AC}(\mathbf{m} + \bar{\mathbf{c}}) \langle (\mathbf{a} + \mathbf{1}_x) + \mathbf{m} | \mathbf{b} \rangle_{(1)} - \\ &N_x(\mathbf{a}) \sum_{m_x, m_y, m_z} T_{AC}(\mathbf{m} + \bar{\mathbf{c}}) \langle (\mathbf{a} - \mathbf{1}_x) + \mathbf{m} | \mathbf{b} \rangle. \end{aligned} \quad (4.31)$$

Of course this result is identical to the one obtained by applying the double asymptotic expansion directly to the ERI derivative expression (compare Eq. (3.58))

$$\begin{aligned} \frac{\partial}{\partial A_x} \langle \mathbf{ab} | \bar{\mathbf{c}} \rangle &= 2 \langle (\mathbf{a} + \mathbf{1}_x) \mathbf{b} | \bar{\mathbf{c}} \rangle_{(1)} + N_x(\mathbf{a}) \langle (\mathbf{a} - \mathbf{1}_x) \mathbf{b} | \bar{\mathbf{c}} \rangle \\ &= 2 \sum_{m_x, m_y, m_z} T_{AC}(\mathbf{m} + \bar{\mathbf{c}}) \langle (\mathbf{a} + \mathbf{1}_x) + \mathbf{m} | \mathbf{b} \rangle_{(1)} - \\ &N_x(\mathbf{a}) \sum_{m_x, m_y, m_z} T_{AC}(\mathbf{m} + \bar{\mathbf{c}}) \langle (\mathbf{a} - \mathbf{1}_x) + \mathbf{m} | \mathbf{b} \rangle. \end{aligned} \quad (4.32)$$

The derivatives with respect the other components of  $\vec{A}$  can be obtained straightforwardly. The derivative with respect to the  $x$  coordinate of the auxiliary function center  $\vec{C}$  of the double asymptotic expansion of the ERI, Eq. (4.5), takes the form

$$\begin{aligned} \frac{\partial}{\partial C_x} \sum_{m_x, m_y, m_z} \frac{(-1)^m}{m_x! m_y! m_z!} T_{AC}(\mathbf{m} + \bar{\mathbf{c}}) \langle \mathbf{a} + \mathbf{m} | \mathbf{b} \rangle &= \\ \sum_{m_x, m_y, m_z} \frac{(-1)^m}{m_x! m_y! m_z!} T_{AC}(\mathbf{m} + \mathbf{1}_x + \bar{\mathbf{c}}) \langle \mathbf{a} + \mathbf{m} | \mathbf{b} \rangle, \end{aligned} \quad (4.33)$$

which is again the same result as comes from the double asymptotic expansion directly to the derivative of the ERI with respect to the  $x$  coordinate of the auxiliary function center  $\vec{C}$

$$\begin{aligned} \frac{\partial}{\partial C_x} \langle \mathbf{ab} | \bar{\mathbf{c}} \rangle &= \langle \mathbf{ab} | \bar{\mathbf{c}} + \bar{\mathbf{1}}_x \rangle \\ &\sim \sum_{m_x, m_y, m_z} \frac{(-1)^m}{m_x! m_y! m_z!} T_{AC}(\mathbf{m} + \mathbf{1}_x + \bar{\mathbf{c}}) \langle \mathbf{a} + \mathbf{m} | \mathbf{b} \rangle. \end{aligned} \quad (4.34)$$

Equivalent derivations can be done for the other components of  $\vec{C}$ . From these results, it is now straightforward to obtain the derivatives of ERIs for the calculation of the energy gradients in the double asymptotic expansion. For the derivative with respect to the  $x$  coordinate of the orbital center  $\vec{A}$  we find

$$\begin{aligned} \frac{\partial}{\partial A_x} \langle \mathbf{ab} \parallel \sum x_{\bar{c}} \bar{c} \rangle &\sim 2 \sum_{m_x, m_y, m_z} \frac{(-1)^m}{m_x! m_y! m_z!} Q_A(\mathbf{m}) \langle \mathbf{a} + \mathbf{m} + \mathbf{1}_x | \mathbf{b} \rangle_{(1)} - \\ &N_x(\mathbf{a}) \sum_{m_x, m_y, m_z} \frac{(-1)^m}{m_x! m_y! m_z!} Q_A(\mathbf{m}) \langle \mathbf{a} + \mathbf{m} - \mathbf{1}_x | \mathbf{b} \rangle, \end{aligned} \quad (4.35)$$

whereas the derivative with respect to the  $x$  coordinate of the auxiliary function center  $\vec{C}$  is given by

$$\begin{aligned} \frac{\partial}{\partial C_x} \langle \mathbf{ab} \parallel \sum x_{\bar{c}} \bar{c} \rangle &\sim \sum_{m_x, m_y, m_z} \frac{(-1)^m}{m_x! m_y! m_z!} \sum_C^{far} \sum_{\bar{c} \in C} \left( \frac{\pi}{\zeta_{\bar{c}}} \right)^{\frac{3}{2}} x_{\bar{c}} T_{AC}(\mathbf{m} + \bar{\mathbf{c}} + \mathbf{1}_x) \langle \mathbf{a} + \mathbf{m} | \mathbf{b} \rangle \\ &= \sum_{m_x, m_y, m_z} -(m_x + 1) Q_A(\mathbf{m} + \mathbf{1}_x) \langle \mathbf{a} + \mathbf{m} | \mathbf{b} \rangle. \end{aligned} \quad (4.36)$$

The definition of  $Q_A(\mathbf{m})$  is given in Eq. (4.12). The derivative with respect to the third center, *i.e.* the second orbital center, is again obtained by the translational invariance relation [119]. In agreement with Eq. (3.79), the ERI gradients can be calculated independently for the near-field and far-field regions. This can be expressed as

$$g_{A_x}^{ERI} = g_{A_x}^{ERI, near} + g_{A_x}^{ERI, far}. \quad (4.37)$$

The double asymptotic expansion of the far-field contribution of ERI gradients is

$$\begin{aligned} g_{A_x}^{ERI} &\sim \sum_{m_x, m_y, m_z} Q_A(\mathbf{m}) \sum_{a, b} 2P_{ab} \langle (\mathbf{a} + \mathbf{1}_x) + \mathbf{m} | \mathbf{b} \rangle_{(1)} - \\ &N_x(\mathbf{a}) \sum_{m_x, m_y, m_z} Q_A(\mathbf{m}) \sum_{a, b} P_{ab} \langle (\mathbf{a} - \mathbf{1}_x) + \mathbf{m} | \mathbf{b} \rangle, \end{aligned} \quad (4.38)$$

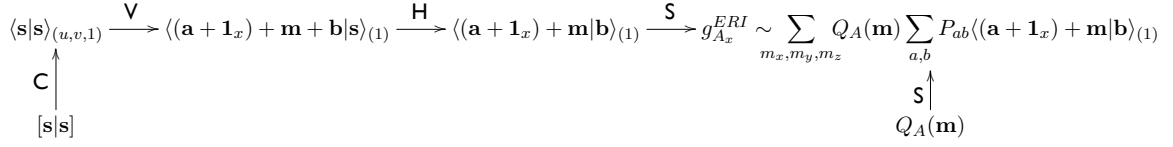


Figure 4.7: Pathway diagram for the calculation of the electron repulsion integral derivative up-shift term using the double asymptotic expansion.

and

$$\begin{aligned}
 g_{C_x}^{ERI} &\sim \sum_{m_x, m_y, m_z} -(m_x + 1) Q_A(\mathbf{m} + \mathbf{1}_x) \sum_{a,b} P_{ab} \langle \mathbf{a} + \mathbf{m} | \mathbf{b} \rangle \\
 &= \sum_{m_x, m_y, m_z} -(m_x + 1) Q_A(\mathbf{m} + \mathbf{1}_x) P(\mathbf{m}), \tag{4.39}
 \end{aligned}$$

where we have introduced

$$P(\mathbf{m}) = \sum_{a,b} P_{ab} \langle \mathbf{a} + \mathbf{m} | \mathbf{b} \rangle. \tag{4.40}$$

The pathway diagram for the calculation of the up-shift term of the ERI derivative with respect to the  $x$  coordinate of center  $A$  as given by the double asymptotic expansion is depicted in Figure 4.7. The first step is the calculation of the basic overlap integral as described in Eq. (3.5). The contraction step (C) is given by Eq. (3.47). The building of the angular momentum index at the orbital on the expansion center is performed in the vertical recurrence step (V) as shown in Eq. (3.7). Finally, the target modified overlap integral is obtained in the horizontal recurrence step (H), Eq. (3.8). Separately from the modified overlap integrals, the atomic quantity  $Q_A(\mathbf{m})$ , Eq. (4.12), is calculated. In the summation step (S) of the pathway diagram, the far-field form of the up-shift term of the ERI derivative with respect to the  $x$  coordinate of  $\vec{A}$ , Eq. (4.35), is built.

The pathway diagram for the calculation of the down-shift term of the ERI derivative with respect to the  $x$  coordinate of atom  $A$  as given by the double asymptotic expansion is depicted in Figure 4.8. The first step is the calculation of the basic overlap integral as described in Eq. (3.5). The contraction step (C) is given by Eq. (3.6). The



momentum index as seen from Eq. (4.36). The last step of the diagram is the summation (S) of the previously calculated quantities to obtain the target far-field ERI derivative with respect to the  $x$  coordinate of the auxiliary function center  $\vec{C}$ .

The pseudocode for the calculation of the far-field contribution to the ERIs gradient given by the double asymptotic expansion is depicted in Figure 4.10. In the first step in the algorithm, the  $Q_A(\mathbf{m} + \mathbf{1}_x)$  field is initialized. A far-field condition check is performed for atom  $A$  and  $C$ . If the condition is fulfilled, then the field  $Q_{AC}(\mathbf{m} + \mathbf{1}_x)$  is built. When the loop for atom  $B$  is accessed, a screening procedure for atom  $A$  and  $B$  is performed. If the overlap between  $A$  and  $B$  is significant, the work field  $Q_S(\mathbf{m} + \mathbf{1}_x)$  is initialized and a second far-field condition check is performed in order to ensure that the contributions to  $Q_S(\mathbf{m} + \mathbf{1}_x)$  are taken from all atoms  $C$  in the far-field of both atoms  $A$  and  $B$ . If not, contributions from atom  $C$  to  $Q_S(\mathbf{m} + \mathbf{1}_x)$  are subtracted. Again, this is done in order to avoid cubic scaling operations in the algorithm. Then, the three component  $(x, y, z)$  work fields *GRADA* and *GRADC* are initialized. In the shell loops, the scaled modified overlap integrals are built and the up-shift term of the orbital gradients is calculated; recall Eq. (4.38). If the angular momentum index of the orbital is greater than 0, the modified overlap integrals are calculated for the down-shift term of the ERI derivative, Eq. (4.38). Both terms are summed up in the work field *GRADA*. For the contribution to the gradients by the ERI derivative with respect to the auxiliary function center, the modified overlap integrals and the field  $P(\mathbf{m})$ , Eq. (4.40), are calculated. Outside of the shell loops, the gradient contributions from the auxiliary function derivatives are calculated, Eq. (4.39), summed up in the work field *GRADC* and subsequently added to the gradients field. Finally, in the diatomic loop, the gradient contributions from the orbital derivatives are calculated using the translational invariance relation, Eq. (3.61) and added to the global gradients field.

```

DO ATOM_A
  Initialize  $Q_A(\mathbf{m} + \mathbf{1}_x) = 0$ 
DO ATOM_C
  IF distance  $\overline{AC}$  is greater than  $r_a + r_\phi$  calculate
     $T_{AC}(\mathbf{m} + \mathbf{c} + \mathbf{1}_x)$  and  $Q_{AC}(\mathbf{m} + \mathbf{1}_x)$ ;
    add  $Q_A(\mathbf{m} + \mathbf{1}_x) \leftarrow Q_A(\mathbf{m} + \mathbf{1}_x) + Q_{AC}(\mathbf{m} + \mathbf{1}_x)$ 
END DO
DO ATOM_B
  IF distance  $\overline{AB}$  is greater than  $r_a + r_b$  go to next ATOM_B
  Initialize  $Q_S(\mathbf{m} + \mathbf{1}_x) = Q_A(\mathbf{m} + \mathbf{1}_x)$ 
DO ATOM_C
  IF distance  $\overline{AC}$  is greater than  $r_a + r_\phi$  but
    distance  $\overline{BC}$  is smaller than or equal  $r_b + r_\phi$  subtract
     $Q_S(\mathbf{m} + \mathbf{1}_x) \leftarrow Q_S(\mathbf{m} + \mathbf{1}_x) - Q_{AC}(\mathbf{m} + \mathbf{1}_x)$ 
END DO
  Initialize  $GRADA(x) = 0$ ,  $GRADC(x) = 0$ 
DO SHELL_A
  DO SHELL_B
    Read  $P_{ab}$ 
    Calculate  $\langle (\mathbf{a} + \mathbf{1}_x) + \mathbf{m} | \mathbf{b} \rangle_{(1)}$ 
    Calculate up-shift term of  $g_{A_x}^{ERI}$ 
     $GRADA(x) \leftarrow GRADA(x) + \text{up-shift term of } g_{A_x}^{ERI}$ 
    IF angular momentum index of SHELL_A > 0 THEN
      Calculate  $\langle (\mathbf{a} - \mathbf{1}_x) + \mathbf{m} | \mathbf{b} \rangle$ 
      Calculate down-shift term of  $g_{A_x}^{ERI}$ 
       $GRADA(x) \leftarrow GRADA(x) + \text{down-shift term of } g_{A_x}^{ERI}$ 
    END IF
    Calculate  $\langle \mathbf{a} + \mathbf{m} | \mathbf{b} \rangle$  and build  $P(\mathbf{m})$ 
  END DO
END DO
DO ATOM_C
  Calculate  $g_{C_x}^{ERI}$ 
   $GRADC(x) \leftarrow GRADC(x) + g_{C_x}^{ERI}$ 
  Add  $g_{C_x}^{ERI}$  to global gradients field
END DO
  Add  $GRADA(x)$  to global gradients field
  Calculate  $g_{B_x}^{ERI} = -GRADA(x) - GRADC(x)$ 
  Add  $g_{B_x}^{ERI}$  to global gradients field
END DO
END DO

```

Figure 4.10: Pseudocode for the calculation of the ERIs gradients using the double asymptotic expansion.

## 4.6 Asymptotic expansion of the embedding integral derivatives

The derivative of the asymptotic expansion of the embedding integral, Eq. (4.21), has the following form

$$\begin{aligned} \frac{\partial}{\partial A_x} \sum_{m_x, m_y, m_z} \frac{(-1)^m}{m_x! m_y! m_z!} T_{AD}(\mathbf{m}) \langle \mathbf{a} + \mathbf{m} | \mathbf{b} \rangle = \\ \sum_{m_x, m_y, m_z} \frac{(-1)^m}{m_x! m_y! m_z!} \left( \frac{\partial}{\partial A_x} T_{AD}(\mathbf{m}) \right) \langle \mathbf{a} + \mathbf{m} | \mathbf{b} \rangle + \\ \sum_{m_x, m_y, m_z} \frac{(-1)^m}{m_x! m_y! m_z!} T_{AD}(\mathbf{m}) \left( \frac{\partial \langle \mathbf{a} + \mathbf{m} | \mathbf{b} \rangle}{\partial A_x} \right). \end{aligned} \quad (4.41)$$

The derivative of  $T_{AD}(\mathbf{m})$ , Eq. (4.4), with respect to the  $x$  coordinate of center  $A$  is

$$\frac{\partial}{\partial A_x} T_{AD}(\mathbf{m}) = -\frac{\partial}{\partial D_x} T_{AD}(\mathbf{m}) = -T_{AD}(\mathbf{m} + \mathbf{1}_x). \quad (4.42)$$

Following the line of argument given in section 4.5 we find

$$\begin{aligned} \frac{\partial}{\partial A_x} \langle \mathbf{ab} | \hat{\mathcal{A}}_D(0) \rangle \sim 2 \sum_{m_x, m_y, m_z} T_{AD}(\mathbf{m}) \langle (\mathbf{a} + \mathbf{1}_x) + \mathbf{m} | \mathbf{b} \rangle_{(1)} - \\ N_x(\mathbf{a}) \sum_{m_x, m_y, m_z} T_{AD}(\mathbf{m}) \langle (\mathbf{a} - \mathbf{1}_x) + \mathbf{m} | \mathbf{b} \rangle. \end{aligned} \quad (4.43)$$

Again this result is identical to the one obtained by applying the asymptotic expansion to the embedding integral derivative expression (see the right-hand side of Eq. (4.20) as a reference)

$$\begin{aligned} \frac{\partial}{\partial A_x} \langle \mathbf{ab} | \hat{\mathcal{A}}_D(0) \rangle = 2 \langle (\mathbf{a} + \mathbf{1}_x) \mathbf{b} | \hat{\mathcal{A}}_D(0) \rangle_{(1)} + N_x(\mathbf{a}) \langle (\mathbf{a} - \mathbf{1}_x) \mathbf{b} | \hat{\mathcal{A}}_D(0) \rangle \\ \sim 2 \sum_{m_x, m_y, m_z} T_{AD}(\mathbf{m}) \langle (\mathbf{a} + \mathbf{1}_x) + \mathbf{m} | \mathbf{b} \rangle_{(1)} - \\ N_x(\mathbf{a}) \sum_{m_x, m_y, m_z} T_{AD}(\mathbf{m}) \langle (\mathbf{a} - \mathbf{1}_x) + \mathbf{m} | \mathbf{b} \rangle. \end{aligned} \quad (4.44)$$

The derivative with respect to the  $x$  coordinate of the point charge position  $\vec{D}$  is given within the asymptotic expansion as

$$\begin{aligned} \frac{\partial}{\partial D_x} \sum_{m_x, m_y, m_z} \frac{(-1)^m}{m_x! m_y! m_z!} T_{AD}(\mathbf{m}) \langle \mathbf{a} + \mathbf{m} | \mathbf{b} \rangle = \\ \sum_{m_x, m_y, m_z} \frac{(-1)^m}{m_x! m_y! m_z!} T_{AD}(\mathbf{m} + \mathbf{1}_x) \langle \mathbf{a} + \mathbf{m} | \mathbf{b} \rangle, \end{aligned} \quad (4.45)$$

which is the same result as comes from applying the asymptotic expansion to the derivative of the embedding integral with respect to the  $x$  coordinate of the point charge position  $\vec{D}$

$$\begin{aligned} \frac{\partial}{\partial D_x} \langle \mathbf{ab} | \hat{\mathcal{A}}_D(0) \rangle = \langle \mathbf{ab} | \hat{\mathcal{A}}_D(\vec{1}_x) \rangle \sim \\ \sum_{m_x, m_y, m_z} \frac{(-1)^m}{m_x! m_y! m_z!} T_{AD}(\mathbf{m} + \mathbf{1}_x) \langle \mathbf{a} + \mathbf{m} | \mathbf{b} \rangle. \end{aligned} \quad (4.46)$$

With these results we can write the asymptotic expansion of embedding charge gradients. For the derivative with respect to  $A_x$  we find

$$\begin{aligned} \frac{\partial}{\partial A_x} \left\langle \mathbf{ab} \left| \sum_D^{MM} \frac{q_D}{|\vec{r} - \vec{D}|} \right. \right\rangle \sim 2 \sum_{m_x, m_y, m_z} Q_A^{MM}(\mathbf{m}) \langle (\mathbf{a} + \mathbf{1}_x) + \mathbf{m} | \mathbf{b} \rangle_{(1)} - \\ N_x(\mathbf{a}) \sum_{m_x, m_y, m_z} Q_A^{MM}(\mathbf{m}) \langle (\mathbf{a} - \mathbf{1}_x) + \mathbf{m} | \mathbf{b} \rangle, \end{aligned} \quad (4.47)$$

where the up-shift modified scaled integral is given by Eq. (4.27). For the derivative with respect to the point charge center, the asymptotic expansion yields the following form

$$\frac{\partial}{\partial D_x} \left\langle \mathbf{ab} \left| \sum_D^{MM} \frac{q_D}{|\vec{r} - \vec{D}|} \right. \right\rangle \sim - \sum_{m_x, m_y, m_z} (m_x + 1) Q_A^{MM}(\mathbf{m} + \mathbf{1}_x) \langle \mathbf{a} + \mathbf{m} | \mathbf{b} \rangle, \quad (4.48)$$

where the definition of  $Q_A^{MM}(\mathbf{m})$  is given in Eq. (4.22). The derivative with respect to the third center, *i.e.* the second orbital center, is obtained by the translational invariance relation [119]. Similar to Eq. (4.37), the total gradient contributions can be calculated independently for the near-field and far-field regions. This can be expressed

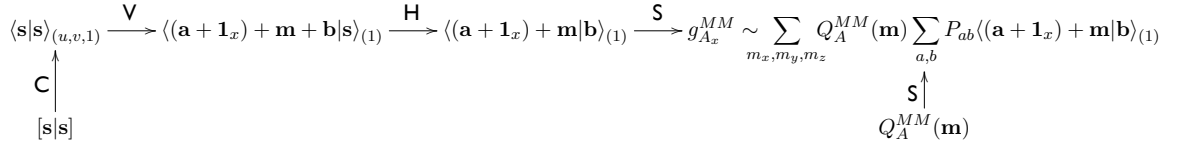


Figure 4.11: Pathway diagram for the calculation of the embedding integral derivative up-shift term using the asymptotic expansion.

as

$$g_{A_x}^{MM} = g_{A_x}^{MM, near} + g_{A_x}^{MM, far}, \quad (4.49)$$

The relevant far-field embedding gradient contributions can be calculated as

$$\begin{aligned} g_{A_x}^{MM} \sim & 2 \sum_{m_x, m_y, m_z} Q_A^{MM}(\mathbf{m}) \sum_{a,b} P_{ab} \langle (\mathbf{a} + \mathbf{1}_x) + \mathbf{m} | \mathbf{b} \rangle_{(1)} - \\ & N_x(\mathbf{a}) \sum_{m_x, m_y, m_z} Q_A^{MM}(\mathbf{m}) \sum_{a,b} P_{ab} \langle (\mathbf{a} - \mathbf{1}_x) + \mathbf{m} | \mathbf{b} \rangle, \end{aligned} \quad (4.50)$$

and

$$g_{D_x}^{MM} \sim - \sum_{m_x, m_y, m_z} (m_x + 1) Q_A^{MM}(\mathbf{m} + \mathbf{1}_x) \sum_{a,b} P_{ab} \langle \mathbf{a} + \mathbf{m} | \mathbf{b} \rangle. \quad (4.51)$$

The pathway diagram for the calculation of the up-shift term of the embedding integral derivative given by the asymptotic expansion is depicted in Figure 4.11. The first step is the calculation of the basic overlap integral as described in Eq. (3.5). The contraction step (C) is given by Eq. (3.47). The building of the angular momentum index of the orbital at the expansion center is performed by the vertical recurrence step (V), Eq. (3.7). Finally, the target modified overlap integral is obtained from the horizontal recurrence step (H), Eq. (3.8). Separately from the modified overlap integrals, the atomic quantity  $Q_A^{MM}(\mathbf{m})$ , Eq. (4.22), is calculated. In the summation step (S) of the pathway diagram, the far-field up-shift term of the embedding integral derivative with respect to the  $x$  coordinate of atom  $A$ , Eq. (4.47), is built.

The pathway diagram for the calculation of the down-shift term of the embedding integral derivative given by the asymptotic expansion is depicted in Figure 4.12. The



the calculation of the atomic quantity  $Q_A^{MM}(\mathbf{m})$  with an augmented-angular momentum index as shown in Eq. (4.48). The last step of the diagram is the summation (S) of the previously calculated quantities to obtain the target far-field embedding integral derivative with respect to the point charge center, Eq. (4.48)

The pseudocode for the calculation of the far-field contribution to the embedding integral gradients as given by the asymptotic expansion is depicted in Figure 4.14. In the first step of the algorithm, the  $Q_A(\mathbf{m} + \mathbf{1}_x)$  field is initialized. A far-field condition check is performed for atom  $A$  and point charge  $D$ . If the condition is fulfilled, then the field  $Q_{AD}^{MM}(\mathbf{m} + \mathbf{1})$  is built. When the loop for atom  $B$  is accessed, a screening procedure for atom  $A$  and  $B$  is performed. If the overlap between  $A$  and  $B$  is significant, the work field  $Q_S^{MM}(\mathbf{m} + \mathbf{1}_x)$  is initialized and a second far-field condition check is performed in order to ensure that the contributions to  $Q_S^{MM}(\mathbf{m} + \mathbf{1}_x)$  are taken from all point charges  $D$  in the far-field of both atoms,  $A$  and  $B$ . If not, contributions from point charge  $D$  to  $Q_S^{MM}(\mathbf{m} + \mathbf{1}_x)$  are subtracted. Thus, cubic scaling operations are avoided. Now, the three component  $(x, y, z)$  work fields *GRADA* and *GRADD* are initialized. In the shell loops, the scaled modified overlap integrals are built and the up-shift term of the orbital gradients is calculated, Eq. (4.50). If the angular momentum index of the orbital is greater than 0, the modified overlap integrals for the down-shift term of the embedding derivative and the down-shift term of the orbital gradient are built, too, Eq. (4.50). Both terms are summed together in the work field *GRADA*. For the contribution to the gradients with respect to the point charge center, the modified overlap integrals are calculated and the field  $P(\mathbf{m})$ , Eq. (4.40), is built. Outside of the shell loops, the gradient contribution from the point charge derivatives are calculated, Eq. (4.51). This is summed up in the work field *GRADD*. Finally, in the diatomic loop, the gradient contributions from the orbital derivatives are calculated using the translational invariance relation and added to the global gradients field.

```

DO ATOM_A
  Initialize  $Q_A^{MM}(\mathbf{m} + \mathbf{1}_x) = 0$ 
  DO POINT_D
    IF distance  $\overline{AC}$  is greater than  $r_a + r_\phi$  calculate
       $T_{AD}(\mathbf{m} + \mathbf{c} + \mathbf{1}_x)$  and  $Q_{AD}^{MM}(\mathbf{m} + \mathbf{1}_x)$ ;
      add  $Q_A^{MM}(\mathbf{m} + \mathbf{1}_x) \leftarrow Q_A^{MM}(\mathbf{m} + \mathbf{1}_x) + Q_{AD}^{MM}(\mathbf{m} + \mathbf{1}_x)$ 
  END DO
DO ATOM_B
  IF distance  $\overline{AB}$  is greater than  $r_a + r_b$  go to next ATOM_B
  Initialize  $Q_S^{MM}(\mathbf{m} + \mathbf{1}_x) = Q_A^{MM}(\mathbf{m} + \mathbf{1}_x)$ 
  DO POINT_D
    IF distance  $\overline{AD}$  is greater than  $r_a + r_d$  but
      distance  $\overline{BD}$  is smaller than or equal  $r_b + r_d$  subtract
       $Q_S^{MM}(\mathbf{m} + \mathbf{1}_x) \leftarrow Q_S^{MM}(\mathbf{m} + \mathbf{1}_x) - Q_{AD}^{MM}(\mathbf{m} + \mathbf{1}_x)$ 
  END DO
  Initialize  $GRADA(x) = 0$ ,  $GRADD(x) = 0$ 
  DO SHELL_A
    DO SHELL_B
      Read  $P_{ab}$ 
      Calculate  $\langle (\mathbf{a} + \mathbf{1}_x) + \mathbf{m} | \mathbf{b} \rangle_{(1)}$ 
      Calculate up-shift term of  $g_{A_x}^{MM}$ 
       $GRADA(x) \leftarrow GRADA(x) + \text{up-shift term of } g_{A_x}^{MM}$ 
      IF angular momentum index of SHELL_A > 0 THEN
        Calculate  $\langle (\mathbf{a} - \mathbf{1}_x) + \mathbf{m} | \mathbf{b} \rangle$ 
        Calculate down-shift term of  $g_{A_x}^{MM}$ 
         $GRADA(x) \leftarrow GRADA(x) + \text{down-shift term of } g_{A_x}^{MM}$ 
      END IF
      Calculate  $\langle \mathbf{a} + \mathbf{m} | \mathbf{b} \rangle$  and build  $P(\mathbf{m})$ 
    END DO
  END DO
  DO POINT_D
    Calculate  $g_{D_x}^{MM}$ 
     $GRADD(x) \leftarrow GRADD(x) + g_{D_x}^{MM}$ 
  END DO
  Add  $GRADA(x)$  to global gradients field
  Calculate  $g_{B_x}^{MM} = -GRADA(x) - GRADD(x)$ 
  Add  $g_{B_x}^{MM}$  to global gradients field
END DO
END DO

```

Figure 4.14: Pseudocode for the calculation of the embedding integral gradients using the asymptotic expansion.

# Chapter 5

## A new mixed SCF scheme

### 5.1 The SCF procedure

The molecular orbital (MO) coefficients and, consequently, the electronic density are obtained with a self-consistent field (SCF) procedure. This is a necessity since, as was explained in chapter 2, the calculation requires a density as input and the MO coefficients that build the density are the output.

Figure 5.1 shows a simplified flowchart for the conventional deMon2k SCF procedure. The actual SCF procedure in deMon2k is performed using a MinMax algorithm [95]. This is, however, out of the scope of our discussion here and, therefore, will not be explained further to avoid unnecessary complications. The SCF starts with the calculation of the electron repulsion integrals and the construction of the adaptive grid for the numerical integration (necessary for the exchange-correlation contribution calculation). In the next step the start density is prepared. Common procedures to obtain start densities are either tight-binding calculations [132] or the diagonalization of the core Hamiltonian matrix, Eq. (2.7). From the start density matrix, the first Coulomb vector  $\mathbf{J}$  is calculated. The Coulomb vector is used in the variational fitting of the Coulomb potential (VFCP) to obtain the charge fitting coefficients  $x_{\bar{e}}$  for the approximated density  $\tilde{\rho}(\vec{r})$  as described in section 2.2. With these coefficients it is possible to calculate the Kohn-Sham matrix. Diagonalizing the Kohn-Sham matrix yields a new set of MO coefficients [51,133] that defines a new density matrix  $\mathbf{P}$ .

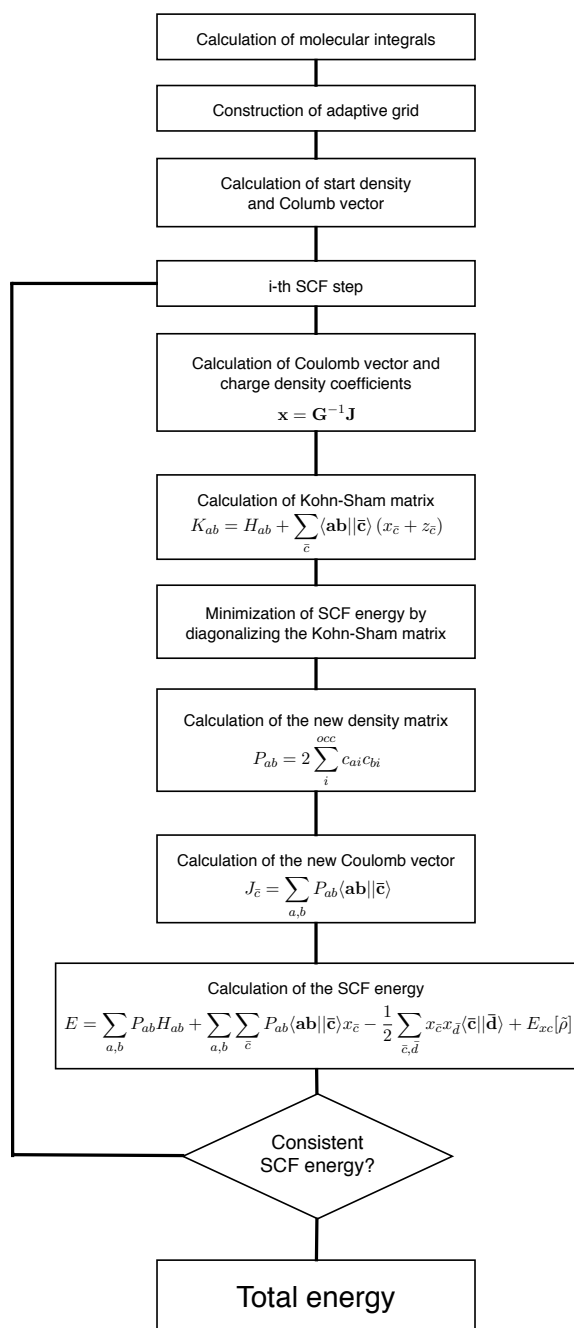


Figure 5.1: The general form of the self-consistent field procedure.

These MO coefficients are utilized to build a new Coulomb vector and fitting coefficients to calculate the electronic energy. If the energy is self-consistent within the

SCF threshold the procedure is terminated and the final total energy, including the nuclear repulsion contribution, is calculated. Otherwise, the next SCF cycle is started.

## 5.2 The SCF schemes

In the original deMon2k code the SCF procedure can be carried out in two ways although the algorithm is essentially the same in both cases. The main difference lies in the way the ERIs are calculated.

The first scheme available is the previously mentioned **conventional SCF** [134] in which the ERIs are calculated and stored before the actual SCF procedure starts. The advantage of this scheme is that ERIs are calculated only once for a given molecular geometry and are read from memory when needed. However, this scheme is only applicable for molecules up to around one hundred atoms with currently available computer architectures. This is due to the memory requirements for the ERIs. The user can choose if the ERIs will be stored only in RAM or if hard disk (HD) storage is allowed as well. This is important since using HD storage requires input/output (I/O) operations that can easily become a bottleneck in the calculation. Reading from HD and loading ERIs into the RAM is a time consuming task that will be done twice per SCF step due to the requirement of the ERIs for the calculation of both the Coulomb vector and Kohn-Sham matrix. Currently, this scheme is only available in serial calculations, *i.e.* for one-processor calculations.

The second scheme available is the **direct SCF** [113] in which the ERIs are calculated in the SCF procedure every time they are needed, *i.e.* one time for the calculation of the Coulomb vector and another time for the calculation of the Kohn-Sham matrix. The advantage of this scheme is that the memory requirements for the calculation of ERIs are minimal since they are calculated in small blocks (shell blocks). Such blocks require very little RAM and can be overwritten by the next ERI set. When the number of atoms is very large, *i.e.* the number of ERIs is huge, calculating the ERIs twice per SCF step requires considerably less time than the I/O operations necessary for the conventional SCF. In the direct SCF scheme the user can activate

the calculation of ERIs using the asymptotic expansion as discussed in section 3.8. The direct SCF scheme is available for one- and multi-processor calculations, and it is the only scheme available for multi-processor calculations.

### 5.3 The near-field ERIs bottleneck

In both SCF schemes, the calculation of ERIs is a demanding task. In chapter 4 a methodology for the calculation of the far-field ERIs in large systems using the double asymptotic expansion was presented. However, such expansion is only feasible when the integrals meet the requirements given in section 3.8. Thus, far-field ERIs appear in large numbers when the system is extended in space. In that case the double asymptotic expansion can reduce considerably the computational time for the far-field ERI calculation.

However, even when a system is extended in space it still possesses a large number of near-field ERIs that cannot be approximated by asymptotic expansions. For example, in deMon2k the direct SCF calculation of an insulin monomer ( $C_{256}H_{381}N_{65}O_{79}S_6$ ) using the DZVP basis set and the GEN-A2 auxiliary function set requires the calculation of 65,959,044,768 ERIs, 36,064,530,116 being near-field and 29,894,514,652 being far-field. This system can take advantage of the double asymptotic expansion implementation but the large number of near-field ERIs is still something to worry about. Another scenario is given by systems that are too large for the conventional SCF scheme but still not large enough to gain significant advantage from the double asymptotic expansion for far-field ERIs. This is particularly common in Born-Oppenheimer molecular dynamic simulations that explore the nanosecond time scale. In all these cases the direct SCF scheme currently is mandatory.

### 5.4 A new solution for the I/O bottleneck

Our new approach to circumvent the ERI I/O bottleneck is a combination of the conventional and direct SCF schemes. The double asymptotic expansion always take care of the far-field integrals employing the direct SCF scheme since the expansion

reduces the scaling and, consequently, the calculation time for the far-field integrals. The near-field ERIs are worked out in the frame of the conventional SCF scheme, *i.e.* the near-field ERIs are stored in memory. However, the only storage allowed is in RAM, since this will avoid the I/O operations that could become a bottleneck in the SCF procedure. Thus, as many as possible near-field integrals are calculated before the SCF procedure and stored in RAM. When the near-field integrals demand more RAM than available, the integrals that do not fit in memory are calculated using the direct SCF scheme. Due to the combination of both SCF schemes this new scheme is called **mixed SCF**.

The mixed SCF is not limited to one-processor calculations as the conventional SCF is. This is one of its most powerful features since the mixed SCF will use the available RAM for near-field ERIs storage from the whole computational architecture on which the calculation is performed. Each processor in the computational architecture will store as many near-field ERIs as its available RAM permits after the allocation of SCF matrices. In addition, the algorithm is programmed such that ERIs will be stored only in slave processors if enough RAM is available. In this way, the master processor RAM is not compromised in order to avoid memory saturation during other I/O operations on the master processor, *e.g.* reading and writing of the density and Kohn-Sham matrices.

Using the mixed SCF scheme eliminates the ERI bottleneck in many systems by calculating the time consuming near-field ERIs in a pre-SCF step and the numerous far-field ERIs with the efficient double asymptotic expansion in each step. A comparison of the three SCF schemes is shown in Figure 5.2.

<b>SCF SCHEME</b>	<b>ADVANTAGES</b>	<b>DISADVANTAGES</b>
Conventional	<ul style="list-style-type: none"><li>• ERIs are calculated only once per SCF procedure.</li><li>• ERIs are only read when needed (twice per SCF step).</li></ul>	<ul style="list-style-type: none"><li>• Rapid memory saturation in molecules with more than 100 atoms.</li><li>• Possible I/O bottleneck.</li><li>• No asymptotic expansion.</li></ul>
Direct	<ul style="list-style-type: none"><li>• Minimal memory requirement.</li><li>• Possibility to use asymptotic expansion.</li></ul>	<ul style="list-style-type: none"><li>• All ERIs are calculated twice per SCF step.</li></ul>
Mixed	<ul style="list-style-type: none"><li>• Stores high computational cost ERIs in RAM.</li><li>• No I/O bottleneck.</li><li>• Uses asymptotic expansion.</li></ul>	<ul style="list-style-type: none"><li>• Possible RAM saturation.</li></ul>

Figure 5.2: Comparison of the self-consistent field schemes available in deMon2k.

# Chapter 6

## Validation and performance of the code

This chapter provides comparisons of calculations for ERIs and embedding integrals as implemented in the original deMon2k code versus the double asymptotic expansion and mixed SCF scheme for ERIs and the asymptotic expansion for embedding integrals as implemented in the modified deMon2k code. The results are used to determine the consistency of the new implementation with respect to the original deMon2k code and the scaling of the new methodology. Additionally, example study cases are treated in order to show the possibilities opened by these new implementations.

### 6.1 Electron repulsion integrals

In order to analyze the accuracy and performance of the double asymptotic ERI expansion we have chosen our test system geometry such that one-, two- and three-dimensional packings are explored. The test systems for the ERIs benchmark comprise n-alkane chains as well as hydrogen-saturated graphene sheets and diamond blocks, all in singlet states. The geometrical parameters for the test systems are given in Table I. All calculations were performed within auxiliary density functional theory [44] as implemented in the deMon2k program [46]. The Coulomb energy was calculated by the variational fitting procedure proposed by Dunlap, Connolly and Sabin [42, 43,135]. For the fitting of the density, the auxiliary function set A2 [136] was used

Table I: Geometrical parameters for the test systems (distances in Å, angles and dihedrals in degrees).

System	Distance	Distance	Angle	Angle	Dihedral	Dihedral
	C-C	H-C	C-C-C	H-C-C	C-C-C-C	H-C-C-C
n-Alkane	1.50	1.00	109.47	109.47	109.47	109.47
Graphene	1.42	1.10	120.00	120.00	180.00	180.00
Diamond	1.54	1.10	109.47	109.47	60.00	60.00

in all calculations. All electrons were treated explicitly using a double-zeta valence-polarization (DZVP) basis [136]. The local density approximation (LDA) with the Dirac exchange [26] in combination with the correlation approximation for the ideal electron gas given by Vosko, Wilk and Nusair was used [64]. The exchange-correlation potential was numerically integrated on an adaptive grid [45] with an accuracy of  $10^{-5}$  Hartree a.u. in all calculations. The asymptotic expansion in the original deMon2k code and the double asymptotic expansion for the new code were utilized according to the distance criteria discussed in section 3.8 for the calculation of the Kohn-Sham matrix and Coulomb vector elements in each cycle of the direct SCF.

### 6.1.1 Direct SCF ERIs

The calculations for the direct SCF ERIs were carried out on 24 Intel Xeon X5675 processors (3.07 GHz). The number of ERIs and SCF cycles along with the absolute total energy differences between the original deMon2k and the new code are given in Table II, III and IV. In the case of one-dimensional n-alkane chains (see Figure 6.1 for the molecular structure) the number of far-field ERIs is always significantly larger than the number of near-field ERIs as Table II shows. With increasing system size, the number of far-field ERIs increases very rapidly. Also in the two-dimensional hydrogen-saturated rhomboidal graphene flakes (see Figure 6.2 for the molecular structure) the number of far-field ERIs is always larger than the number of near-field ERIs (see Table III). However, the differences between the number of near-field and far-field ERIs for these systems is much smaller than in the case of n-alkanes. For the three-dimensional hydrogen-saturated diamond blocks (see Figure 6.3 for the molecular structure) that we used as three-dimensional test systems the situation is reversed. Here the num-

Table II: Number of near- and far-field integrals, SCF cycles and absolute total energy differences [a.u.] between the original deMon2k and the new ERI implementation for the n-alkane test systems.

Number of carbons	Near-field integrals	Far-field integrals	Number of cycles	$\Delta E$
100	311,964,544	1,120,636,432	15	1.70E-8
110	345,587,724	1,391,795,872	16	1.70E-8
120	379,220,760	1,692,382,528	16	2.00E-8
130	412,843,940	2,022,280,648	16	2.10E-8
140	446,467,120	2,381,545,168	16	2.40E-8
150	480,090,300	2,770,176,088	16	2.50E-8
160	513,714,732	3,188,185,612	16	2.50E-8
170	547,337,912	3,635,550,172	16	2.90E-8
180	582,138,892	4,118,958,916	16	3.20E-8
190	616,607,704	4,631,005,052	16	3.40E-8
200	650,343,524	5,167,967,252	16	3.60E-8
210	691,046,712	5,781,016,100	16	3.90E-8
220	725,133,052	6,381,853,220	16	3.80E-8
230	759,219,392	7,012,392,740	16	4.30E-8
240	793,305,732	7,672,634,660	16	4.60E-8
250	827,960,608	8,367,306,476	16	4.30E-8
260	865,539,348	9,117,068,444	39	4.50E-8
270	899,788,088	9,869,339,084	39	5.10E-8
280	938,692,132	10,705,237,844	39	5.20E-8
290	983,995,540	11,635,447,472	40	5.90E-8
300	1,019,081,360	12,493,378,736	40	5.50E-8

ber of far-field ERIs is always smaller than the number of near-field ERIs. From the data in Table IV we find that the number of near-field ERIs increases quadratically whereas the number of far-field ERIs increases cubically. Extrapolating the data in Table IV indicates a crossover for systems with around 1,800 carbon atoms. Thus, the systems here studied are still far away from this crossover. Hence such systems are not considered here because computational memory limitations put them out of reach.

These benchmark calculations indicate that the double asymptotic ERI expansion has no influence on the SCF convergence, *i.e.* the number of SCF cycles is the same for both codes. Detailed comparison of the converged total energies between the orig-

Table III: Number of near- and far-field integrals, SCF cycles and absolute total energy differences [a.u.] between the original deMon2k and the new ERI implementation for the hydrogen-saturated graphene test systems.

Number of carbons	Near-field integrals	Far-field integrals	Number of cycles	$\Delta E$
338	12,014,006,804	13,658,144,896	98	4.50E-6
392	14,807,582,780	20,447,254,068	80	7.40E-6
450	18,055,988,252	29,665,067,368	79	1.13E-5
512	21,401,372,036	41,171,139,964	79	1.58E-5
578	25,099,850,900	55,705,776,432	79	2.18E-5
648	29,351,151,600	74,164,477,440	80	2.91E-5

Table IV: Number of near- and far-field integrals, SCF cycles and absolute total energy differences [a.u.] between the original deMon2k and the new ERI implementation for the hydrogen-saturated diamond test systems.

Number of carbons	Near-field integrals	Far-field integrals	Number of cycles	$\Delta E$
128	7,396,274,288	78,938,128	12	1.20E-8
250	35,935,555,540	1,967,937,360	14	1.86E-7
432	119,162,679,484	17,217,240,836	16	1.28E-6
686	301,843,042,800	89,183,694,700	18	3.90E-7

inal and new code shows energy differences in the range of  $10^{-6}$  Hartree a.u. or smaller for the n-alkanes and diamond-type test systems. This is well below the Min-Max SCF [95] converge criterion of  $10^{-5}$  Hartree a.u. (deMon2k default). In the case of the hydrogen-saturated graphene flakes energy differences up to  $3 \cdot 10^{-5}$  Hartree a.u. are found. The reason for these larger energy differences lies in the use of the level shift procedure [138] to enforce SCF convergence for these systems. This interpretation is confirmed by the enlarged number of SCF cycles (Table III) to reach energy convergence. Thus, we find that the double asymptotic ERI expansion yields identical results, within the SCF convergence criterion, as the original deMon2k code. This also holds for the cases where SCF convergence must be enforced, like for the graphene-type systems discussed here.

The computational timings for the ERI calculation per SCF cycle of the three kinds of test systems are shown in Figure 6.1, 6.2 and 6.3. The red bars in these figures correspond to the computational timings for both near- and far-field integrals in the original deMon2k code employing the asymptotic expansion. Since both types of integrals are calculated in the same step only one bar is depicted. The blue and green bars correspond to the computational timings for near- and far-field integrals in the new code. In this case, each integral type is calculated in a separate step. Thus, the timings can be distinguished and both bars together represent the full computational timing for the ERI calculation in the new code that can be directly compared to the original deMon2k timings. Since the near-field integrals were calculated in the same way in both implementations, it is reasonable to assume that the computational timings for these integrals are very similar in both codes. Therefore, horizontal lines between the bars representing the computational timings for ERIs from the asymptotic expansion in the original deMon2k and new codes have been drawn in order to have a common baseline for the comparison.

Even for systems with more far-field integrals than near-field integrals, the latter contribute by far the most from the total ERI timing. This is particularly well demonstrated in the case of the large n-alkanes. For the largest n-alkane,  $C_{300}H_{602}$ , the number of far-field ERIs is over ten times the number of near-field ERIs (see Table II) but the computational cost for these far-field ERIs employing the new double asymptotic expansion is one fifth of that for the near-field ERIs. The difference to the original deMon2k timings also indicates significantly improved computational performance of the new code. Because the near-field ERIs are calculated in both codes the same way, this improved performance is due to the new double asymptotic expansion of the far-field ERIs. As a consequence we find that the reduction of computational time is proportional to the number of far-field integrals and, thus, to the size of the system. This is consistent with the algorithmic features discussed for the double asymptotic expansion, since the (larger) number of auxiliary centers in the far-field region contributes only to the  $T_{AC}(\mathbf{m})$  term, Eq. (4.4), that is calculated outside the integration loops. In the case of the diamond-type test system (Figure 6.3), the time required for the calculation of far-field ERIs using the double asymptotic expansion

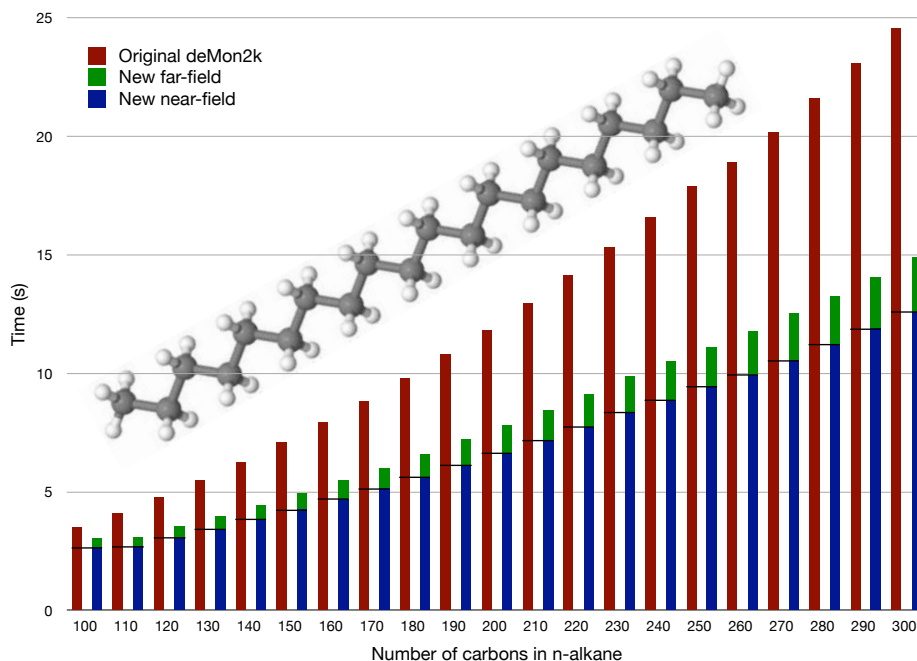


Figure 6.1: Computational timings for the ERI calculation per SCF cycle of n-alkane chains. The horizontal lines between bars show the predicted baseline for the far-field ERI timings in the original deMon2k code.

is practically negligible compared to the time spent in the near-field ERIs. Despite the relative small system size with respect to the ERI crossover point ( $\sim 1,800$  carbon atoms), a notable reduction in the computational timing for the ERI calculation is found for the largest diamond-type test system,  $C_{686}H_{294}$ .

In order to have a clearer idea of the benefits of the double asymptotic expansion, an additional benchmark was done with one-processor calculations. In the particular case of the n-alkanes, the original deMon2k implementation for the direct calculation and the asymptotic expansion of ERIs are compared with the double asymptotic expansion. These calculations were performed on a single Intel Xeon E5450 CPU (3.00 GHz). The computational timings per SCF cycle for the n-alkane ERI calculation are shown in Figure 6.4. The gray bars correspond to the computational timings for the direct ERIs in the original deMon2k code. The red bars correspond to the computational timings for both near- and far-field ERIs in the original deMon2k code

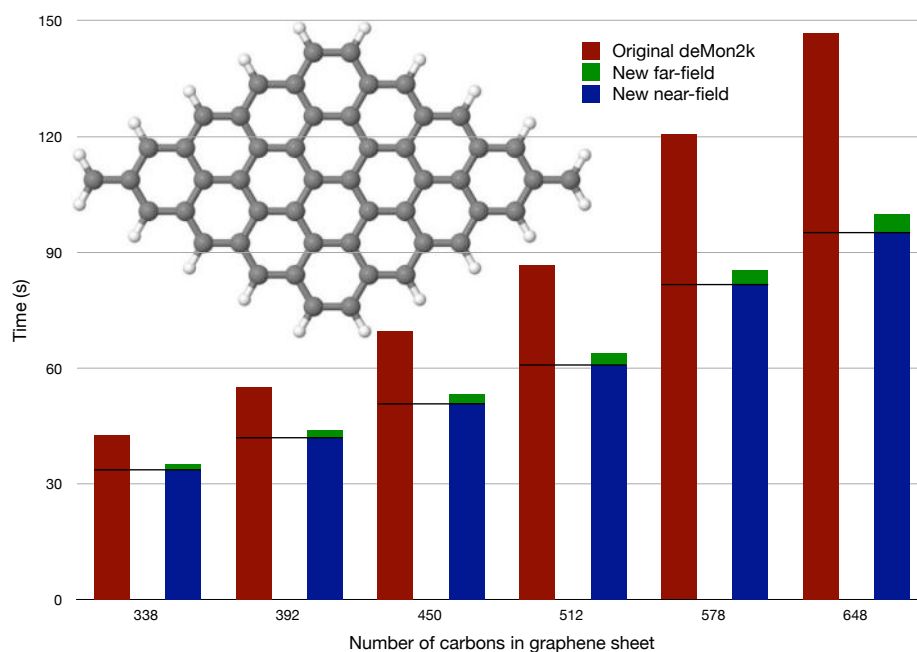


Figure 6.2: Computational timings for the ERI calculation per SCF cycle of hydrogen-saturated graphene sheets. The horizontal lines between bars show the predicted baseline for the far-field ERI timings in the original deMon2k code.

employing the asymptotic expansion. The blue and green bars correspond to the computational timings for near- and far-field integrals in the new code. Horizontal lines between the bars representing the computational timings for ERIs from the asymptotic expansion in the original deMon2k and new codes have been drawn in order to have a common baseline for the comparison.

The analysis of the scaling with respect to the number of basis functions for the far-field ERI calculation in the n-alkane chain set yields a scaling of 1.47. However, calculating the scaling only from the five largest n-alkane molecules yields a scaling of 0.90, *i.e.* sublinear with respect to the number of basis functions. The reason for the different scaling is found in the change of the most demanding computational steps in the ERI calculation as the system grows. When a system is relatively small, the most demanding step is the calculation of the modified overlap integrals (see Figure 4.2 as a reference for the Kohn-Sham matrix ERIs). This results in a quadratic scaling. When the system grows, the overlap integral screening starts to discard integrals and thus

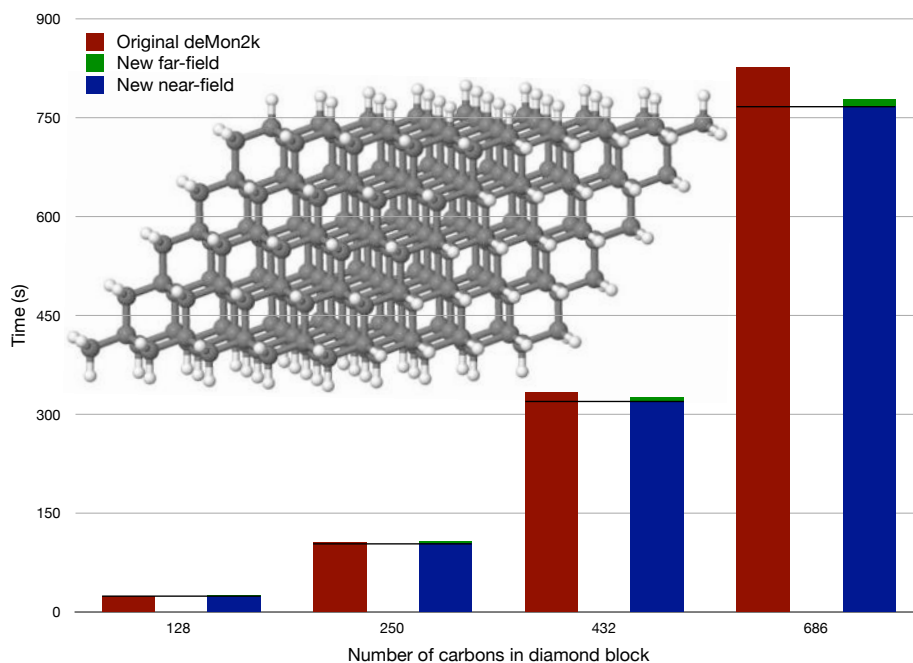


Figure 6.3: Computational timings for the ERI calculation per SCF cycle of hydrogen-saturated diamond blocks. The horizontal lines between bars show the predicted baseline for the far-field ERI timings in the original deMon2k code.

changes the scaling towards the linear regime. When the systems is large enough, the modified overlap integral timing becomes negligible compared to the calculation of the atomic derivatives given by  $T_{AC}$ , Eq. (4.4), the latter being the most demanding step of the calculation. When this happens, the scaling becomes quadratic, however, with respect to the number of atoms. As a result, the scaling with respect to the number of basis functions becomes sublinear for the system size studied here. This nicely demonstrates how the double asymptotic ERI expansion transforms the scaling of long-range ab-initio interactions into a regime typical for atomistic simulations with empirical atomic potentials. Most certainly, this opens a completely new avenue for ab-initio LCGTO-DFT calculations.

A scaling analysis was also performed for the graphene sheets and diamond blocks, yielding scalings of 1.46 and 1.75, respectively. These scalings are consistent with the number of far-field ERIS in these test system and confirm that for large numbers of

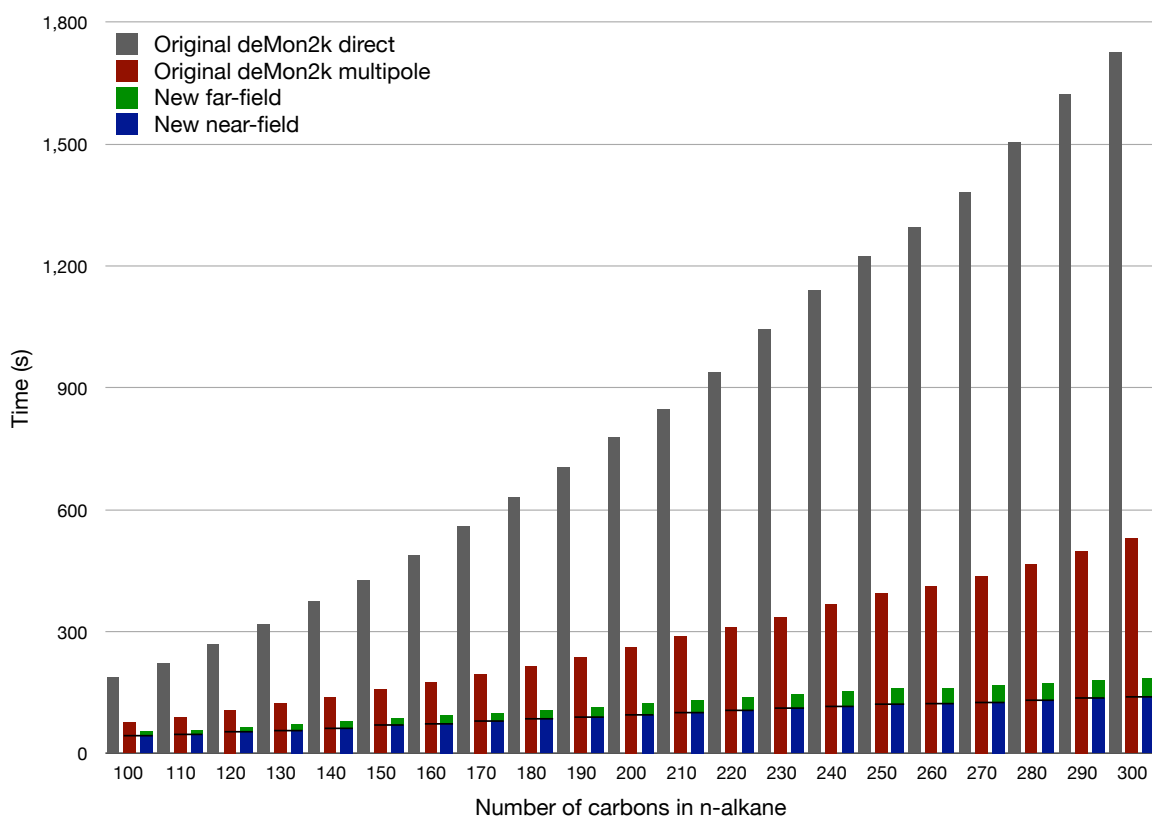


Figure 6.4: Computational timings for the ERI calculation per SCF cycle of n-alkane chains in one processor. The horizontal lines between bars show the predicted baseline for the far-field ERI timings in the original asymptotic expansion implementation in deMon2k.

far-field ERIs the linear scaling regime will be reached, independently of the system dimensionality.

## 6.1.2 ERI gradients

The performance and accuracy of the double asymptotic ERI gradient calculation was benchmarked with the partial optimization of the n-alkanes from section 6.1 as well as a full optimization of the first twenty n-alkanes of the group. The calculations were carried out using 8 Intel Xeon E5450 CPUs (3.00 GHz). In Table V the number of optimization cycles and the total energy for the fully optimized systems are presented. The number of optimization cycles is not affected by the use of the

Table V: Number of optimization cycles and absolute total energy differences [a.u.] of the converged geometries between the original deMon2k and the new ERI gradients implementation for the first twenty n-alkane chains in the test sets.

Number of carbons	Number of cycles	$\Delta E$
100	16	5.10E-8
110	16	1.00E-8
120	17	3.30E-8
130	17	1.00E-9
140	18	9.70E-8
150	18	7.70E-8
160	19	1.00E-9
170	19	1.94E-7
180	20	1.22E-7
190	21	7.80E-8

double asymptotic expansion in the ERI gradients since it is the same for both the original deMon2k and the new code. Also, the absolute total energy differences for the optimized geometries are in the range of  $10^{-7}$  Hartree a.u. which is very well in the accuracy range expected for default geometry optimizations in deMon2k.

The computational timings for the ERI gradients calculation per optimization cycle for the partial geometry optimization of n-alkanes from 100 to 300 carbon atoms is depicted in Figure 6.5. The red bars correspond to the computational timings for both near- and far-field ERI gradients in the original deMon2k code employing the asymptotic expansion. The blue and green bars correspond to the computational timings for near- and far-field integrals in the new code, respectively. Since the near-field ERI gradients were calculated in the same way in both implementations, horizontal lines between the bars represent a predicted near-field ERI gradients timing for the original deMon2k code. As expected, the larger the system the better the performance of the double asymptotic expansion of the ERI gradients with respect to the original deMon2k code. In the largest system,  $C_{300}H_{602}$ , the far-field ERI gradient calculation time per optimization cycle using the double asymptotic expansion is a quarter of the time required by the asymptotic expansion implemented in the original deMon2k code. The absolute difference in total energies between the original and new code is

also in the range of  $10^{-7}$  a.u. for the systems studied here.

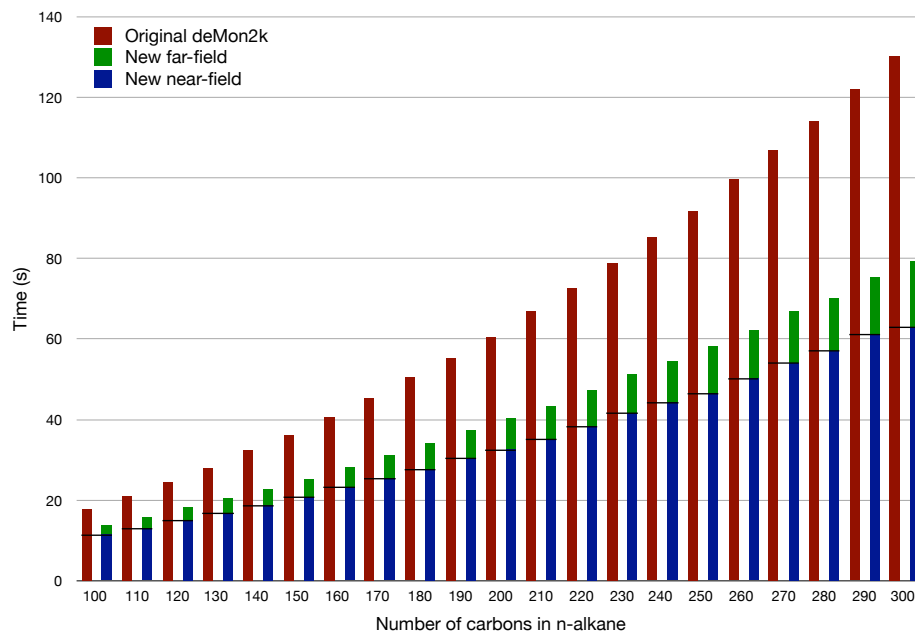


Figure 6.5: Computational timings for the ERI gradients calculation per optimization cycle of n-alkane chains with eight processors. The horizontal lines between bars show the predicted baseline for the far-field ERI timings in the original asymptotic expansion implementation in deMon2k.

## 6.2 Embedding integrals

Different systems have been used for benchmarking of the asymptotic expansion of the core embedding and embedding gradient integrals. The first model is taken from the nucleotidyl transfer reaction involving RNA polymerase II [146]. Here the QM subsystem is defined based on the analysis of the ligand and the protein, which results in a QM subsystem of 124 atoms with a charge of -2 and a singlet multiplicity. The rest of the system is defined as the MM subsystem. To study the long-range electrostatics, the size of the MM part is varied. The number of MM atoms in the benchmarking are 1,145, 2,479, 3,309, 4,527, 5,946, 6,851, 7,677, 8,573, 9,382, 10,614, 14034 and 59,259. Positions of the embedding charges and QM atoms are taken from a snapshot of a 1 ns long molecular dynamics trajectory of the RNA polymerase II

system [146]. The QM system is capped with hydrogen atoms at the boundary with the embedding charges.

The second benchmark system consists of a MgO cube formed by 51x51x51 unit cells in which the central cell is built from 8 QM atoms (4 Mg and 4 O) and the other cells are built from point charges. In total, this system contains more than one million point charges.

Except for the exchange-correlation functional, these calculations used the same procedures and basis as described at the start of section 6.1. The generalized gradient approximation, as proposed by Perdew, Burke and Ernzerhof [69], was applied. The exchange-correlation potential was numerically integrated on an adaptive grid [45]. The grid accuracy was set to  $10^{-5}$  a.u. in all calculations.

### 6.2.1 Core embedding integrals

The core embedding integrals were benchmarked using the RNA polymerase fragments. In Table VI the number of integrals for these systems is shown. The far-field integrals are separated into the *full sum* (with the asymptotic expansion up to 8<sup>th</sup> order) and *cut-off sum* (with the asymptotic expansion up to 2<sup>nd</sup> order) integrals as explained in chapter 4. Even for the second smallest test system, with 2,479 embedding charges, the near-field integrals are already saturated as the comparison with the following test systems shows. Thus, from that system on, only the number of far-field integrals increases. That number grows rapidly, as Table VI shows. From 5,946 embedding charges onward, some far-field integrals are evaluated with the cut-off sum, *i.e.* with asymptotic expansion sums only up to 2<sup>nd</sup> order. The number of these integrals increases moderately until the system with 59,259 embedding charges. In that system the number of far-field integrals with expansions up to the 8<sup>th</sup> and 2<sup>nd</sup> order are practically the same.

In Figure 6.6 computational timings for the embedding integral calculation in the studied QM/MM systems are shown. The red bars correspond to the direct embedding integral sum timings of the original deMon2k code. Since this part of the code

Table VI: Number of near- and far-field integrals (full sum and cut-off sum) and absolute total energy differences [a.u.] between the original deMon2k and the new implementation for the embedded RNA polymerase II fragment.

Number of charges	Near-field integrals	Far-field integrals (full sum)	Far-field integrals (cut-off sum)	$\Delta E$ (serial)	$\Delta E$ (parallel)
1,145	63,766,082	340,788,753	0	7.00E-09	6.00E-09
2,479	67,686,417	808,201,300	0	0.00E-00	0.00E-00
3,309	67,762,848	1,101,382,959	0	2.00E-09	2.00E-09
4,527	67,762,848	1,531,730,373	0	0.00E-00	1.00E-09
5,946	67,762,848	2,033,093,450	2,260	2.00E-09	2.00E-09
6,851	67,762,848	2,352,777,039	75,986	5.20E-08	5.20E-08
7,677	67,762,848	2,644,578,206	119,617	5.20E-08	5.20E-08
8,573	67,762,848	2,960,792,766	482,465	1.16E-07	1.16E-07
9,382	67,762,848	3,245,326,149	1,787,389	3.28E-07	3.28E-07
10,614	67,762,848	3,676,953,910	5,453,564	7.60E-08	7.50E-08
14,034	67,762,848	4,837,018,040	53,754,094	6.70E-08	6.80E-08
59,259	67,762,848	10,498,227,669	10,371,577,140	7.92E-07	7.93E-07

was not parallelized nor separated into near- and far-field contributions, only one bar represents the time for the whole integral sum calculation. The dark blue and dark green bars represent computational timings using one processor for the calculation of the near-field and far-field embedding integral sum with the new algorithm, respectively. Since these calculations are now separated into two different steps, timings for each step are given. Both bars together represent now the full timing for the embedding integral calculation and thus can be compared directly to the original deMon2k timings. Since the near-field embedding integrals were calculated with the same algorithm, they can be considered equal in timing. Thus, a horizontal line from the top of the blue bar to the red bar indicate the prediction of the timing for the near-field integrals achieved by the original deMon2k code. Finally, the light blue and light green bars depict the computational timings for the calculation of the near-field and far-field embedding integrals calculated with 8 processors.

The results for the new algorithm in Figure 6.6 show a considerable reduction in the time for the integral sum calculations even for the smallest test system. This is due to the improved computational performance of the asymptotic integral expansion. As

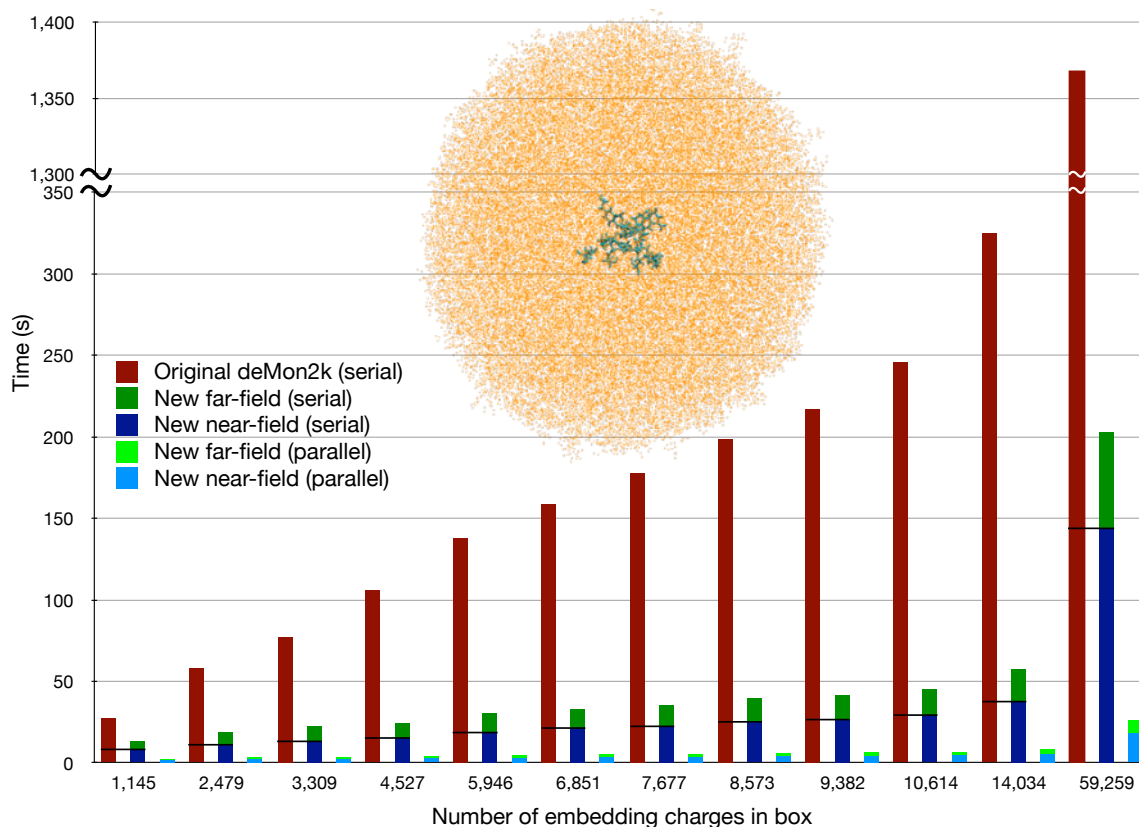


Figure 6.6: Comparison of computational timings for the embedding integral calculation in small QM/MM systems.

expected, the computational savings increase rapidly with the system size because of the rapid saturation of the number of near-field integrals (see Table VI). Comparison of the serial and parallel implementations of the asymptotic integral sum calculation indicates almost perfect scaling with respect to the number of processors. For the largest system (with 59,259 embedding charges) we find a computational speed-up relative to the original embedding sum implementation in deMon2k by a factor of around 6.7 for serial runs and a factor of more than 50 for the 8-processor parallel run in the total embedding integral calculation. The 26 s for the embedding integral calculation in the parallel run is negligible compared to the total QM/MM step time that is in the range of 2,000 s. Thus, the asymptotic integral expansion removes the embedding integral bottleneck in large-scale QM/MM calculations without jeopardiz-

ing the accuracy of the QM methodology. To analyze this in more detail, Table VI also lists the total energies calculated with the original direct embedding integral sum and the new near- and far-field separations for all embedded systems we studied. Table VI shows that the new serial and parallel code employing the asymptotic expansion of the embedding integral sum reproduces the original embedding sum energies within the default  $10^{-6}$  a.u. accuracy.

## 6.2.2 Embedding integral gradients

A cubic MgO system was used to benchmark the performance and accuracy of the embedding integral gradient calculation. The  $51 \times 51 \times 51$  unit cell system consists of only 8 QM atoms and 1,061,200 point charges representing Mg and O atoms. This yields 5,790,320 near-field embedding integrals and 9,670,231,280 far-field embedding integrals with 1,408,694,138 calculated via an expansion order up to 8 and 8,261,537,142 calculated with an expansion order up to 2, *i.e.* they are outside the cut-off radius. The benchmark results here presented are taken from 28 optimization steps.

The timings for the embedding integral gradients are plotted in Figure 6.7. The reduction in the embedding integral gradient timing can be considered exclusively a consequence of the use of the asymptotic expansion in the new code for the far-field integrals. The speed-up has a factor of around 1.50. This small speed-up factor arises

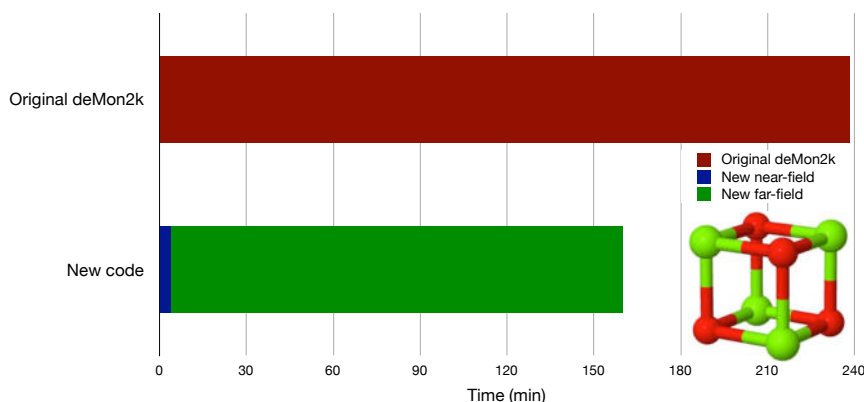


Figure 6.7: Total timings for embedding integral gradients (28 steps) calculation for the MgO cube system.

from the overhead created by the distance criterion explained in section 3.8 in chapter 3. Since this criterion is used to classify the point charges as elements of the near-field and far-field region of a given atom, an enormous number of point charges has to be inspected in this system causing a significant overhead from those distance calculations. A similar situation, even though much less pronounced, can be seen for the benchmark of the embedding integrals for the core Hamiltonian matrix (see Figure 6.6). As Table VI shows, the largest system in that benchmark has the same number of near-field embedding integrals as the smaller fragments but the calculation of those integrals takes up substantially more time for the largest system. A more detailed profiling again reveals that this overhead arises from distance calculations very much the same as in the MgO system discussed here. These findings suggest the need for a different algorithm to assign atomic centers to the near- and far-field region of a given atom pair for very large systems. However, that task is outside the scope of this thesis.

### 6.3 The mixed SCF scheme

The mixed SCF was benchmarked with the n-alkane chains from section 6.1 employing the same computational methodology as described there. We report timings for all ERIs in a single-point SCF calculation since it is important to demonstrate the benefit of computing the near-field ERIs only once during the single-point SCF. In addition to the original deMon2k timings using the single asymptotic expansion, the timings for the new direct SCF implementation using the double asymptotic expansion are also shown for comparison. The calculations were carried out using 32 Intel Xeon E7-8837 CPUs (2.67GHz). Together, the amount of RAM of these cores was sufficient to store all near-field ERIs.

The computational timings for the ERI calculations are shown in Figure 6.8. The timing for the original deMon2k implementation using the asymptotic expansion of far-field ERIs is depicted with red bars. The dark blue bars denote the computational time for the near-field ERIs and the dark green bars for the far-field ERIs calculated with the double asymptotic expansion. The third bar depicts the computational time

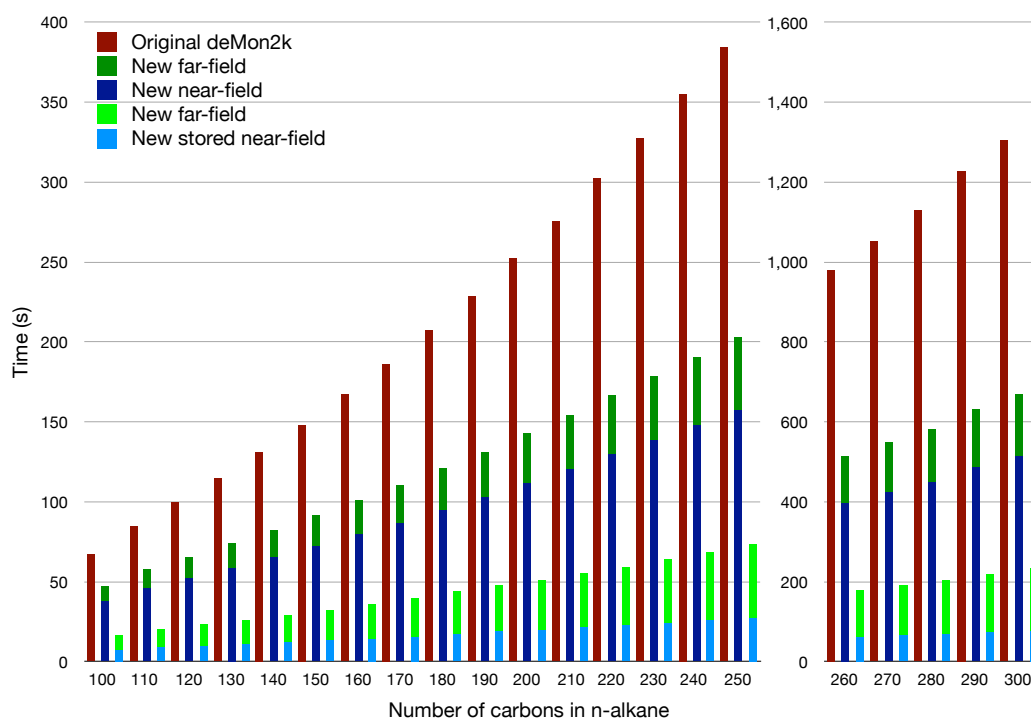


Figure 6.8: Computational timings for the ERI calculation in the single-point SCF of n-alkane chains. The scale is changed for the last few systems since the number of SCF cycles is larger.

for the mixed SCF scheme ERIs. It is divided into a blue bar for the in-core near-field ERI timings and a light green bar that denotes the timing for the direct far-field ERIs calculated with the double asymptotic expansion. The time saving due to the in-core calculation of the near-field ERIs is noteworthy as it can be seen in Figure 6.8. For the largest system,  $C_{300}H_{602}$ , the mixed SCF scheme shows a speed-up factor with respect to the original deMon2k code of above 6.5 for the calculation of near-field ERIs and 3.2 for the whole ERI timing. Another interesting fact seen in this benchmark is the growth trend of the near-field ERI timing. Even though the far-field ERI calculation goes into a linear regime as the system becomes larger, the growth trend for the in-core near-field ERIs is evidently lower than the far-field ERIs growth. This ultimately will drive the whole ERI calculation scaling into a sublinear regime for the here presented systems. Finally, as with the previous benchmarks, excellent agreement in the

total energies was found between the original deMon2k and the new implementation.

## 6.4 Perspectives

A common drawback for large-scale studies in chemistry and physics is the long time needed for the completion of the calculations such studies require. The implementations achieved in this thesis open the avenue for this kind of studies in reasonable times using the density functional theory program deMon2k. This will benefit research areas such as biochemistry [139–141], material science [142–144] and electrochemistry [145].

The implementations fruit of the labor presented here are already being utilized in collaboration with other research groups. Colleagues working on biochemistry study the system shown in section 6.4.1 [146]. Another group studies the system shown in section 6.4.2 [147]. A further study in our group is the geometry optimization of the insulin monomer shown in section 6.4.3.

### 6.4.1 RNA polymerase II in water

The entire RNA polymerase II system studied in Ref. [146] and introduced in section 6.2 contains 343,300 atoms since it also includes solvent molecules. The motivation for choosing this system is to model the biophysical and biochemical steps of the transcription process by messenger RNA using the nucleotide sequence of a template strand of DNA performed by the enzyme RNA polymerase. This system consists of 124 atoms representing the QM region and 343,176 MM atoms that represent the rest of the system. Figure 6.9 shows the QM/MM system. On the left, the ribbon model of the whole RNA polymerase II with the QM part in blue and the MM part in orange is depicted. On the right, the point charge model with the 343,176 embedding charges is shown. As in the benchmarking, the QM system is capped with hydrogen atoms.

The calculation reports 67,762,848 near-field embedding integrals as well as a total of 121,187,744,230 far-field embedding integrals, where 10,498,321,422 are calculated with the full sum and 110,689,422,808 are calculated using the cut-off sum. The timing for the original deMon2k (serial) implementation is 7,927.61 s. The new code using

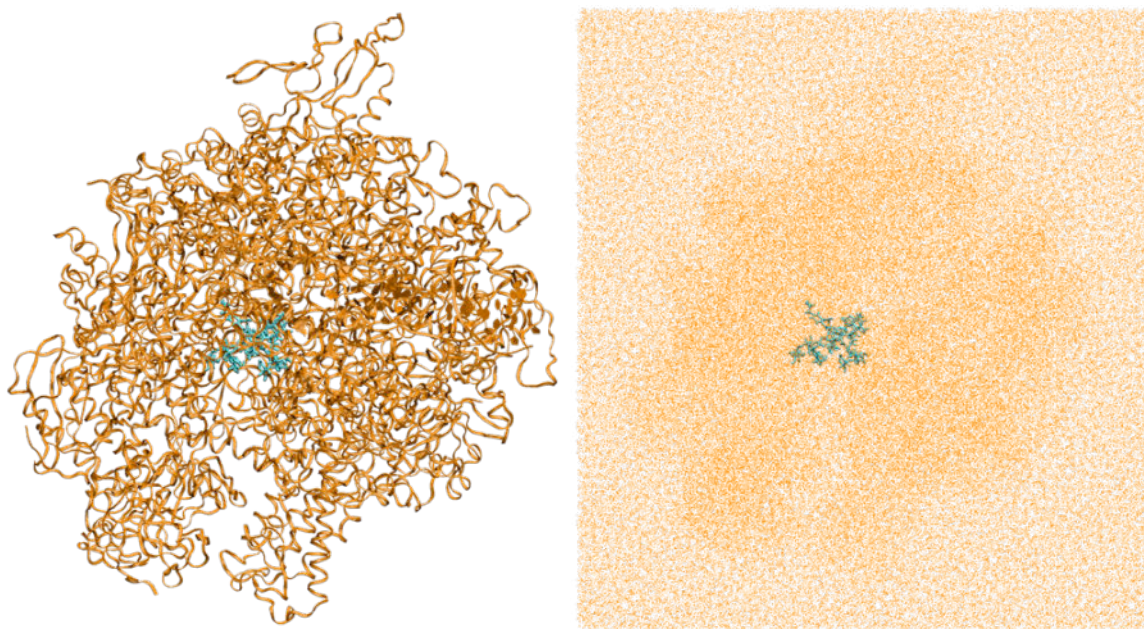


Figure 6.9: The ribbon model for RNA polymerase II (left) and the embedding system for the QM/MM calculation with 124 QM atoms and 343,176 MM atoms (right).

one processor yields timings of 817.55 s and 218.47 s for near- and far-field embedding integrals, respectively, whereas the parallel implementation using 8 processors yields 129.77 s and 37.98 s for the near- and far-field integrals, respectively. Thus, we found a computational speed-up relative to the original embedding integral implementation in deMon2k by a factor above 7 for serial runs and a factor of more than 45 for the parallel run. The 200 s for the embedding integral calculation represents only a fraction of the total QM/MM step time that is in the range of 6,000 s.

Comparing the number of integrals in this calculation with the number of integrals reported in Table VI shows that the far-field region presents a saturation of full sum integrals, whereas the number of cut-off integrals increases by one order of magnitude. This shows that a further increase of the embedding box will add only cut-off sum integrals which will be computationally less demanding than the full sum integrals. Considering this, a second cut-off radius could be introduced beyond which only zero-th order (charge) contributions are considered. This shows that our asymptotic integral expansion ultimately turns into a point charge picture as used in most MM

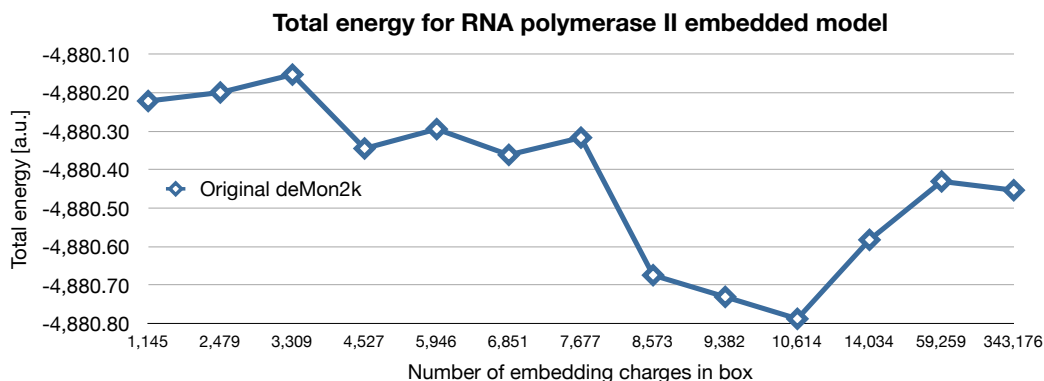


Figure 6.10: Total energy of the RNA polymerase II embedded model for different numbers of point charges.

approaches. As a consequence, every acceleration method for point charge interactions, e.g. fast multipole methods, can be used in combination with the asymptotic integral expansion presented here without loss of accuracy. This will be relevant for systems with millions of MM atoms, as was shown in section 6.2.2.

The benchmark result shows that the total energy differences between the original and new code are below  $10^{-6}$  a.u. for all systems. Thus, the use of the asymptotic expansion in the far-field embedding integrals has no effect on the total energy calculation. The total energy values for the benchmark calculations from section 6.2.1 and this calculation are given in Figure 6.10. As can be seen from this figure, substantial energy changes are found for systems with 10,614, 14,034 and 59,259 embedding charges. This fact underscores, once again, the importance of the accurate treatment of long-range Coulomb interactions in large-scale QM and QM/MM studies and calls for the incorporation of realistic electrostatic environments for such studies.

### 6.4.2 Molecular dynamics of the $\text{Na}_{55}^+$ cluster

Studies on physical and chemical properties of finite systems have become an active research area due to the development of nanoscience and nanotechnology. Calculation of cluster properties poses both experimental and theoretical challenges due to the size dependence they can exhibit [148]. When the cluster size is in the order of

dozens of atoms, it is important to use accurate theoretical methods to predict correctly the forces and internal energy in the system. For this purpose, first-principle Born-Oppenheimer molecular dynamics (BOMD) simulations are best suited.

The purpose of this calculation is to show the time reduction achieved by the mixed SCF scheme in BOMD simulations for a cationic sodium cluster consisting of 55 atoms. The calculations were carried out in parallel on Intel Xeon E5649 CPUs (2.53 GHz). The BOMD simulations were performed in the canonical ensemble at 150 K employing a Nosé-Hoover chain thermostat [149–151] using seven thermostats with a coupling frequency of  $1500 \text{ cm}^{-1}$ . The total simulation time was 400 fs with a step size of 2 fs. Technical details were as before, including use of the PBE exchange-correlation functional, except for the fact that the default SCF convergence acceleration by the direct inversion in the iterative subspace (DIIS) was disabled for this calculation to avoid possible SCF convergence problems. A level shift [138] of 0.5 Hartree a.u. was set. This setup is typical for BOMD production runs that target the finite system heat capacity as a function of temperature. For this purpose several thousands of these runs have to be performed and analyzed together to obtain robust statistics. Thus, even small savings are of great significance.

The  $\text{Na}_{55}^+$  cluster has, on average, 1,375,222,790 integrals during the BOMD simulation, all of them near-field. The timings for the ERI and total calculation are given in Figure 6.11 and 6.12, respectively. The number of processors for the calculation ranges from 24 to 120. Both figures show the expected decay of the computational timings into a plateau [152]. As it can be seen in Figure 6.11, the time reduction in the ERI calculation due to the mixed SCF scheme is around 90% independent of the number of processors used. For the overall saving the proportion between the ERI calculation and the total time is worth noticing. In the original deMon2k code, this proportion ranges from 59% on 24 processors to 46% on 120 processors. Thus, around half of the computational time for the BOMD simulations of the  $\text{Na}_{55}^+$  cluster is needed for ERI calculations. Using the mixed SCF scheme these proportions decrease to 17% on 24 processors and 7% on 120 processors indicating substantial savings in the total time, too.

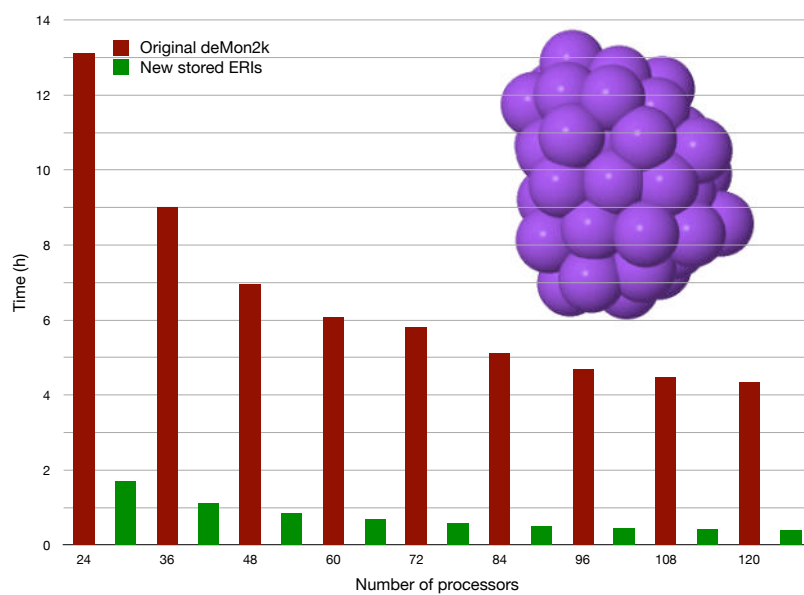


Figure 6.11: ERI timings for Na<sub>55</sub><sup>+</sup> BOMD simulations with different numbers of processors.

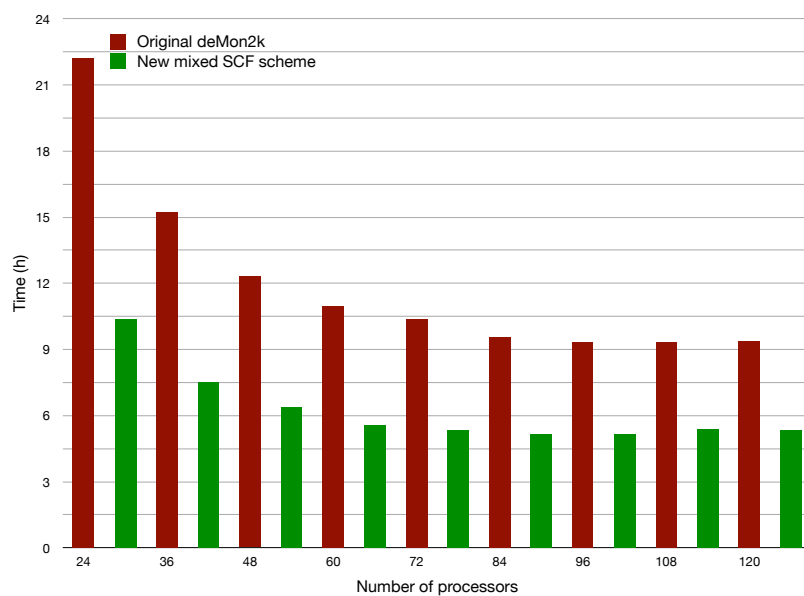


Figure 6.12: Total timings for Na<sub>55</sub><sup>+</sup> BOMD simulations with different numbers of processors.

To analyze this in more detail we depict in Figure 6.12 the total timings for the  $\text{Na}_{55}^+$  BOMD simulations on various numbers of processors. As this figure shows, our new mixed SCF scheme reduces the total timings roughly by half. Knowing that only the ERI calculation is different between the original and new code this result shows the importance of saving time in the ERI computation in BOMD simulations. Although this particular BOMD is not long enough to calculate thermodynamic properties like heat capacities, it is worth while to extrapolate the amount of time required to obtain such data. It is expected that one hundred thousands steps for one temperature will provide enough data to obtain a stable statistical sampling, *e.g.* with the multiple histogram method [153,154], from which the heat capacity of the  $\text{Na}_{55}^+$  cluster then can be calculated. If this dynamics was meant to be done with the original deMon2k code it would require almost fifteen and a half months using 24 processors or six and a half months using 120 processors. The use of the mixed SCF scheme will reduce these timings to around half and, therefore, allows the calculation of thermodynamic properties of systems with up to around 100 atoms using first-principle all-electron BOMD simulations.

### 6.4.3 Geometry optimization of the insulin monomer

The study of human insulin is of great interest in biochemistry. Although insulin mainly exists in our body in associated states (from dimer to hexamer), the monomer is the biologically active form. Thus, knowledge of the structure and properties of the insulin monomer (Figure 6.13) is mandatory in order to understand its trend to form dimers, behavior which has been associated with drawbacks in the preparation and stability of formulations [155].

This calculation reports on the geometry optimization of the insulin monomer using the mixed SCF scheme. The molecule consists of 784 atoms. The computational architecture used for the calculation consists of 64 Intel Xeon E7-8837 CPUs (2.67GHZ) with enough memory to store all near-field ERIs in RAM. Technical details are as before, with the local density approximation used for exchange and correlation.

The computational methodology results in 7,974 orbitals and 15,292 auxiliary func-

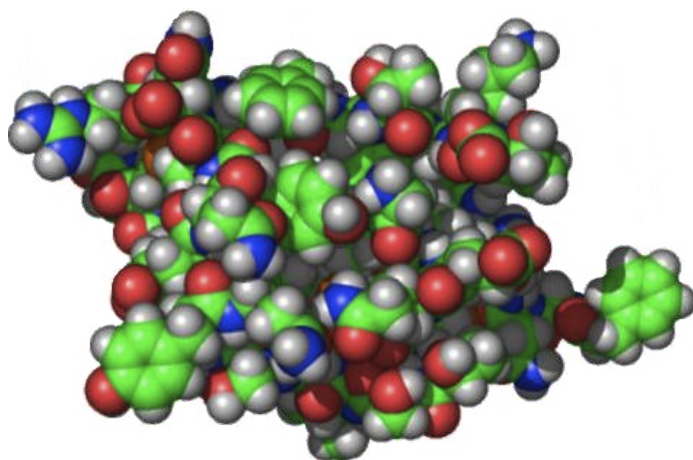


Figure 6.13: The insulin monomer model used for geometry optimization.

tions for the calculation. This calculation required several submissions to the computation system due to its configured walltime. Thus, the accumulated times for all the submissions are shown in the discussion. During the geometry optimization we find, on average, 37,864,719,360 near-field ERIs and 30,143,796,706 far-field ERIs. The calculation times for the SCF ERIs and ERI gradients are given in Figure 6.14. The depicted timings refer to 6,166 SCF cycles and 108 optimization cycles. From Figure 6.14 two important facts for this particular calculation can be deduced. First, the near-field ERIs calculated with the mixed SCF scheme and the far-field ERIs using the double asymptotic expansion have very similar timings since they are practically the same in number. This demonstrates the efficiency of the double asymptotic expansion for the far-field ERI calculation in large-scale all-electron calculations since it is comparable to an in-core ERI algorithm. Second, the ratio of the timings for the near-field and far-field ERI gradients is around 20. Assuming a similar ratio for the near- and far-field SCF ERIs in the direct SCF scheme, the time required for the calculation of the near-field ERIs would reach the order of weeks. This highlights the benefits of the in-core calculation given by the mixed SCF scheme.

The total calculation time for this test was 15 days. The SCF ERIs needed 11% of this time whereas the ERI gradient timing accounted only for 1%. Thus, it is fair to say that the ERI bottleneck has been removed for large-scale deMon2k calculations.

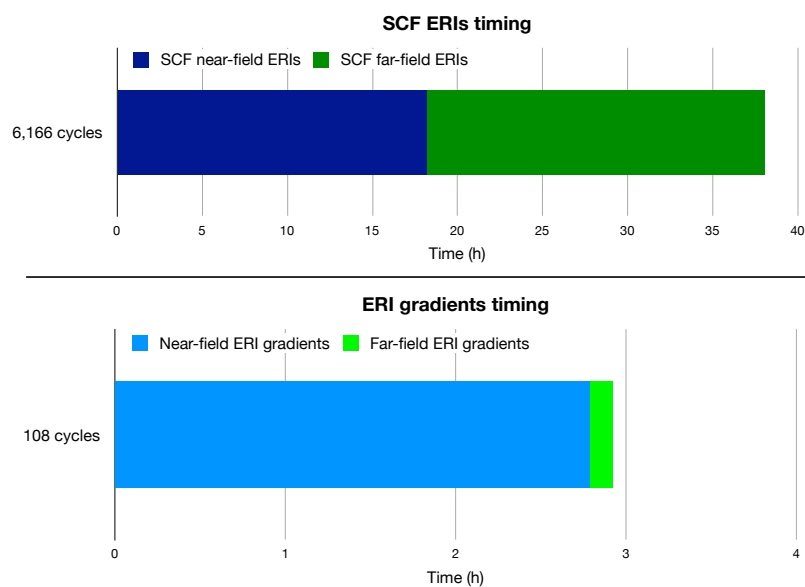


Figure 6.14: SCF ERIs (upper) and ERI gradients (lower) timing for the geometry optimization of insulin in 64 processors using the mixed SCF scheme.

This shows the possibilities opened by the combination of the in-core near-field ERIs calculation and the double asymptotic expansion given by the mixed SCF scheme to perform large-scale calculations using an all-electron DFT methodology. Moreover, the combination of these implementations in the framework of a QM/MM or BOMD code will allow studies on the nanoscale size range in reasonable times.



# Chapter 7

## Conclusions and future work

This work has achieved a considerable reduction in the calculation time of electrostatic interaction integrals, a task which was the bottleneck in the computation of large systems in deMon2k. Using the near- and far-field region definitions already implemented, further expansions were developed to reduce the computation time of the commonly numerous far-field integrals. In addition, a new self-consistent field (SCF) scheme was implemented for the calculation time reduction for near-field SCF integrals. This allows deMon2k, an all-electron DFT program, to access a new level of calculation capabilities in reasonable times making a better use of the computational parallel architectures. The conclusions and future work of these implementations are given in the following sections.

### 7.1 Conclusions

1. The double asymptotic expansion is a new methodology which takes care of the calculation of the far-field electron repulsion integrals (ERI). It was derived and implemented on top of the asymptotic expansion already programmed in deMon2k. The benchmarks show a considerable speed-up by employing the double asymptotic expansion instead of the original expansion. At the same time, the accuracy of the energy calculation is kept within the SCF and geometry optimization thresholds without perturbing the convergence behavior. Thus, the use of the original asymptotic expansion becomes obsolete.

2. The definition of near- and far-field regions is based on atomic properties which can be calculated readily from the basis and auxiliary function set definition. Thus, no space division is necessary as in the fast multipole method (FMM). Moreover translation and rotation operators are not required. Strictly speaking, the only translation present in the implementation is related to the centers of Gaussian orbital products but this translation operation is not explicitly performed. By taking primitive products closer to center  $\vec{A}$  to build the double asymptotic expansion on  $\vec{A}$  (and vice versa for center  $\vec{B}$ ) high accuracies with relative low expansion orders are achieved.
3. The double asymptotic expansion yields a considerably simpler form for the ERIs, namely a modified overlap integral form. This modified overlap integral has analytic solutions, thereby obviating the need for the calculation (and interpolation) of the non-analytic Boys function. In addition, the contributions of the auxiliary function potential are shifted to the atomic level enabling a factorization that accelerates the overall far-field ERI calculation.
4. The form of the asymptotic expansion from which the double asymptotic expansion was derived resembles very much the nuclear attraction integral (NAI). An asymptotic form of the NAI was derived and implemented for the electrostatic point charge embedding in deMon2k. This form achieved remarkable speed-ups for systems with hundreds of thousands of point charges. This implementation allows deMon2k to be used efficiently in combination with other programs to perform so-called QM/MM calculations.
5. Although the far-field ERIs bottleneck was resolved, the near-field ERIs bottleneck remained. A new SCF scheme was developed and implemented in order to combine the benefits of the conventional and direct SCF schemes present in deMon2k. The far-field ERIs are calculated using the direct SCF methodology whereas the near-field ERIs are stored in RAM. This so-called mixed SCF approach was programmed to take advantage of parallel computational architectures making efficient use of the available RAM. This additional implementation removed completely the ERIs bottleneck from all-electron DFT calculations in deMon2k.

## 7.2 Future work

1. Several implementations of the asymptotic expansions presented here can be readily achieved. Examples include:
  - Implementation of the asymptotic expansion for the nuclear attraction integrals.
  - Implementation of the double asymptotic expansion for the Coulomb matrix integrals (see appendix B).
  - Implementation of the double asymptotic expansion in the molecular property calculations, e.g. nuclear magnetic resonance of embedded systems.
2. The benchmarks of the embedding calculations for several hundreds and millions of point charges show an overhead that is not associated with the actual integral calculation. Time profiles showed that this overhead originates from the interatomic distance calculation despite its simple form. Thus, a new approach for the near- and far-field integral classification must be implemented in order to eliminate this bottleneck.
3. The memory usage by work fields in the far-field integral calculation can reach the order of Gigabytes when millions of atoms or point charges are processed. It is mandatory to reduce the memory requirement of such work fields. The solution of this issue can be the implementation of a batching algorithm in which the atom and point charge information is efficiently distributed over the parallel computational architecture.
4. The remarkable time reduction of the double asymptotic expansion of far-field ERIs opens a new possibility for electrostatic embedding implementations. Instead of using point charges one can now think about the use of approximate densities. Since the near-field embedding region can be rapidly saturated, the main time consumption would come from the far-field embedding region, which can be handled by the double asymptotic expansion. This new embedding scheme would make the electrostatic environment more realistic and even would open the opportunity to introduce non-classical interactions in the embedding interaction.

5. There is another bottleneck which was not treated in this work: Linear algebra. Matrix diagonalization and multiplication are now the bottleneck in deMon2k not only since the molecular integral calculation time has been remarkably reduced but also because the systems which are now available for calculation are bigger. SCF matrices become difficult to store and handle when the system size reaches many thousands of atoms and the matrix operations require more computational time. An efficient distribution algorithm for matrix storage and calculation is required in order to solve this bottleneck.

# Appendices



# Appendix A

## The positive semidefinite nature of the variational fitting error

The variational fitting of the Coulomb potential (VFCP) shown in section 2.2 relies on the minimization of the error given by Eq. (2.16):

$$\mathcal{E} = \frac{1}{2} \iint \frac{[\rho(\vec{r}) - \tilde{\rho}(\vec{r})][\rho(\vec{r}') - \tilde{\rho}(\vec{r}')]d\vec{r}d\vec{r}'}{|\vec{r} - \vec{r}'|} \quad (\text{A.1})$$

In order to demonstrate the property  $\mathcal{E} \geq 0$  we will show that the following relation holds for a charge distribution  $\rho$ :

$$\mathcal{U} = \frac{1}{2} \iint \frac{\rho(\vec{r})\rho(\vec{r}')}{|\vec{r} - \vec{r}'|} d\vec{r}d\vec{r}' \geq 0, \quad (\text{A.2})$$

where  $\mathcal{U}$  is the Coulomb energy. Then, we will show that the same relations which determines  $\mathcal{U} \geq 0$  [156] apply to  $\mathcal{E}$ .

The electric field  $\vec{\mathbf{E}}$  at  $\vec{r}$  generated by a charge distribution  $\rho$  is defined as:

$$\vec{\mathbf{E}}(\vec{r}) = \int \rho(\vec{r}') \frac{\vec{r} - \vec{r}'}{|\vec{r} - \vec{r}'|^3} d\vec{r}' \quad (\text{A.3})$$

Since the electric field is conservative it can be written as the gradient of a scalar field. Using the relation:

$$\nabla_{\vec{r}} \frac{1}{|\vec{r} - \vec{r}'|} = -\frac{\vec{r} - \vec{r}'}{|\vec{r} - \vec{r}'|^3}, \quad (\text{A.4})$$

where the subindex in  $\nabla_{\vec{r}}$  means that the operator acts on  $\vec{r}$ , the electric field definition can be written as:

$$\vec{\mathbf{E}}(\vec{r}) = -\int \rho(\vec{r}') \nabla_{\vec{r}} \frac{1}{|\vec{r} - \vec{r}'|} d\vec{r}' = -\nabla_{\vec{r}} \int \rho(\vec{r}') \frac{1}{|\vec{r} - \vec{r}'|} d\vec{r}' \equiv -\nabla \Phi(\vec{r}) \quad (\text{A.5})$$

where the subindex for  $\nabla$  in the last equivalence renders useless. Thus, the electrostatic potential has been defined as:

$$\Phi(\vec{r}) = \int \rho(\vec{r}') \frac{1}{|\vec{r} - \vec{r}'|} d\vec{r}' \quad (\text{A.6})$$

The divergence theorem gives the relation between the electric field and the charge distribution density:

$$\nabla \cdot \vec{\mathbf{E}}(\vec{r}) = 4\pi\rho(\vec{r}). \quad (\text{A.7})$$

This equation is known as Gauss' law. Substituting Eq. (A.6) and (A.7) in the definition of the Coulomb energy yields:

$$\mathcal{U} = \frac{1}{8\pi} \int (\nabla \cdot \vec{\mathbf{E}}(\vec{r})) \Phi(\vec{r}) d\vec{r} \quad (\text{A.8})$$

Applying the operator  $\nabla$  to the product of a scalar and vector field yields:

$$\nabla \cdot (\chi(\vec{r}) \vec{\mathbf{V}}(\vec{r})) = \vec{\mathbf{V}}(\vec{r}) \cdot \nabla \chi(\vec{r}) + \chi(\vec{r}) \nabla \cdot \vec{\mathbf{V}}(\vec{r}). \quad (\text{A.9})$$

Thus, the Coulomb energy can be written as:

$$\mathcal{U} = \frac{1}{8\pi} \int \nabla \cdot (\Phi(\vec{r}) \vec{\mathbf{E}}(\vec{r})) d\vec{r} - \frac{1}{8\pi} \int \vec{\mathbf{E}}(\vec{r}) \cdot \nabla \Phi(\vec{r}) d\vec{r} \quad (\text{A.10})$$

Using the divergence theorem the first term of Eq. (A.10) can be written in terms of a surface integral as follows:

$$\int \nabla \cdot (\Phi(\vec{r})\vec{\mathbf{E}}(\vec{r})) d\vec{r} = \oint_{\sigma} (\Phi(\vec{r})\vec{\mathbf{E}}(\vec{r})) \cdot \vec{\mathbf{n}} d\sigma, \quad (\text{A.11})$$

where the boundary of the integration surface  $\sigma$  is at infinity. Since  $\vec{\mathbf{E}}(\vec{r})$  is 0 at  $\vec{r} = \infty$ , the result is

$$\int \nabla \cdot (\Phi(\vec{r})\vec{\mathbf{E}}(\vec{r})) d\vec{r} = 0. \quad (\text{A.12})$$

Substituting Eq. (A.5) and (A.12) in Eq. (A.10) yields:

$$\mathcal{U} = \frac{1}{8\pi} \int |\vec{\mathbf{E}}(\vec{r})|^2 d\vec{r}, \quad (\text{A.13})$$

which is greater or equal to 0. In order to show that  $\mathcal{E}$  shares this property, it is enough to show that  $(\rho - \tilde{\rho})$  is a charge distribution that fulfills Eq. (A.5) for the definition of the electrostatic potential and the Gauss' law, Eq. (A.7). The electric field,  $\vec{\mathbf{E}}_{\Delta}(\vec{r})$ , given by the charge distribution  $(\rho - \tilde{\rho})$  is

$$\vec{\mathbf{E}}_{\Delta}(\vec{r}) = \int (\rho(\vec{r}') - \tilde{\rho}(\vec{r}')) \frac{\vec{r} - \vec{r}'}{|\vec{r} - \vec{r}'|^3} d\vec{r}' = \vec{\mathbf{E}}(\vec{r}) - \tilde{\vec{\mathbf{E}}}(\vec{r}). \quad (\text{A.14})$$

Thus, the electrostatic potential for this field is obtained by:

$$\begin{aligned} \vec{\mathbf{E}}_{\Delta}(\vec{r}) &= - \int (\rho(\vec{r}') - \tilde{\rho}(\vec{r}')) \nabla_{\vec{r}} \frac{1}{|\vec{r} - \vec{r}'|} d\vec{r}' = - \nabla_{\vec{r}} \int (\rho(\vec{r}') - \tilde{\rho}(\vec{r}')) \frac{1}{|\vec{r} - \vec{r}'|} d\vec{r}' \\ &= - \nabla_{\vec{r}} \int \rho(\vec{r}') \frac{1}{|\vec{r} - \vec{r}'|} d\vec{r}' + \nabla_{\vec{r}} \int \tilde{\rho}(\vec{r}') \frac{1}{|\vec{r} - \vec{r}'|} d\vec{r}' \\ &\equiv - \nabla \Phi(\vec{r}) + \nabla \tilde{\Phi}(\vec{r}) = - \nabla \Phi_{\Delta}(\vec{r}). \end{aligned} \quad (\text{A.15})$$

Thus, an electrostatic potential can be defined for the electric field generated by  $(\rho - \tilde{\rho})$ :

$$\Phi_{\Delta}(\vec{r}) = \Phi(\vec{r}) - \tilde{\Phi}(\vec{r}) = \int \rho(\vec{r}') \frac{1}{|\vec{r} - \vec{r}'|} d\vec{r}' - \int \tilde{\rho}(\vec{r}') \frac{1}{|\vec{r} - \vec{r}'|} d\vec{r}' \quad (\text{A.16})$$

Using the relation between the electrostatic potential and the electric field, Eq. (A.15), Gauss' law can be written as:

$$\begin{aligned}\nabla \cdot \vec{\mathbf{E}}_{\Delta}(\vec{r}) &= \nabla \cdot \left( \vec{\mathbf{E}}(\vec{r}) - \tilde{\vec{\mathbf{E}}}(\vec{r}) \right) = \nabla \cdot \vec{\mathbf{E}}(\vec{r}) - \nabla \cdot \tilde{\vec{\mathbf{E}}}(\vec{r}) \\ &= 4\pi\rho(\vec{r}) - 4\pi\tilde{\rho}(\vec{r}) = 4\pi(\rho(\vec{r}) - \tilde{\rho}(\vec{r})),\end{aligned}\tag{A.17}$$

since individual electric fields can be written according to Eq. (A.14). Thus, the error given by the VFCEP can be written as:

$$\begin{aligned}\mathcal{E} &= \frac{1}{8\pi} \int (\nabla \cdot \vec{\mathbf{E}}_{\Delta}(\vec{r})) \Phi_{\Delta}(\vec{r}) d\vec{r} \\ &= \frac{1}{8\pi} \int \nabla \cdot (\Phi_{\Delta}(\vec{r}) \vec{\mathbf{E}}_{\Delta}(\vec{r})) d\vec{r} - \frac{1}{8\pi} \int \vec{\mathbf{E}}_{\Delta}(\vec{r}) \cdot \nabla \Phi_{\Delta}(\vec{r}) d\vec{r} \\ &= \frac{1}{8\pi} \int |\vec{\mathbf{E}}_{\Delta}(\vec{r})|^2 d\vec{r} = \frac{1}{8\pi} \int |\vec{\mathbf{E}}(\vec{r}) - \tilde{\vec{\mathbf{E}}}(\vec{r})|^2 d\vec{r},\end{aligned}\tag{A.18}$$

which shows that  $\mathcal{E} \geq 0$ .

# Appendix B

## Double asymptotic expansion of two-center ERIs with HGTF

For the variational fitting of the Coulomb potential as introduced in section 2.2, two-center ERIs over primitive Hermite Gaussian type functions (HGTFs) are needed

$$[\bar{\mathbf{c}}|\bar{\mathbf{d}}] = \iint \frac{\bar{\mathbf{c}}(\vec{r}_1)\bar{\mathbf{d}}(\vec{r}_2)}{|\vec{r}_1 - \vec{r}_2|} d\vec{r}_1 d\vec{r}_2. \quad (\text{B.1})$$

This ERI can be rewritten as a one-electron integral in the following way

$$[\bar{\mathbf{c}}|\bar{\mathbf{d}}] = \int \bar{\mathbf{c}}(\vec{r}_1)\phi_{\bar{\mathbf{d}}}(\vec{r}_1)d\vec{r}_1, \quad (\text{B.2})$$

where the potential  $\phi_{\bar{\mathbf{d}}}(\vec{r})$  is defined as in Eq. (3.67). The asymptotic expansion given in Eq. (3.72) then applied to Eq. (B.2) yields

$$[\bar{\mathbf{c}}|\bar{\mathbf{d}}] \sim \left(\frac{\pi}{\zeta_{\bar{\mathbf{d}}}}\right)^{3/2} \left(\frac{\partial}{\partial D_x}\right)^{\bar{d}_x} \left(\frac{\partial}{\partial D_y}\right)^{\bar{d}_y} \left(\frac{\partial}{\partial D_z}\right)^{\bar{d}_z} \int \frac{\bar{\mathbf{c}}(\vec{r}_1)}{|\vec{r}_1 - \vec{D}|} d\vec{r}_1 = [\bar{\mathbf{c}}|\hat{\mathcal{A}}_D(\bar{\mathbf{d}})]. \quad (\text{B.3})$$

The last equality comes from the definition in Eq. (3.13). The integral in Eq. (B.3) is a nuclear attraction-like integral with the "nuclear center" on  $\vec{D}$ . Taking advantage of the HGTF definition, the last part of Eq. (B.3) can be written in the following way

$$[\bar{\mathbf{c}}|\hat{\mathcal{A}}_D(\bar{\mathbf{d}})] = \hat{D}_C(\bar{\mathbf{c}})\hat{D}_D(\bar{\mathbf{d}})[\bar{\mathbf{s}}_C|\hat{\mathcal{A}}_D(\bar{\mathbf{0}})] = \hat{D}_C(\bar{\mathbf{c}})\hat{D}_D(\bar{\mathbf{d}})\left[\frac{2\pi}{\zeta_{\bar{\mathbf{c}}}}F_0(\zeta_{\bar{\mathbf{a}}}(\vec{C} - \vec{D})^2)\right], \quad (\text{B.4})$$

where

$$\hat{\mathcal{D}}_C(\bar{\mathbf{c}}) \equiv \left(\frac{\partial}{\partial C_x}\right)^{\bar{c}_x} \left(\frac{\partial}{\partial C_y}\right)^{\bar{c}_y} \left(\frac{\partial}{\partial C_z}\right)^{\bar{c}_z} \quad \text{and} \quad \hat{\mathcal{D}}_D(\bar{\mathbf{d}}) \equiv \left(\frac{\partial}{\partial D_x}\right)^{\bar{d}_x} \left(\frac{\partial}{\partial D_y}\right)^{\bar{d}_y} \left(\frac{\partial}{\partial D_z}\right)^{\bar{d}_z} \quad (\text{B.5})$$

Applying once again the asymptotic expansion from Eq. (3.72) to the Boys function in Eq. (B.4) and substituting in (B.3) yields

$$[\bar{\mathbf{c}}||\bar{\mathbf{d}}] \sim \left(\frac{\pi}{\zeta_{\bar{\mathbf{c}}}}\right)^{3/2} \left(\frac{\pi}{\zeta_{\bar{\mathbf{d}}}}\right)^{3/2} \hat{\mathcal{D}}_C(\bar{\mathbf{c}}) \hat{\mathcal{D}}_D(\bar{\mathbf{d}}) \frac{1}{|\vec{C} - \vec{D}|}. \quad (\text{B.6})$$

Using the relation

$$\left(\frac{\partial}{\partial C_i}\right)^{\bar{c}_i} \left(\frac{\partial}{\partial D_i}\right)^{\bar{d}_i} \frac{1}{C_i - D_i} = (-1)^{\bar{d}_i} \left(\frac{\partial}{\partial C_i}\right)^{\bar{c}_i + \bar{d}_i} \frac{1}{C_i - D_i}, \quad (\text{B.7})$$

the double asymptotic expansion of two-center ERIs over HGTFs is given by

$$\begin{aligned} [\bar{\mathbf{c}}||\bar{\mathbf{d}}] &\sim (-1)^{\bar{d}} \left(\frac{\pi}{\zeta_{\bar{\mathbf{c}}}}\right)^{3/2} \left(\frac{\pi}{\zeta_{\bar{\mathbf{d}}}}\right)^{3/2} \hat{\mathcal{D}}_C(\bar{\mathbf{c}} + \bar{\mathbf{d}}) \frac{1}{|\vec{C} - \vec{D}|} \\ &= (-1)^{\bar{c}} \left(\frac{\pi}{\zeta_{\bar{\mathbf{c}}}}\right)^{3/2} \left(\frac{\pi}{\zeta_{\bar{\mathbf{d}}}}\right)^{3/2} \hat{\mathcal{D}}_D(\bar{\mathbf{c}} + \bar{\mathbf{d}}) \frac{1}{|\vec{C} - \vec{D}|}. \end{aligned} \quad (\text{B.8})$$

Thus, the double asymptotic expansion of two-center ERIs possesses the same symmetry as the original integrals.

# Bibliography

- [1] Diels, H.; Kranz, W. *Die Fragmente der Vorsokratiker, Griechisch und Deutsch*, sixth edition; Weidmann: Berlin (1951).
- [2] Taylor, C. C. W. *The Atomists: Leucippus and Democritus. Fragments, A Text and Translation with Commentary*; University of Toronto Press: Toronto (1999).
- [3] Aristotle, *The Complete Works of Aristotle, Vol. I and II*; Barnes, J.; Princeton University Press: Princeton (1984).
- [4] Lavoisier, A. L. *Traité élémentaire de Chimie*; Cuchet: Paris (1789).
- [5] Proust, J. L. *Ann. Chimie*, **32**, 26 (1799).
- [6] Dalton, J. *A New System of Chemical Philosophy*; Russel, S.; Citadel Press: New York (1964).
- [7] Dalton, J. *Ann. Phil.*, **3**, 174 (1814).
- [8] Newlands, J. A. R. *Chemical News* , **10**, 94 (1864).
- [9] Newlands, J. A. R. *Chemical News* , **12**, 83 (1865).
- [10] Mendeleev, D. *Zeitschrift für Chemie*, **12**, 405 (1869).
- [11] Thomson, J. J. *Phil. Mag. Series 5*, **44**, 293 (1897).
- [12] Stoney, G. J. *Phil. Mag. Series 5*, **38**, 418 (1894).
- [13] Rutherford, E. *Phil. Mag. Series 6*, **21**, 669 (1911).
- [14] Chadwick, J. *Nature*, **192**, 312 (1932).

- [15] Bohr, N. *Phil. Mag. Series 6*, **26**, 1 (1913).
- [16] Sommerfeld, A. *Atombau und Spektrallinien*; Friedrich Vieweg und Sohn: Braunschweig (1919).
- [17] Uhlenbeck, G. E.; Goudsmit, S. *Naturwissenschaften* **47** 953 (1925).
- [18] Pauli, W. *Zeit. für Phys. A Hadrons and nuclei* **31** 765 (1925).
- [19] Einstein, A. *Ann. der Phys.* **17**, 132 (1905).
- [20] de Broglie, L. *Ann. de Phys. 10th series, tome III*; Masson & C. Éditeurs: Paris (1925).
- [21] Heisenberg, W. *Zeit. für Physik A Hadrons and Nuclei*, **33**, 879 (1925).
- [22] Schrödinger, E. *Phys. Rev.*, **28**, 1049 (1926).
- [23] Szabo, A.; Ostlund, N. S. *Modern Quantum Chemistry*; Dover Publishing: Mineola (1996).
- [24] Thomas, L. H. *Proc. Cambridge Phil. Soc.*, **23**, 542 (1927).
- [25] Fermi, E. *Rend. Accad. Naz. Lincei*, **6**, 602 (1927).
- [26] Dirac, P. A. M. *Math. Proc. Camb. Phil. Soc.*, **26**, 376 (1930).
- [27] Wigner, E; Seitz, F. *Phys. Rev.*, **43**, 804 (1933).
- [28] Wigner, E; Seitz, F. *Phys. Rev.*, **46**, 509 (1934).
- [29] Slater, J. C. *Phys. Rev.*, **81**, 385 (1951).
- [30] Gaspar, R. *Acta Phys. Acad. Scientiarum Hungaricae*, **3**, 263 (1954).
- [31] Slater, J. C.; Johnson, K. H. *Phys. Rev. B*, **5**, 844 (1972).
- [32] Slater, J. C. *Phys. Rev.*, **51**, 846 (1937).
- [33] Martin, R. M. *Electronic Structure: Basic Theory and Applications*; Cambridge University Press: Cambridge (2004).

- [34] Hohenberg, P.; Kohn, W. *Phys. Rev.*, **136** (3B), B864-B871 (1964).
- [35] Kohn, W.; Sham, L. J. *Phys. Rev.*, **140**, A1133 (1965).
- [36] Roothaan, C. C. J. *Rev. Mod. Phys.*, **23**, 69 (1951).
- [37] Hall, G. G. *Proc. Roy. Soc. Lond. A*, **205**, 541 (1951).
- [38] Helgaker, T.; Jørgensen, P.; Olsen, J. *Molecular Electronic-Structure Theory*, Wiley: Chichester (2000).
- [39] Dunlap, B. I.; Rösch, N.; Trickey, S. B. *Mol. Phys.*, **108**, 3167 (2010).
- [40] Baerends, E. J.; Ellis, D. E.; Ros, P. *Chem. Phys.*, **2**, 41 (1973).
- [41] Sambe, H.; Felton, R. H. *J. Chem. Phys.*, **62**, 1122 (1975).
- [42] Dunlap, B. I.; Connolly, J. W.; Sabin, J. R. *J. Chem. Phys.*, **71**, 4993 (1979).
- [43] Mintmire, J. W.; Dunlap, B. I. *Phys. Rev. A*, **25**, 88 (1982).
- [44] Köster, A. M.; Reveles, J. U.; del Campo, J. M. *J. Chem. Phys.* **121**, 3417 (2004).
- [45] Köster, A. M.; Flores-Moreno, R.; Reveles, J. U. *J. Chem. Phys.* **121**, 681 (2004).
- [46] Köster, A. M.; Geudtner, G.; Calaminici, P.; Casida, M. E.; Dominguez, V. D.; Flores-Moreno, R.; Gamboa, G. U.; Goursot, A.; Heine, T.; Ipatov, A.; Janetzko, F.; del Campo, J. M.; Reveles, J. U.; Vela, A.; Zuniga-Gutierrez B.; Salahub, D. R. *deMon2k, Version 3*, The deMon developers, CINVESTAV, Mexico City (2011).
- [47] Atkins, P. W. *Molecular quantum mechanics*, second edition; Oxford University Press: New York (1983).
- [48] Born, M.; Oppenheimer, J. R. *Ann. Physik*, **84**, 457 (1927).
- [49] Born, M.; Fock, V. A. *Zeitschrift für Physik A Hadrons and Nuclei*, **51**, 165 (1928).

- [50] Handy, N. C.; Lee, A. M. *Chem. Phys. Lett.*, **252**, 425 (1996).
- [51] del Campo Ramirez, J. M. *Exploring chemical reactivity with auxiliary density functional theory*, Ph.D. Thesis, CINVESTAV, Mexico City (2008).
- [52] Sherrill, C. D. The Born-Oppenheimer approximation in *General Quantum Chemistry*. Available in <http://vergil.chemistry.gatech.edu/notes/bo/bo.pdf> (March 2005).
- [53] Roos, B. O.; Taylor, P. R.; Siegbahn, P. E. M. *Chem. Phys.*, **48**, 157 (1980).
- [54] Purvis, G. D.; Bartlett, R. J. *J. Chem. Phys.*, **76**, 1910 (1982).
- [55] Epstein, S. T. *The Variation Method in Quantum Chemistry*, Academic Press, Inc: New York (1974).
- [56] Capelle, K. *Braz. J. Phys.* **36**, 1318 (2006).
- [57] Jones, O. R. Introduction to Density Functional Theory and Exchange-Correlation Energy Functionals. In *Computational Nanoscience: Do It Yourself!*; Grotendorst, J.; Blügel, S.; Marx, D.; NIC Series, Vol. 31; John von Neumann Institute for Computing: Jülich (2006).
- [58] Perdew, J. P.; Levy, M. *Phys. Rev. B*, **31**, 6264 (1985).
- [59] Gunnarsson, O.; Lundqvist, B. I. *Phys. Rev. B*, **13**, 4274 (1976).
- [60] Parr, R. G.; Yang, W. *Density-Functional Theory of Atoms and Molecules*; Wellesley-Cambridge Press: New York (1989).
- [61] Teller, E. *Rev. Mod. Phys.*, **34**, 627 (1962).
- [62] Wesolowski, T. A.; Warshel, A. *Int. J. of Quant. Chem.*, **61**, 303 (1997).
- [63] Ho, G. S.; Lignères, V. L.; Carter, E. A. *Phys. Rev. B*, **78**, 045105 (2008).
- [64] Vosko, S. H.; Wilk, L.; Nusair, M. *Can. J. Phys.*, **58**, 1200 (1980).
- [65] Becke, A. D. *Phys. Rev. A*, **38**, 3098 (1988).

- [66] Lee, C.; Yang, W.; Parr, R. G. *Phys. Rev. B*, **37**, 785 (1988).
- [67] Perdew, J. P.; Chevary, J. A.; Vosko, S. H.; Jackson, K. A.; Pederson, M. R.; Singh, D. J.; Fiolhais, C. *Phys. Rev. B*, **46**, 6671 (1992).
- [68] Perdew, J. P.; Wang, Y. *Phys. Rev. B*, **45**, 13244 (1992).
- [69] Perdew, J. P.; Burke, K.; Ernzerhof, M. *Phys. Rev. Lett.*, **77**, 3865 (1996).
- [70] Stephens, P.J.; Devlin, F.; Chabalowski, C.F.; Frisch, M.J. *J. Phys. Chem.*, **98**, 11623 (1994).
- [71] Adamo, C.; Barone, V. *J. Chem. Phys.*, **110**, 6158 (1999).
- [72] Becke, A. D. *J. Chem. Phys.*, **107**, 8554 (1997).
- [73] Becke, A. D. *J. Chem. Phys.*, **109**, 2092 (1998).
- [74] Perdew, J. P.; Kurth, S.; Zupan, A.; Blaha, P. *Phys. Rev. Lett*, **82**, 2544 (1999).
- [75] Van Voorhis, T.; Scuseria, G. E. *J. Chem. Phys.*, **109**, 400 (1998).
- [76] Cohen, A. J.; Handy, N. C. *Chem. Phys. Lett.*, **316**, 160 (2000).
- [77] Scuseria, G. E.; Staroverov, V. N. Progress in the development of exchange-correlation functionals. In *Theory and Applications of Computational Chemistry: The First 40 Years*; Dykstra, C. E.; Frenking, G.; Kim, K. S.; Scuseria, G. E.; Elsevier: Amsterdam (2005).
- [78] Boys, S. F. *Proc. R. Soc. Lond. A*, **200**, 542 (1950).
- [79] Saunders, V. R. Molecular integrals for Gaussian type functions. In *Methods in Computational Molecular Physics*; Diercksen, G.H.F.; Wilson S.; Reidel Publishing Company: Dordrecht (1983).
- [80] Roothaan, C. C. J. *Rev. Mod. Phys.*, **32**, 179 (1960).
- [81] Pople, J. A.; Nesbet, R. K. *J. Chem. Phys.*, **22**, 571 (1954).
- [82] Binkley, J. S.; Pople, J. A.; Dobosh, P. A. *Mol. Phys.*, **28**, 1423 (1974).

- [83] McMurchie, L. E.; Davidson, E. R. *J. Comput. Phys.*, **26**, 218 (1978).
- [84] Köster, A. M. *J. Chem. Phys.*, **104**, 4114 (1996).
- [85] Andzelm, J.; Russo, N.; Salahub, D. R. *J. Chem. Phys.*, **87**, 6562 (1987).
- [86] Köster, A. M. *J. Chem. Phys.*, **118**, 9943 (2003).
- [87] Press, W. H.; Teukolsky, S. A.; Vetterling, W. T.; Flannery, B. P. *Numerical Recipes in FORTRAN: The Art of Scientific Computing*; Cambridge University Press: New York (1992).
- [88] Domínguez Soria, V. D. *Cálculos de sistemas grandes basados en la teoría de funcionales de la densidad auxiliar: implementación y aplicaciones*, Ph.D. Thesis, CINVESTAV, Mexico City (2009).
- [89] Domínguez-Soria, V. D.; Geudtner, G.; Morales, J. L.; Calaminici, P.; Köster, A. M. *J. Chem. Phys.* **131**, 124102 (2009).
- [90] Trickey, S. B.; Alford, J. A.; Boettger, J. C. Methods and Implementation of Robust, High-Precision Gaussian Basis DFT Calculations for Periodic Systems: the GTOFF Code. In *Computational Materials Science: Theoretical and Computational Chemistry, Vol. 15*; Leszczynski, J.; Elsevier: Amsterdam (2004).
- [91] Trickey, S. B., private communication to Köster, A. M. (unpublished).
- [92] Hartree, D. R. *The calculation of atomic structures*; Wiley: New York (1957).
- [93] Cancés, E. *J. Chem. Phys.* **114**, 10616 (2001).
- [94] Pulay, P. *J. Comp. Chem* **3**, 556 (1982).
- [95] Köster, A. M.; del Campo, J. M.; Janetzko, F.; Zuniga-Gutierrez, B. *J. Chem. Phys.* **130**, 114106 (2009).
- [96] Góllebiewski, A.; Mrozek, J. *Int. J. Quant. Chem.*, **7**, 623 (1973).
- [97] Singer, K. *Proc. R. Soc. Lond. A*, **258**, 412 (1960).
- [98] Obara, S.; Saika, A. *J. Chem. Phys.*, **84**, 3963 (1986).

- [99] Köster, A. M. *Entwicklung einer LCGTO-Dichtefunktionalmethode mit Hilfsfunktionen*, Habilitation thesis, Universität Hannover, Hannover (1998).
- [100] Head-Gordon, M.; Pople, J. A. *J. Chem. Phys.*, **89**, 5777 (1988).
- [101] Živković, T.; Maksić, Z. B. *J. Chem. Phys.*, **49**, 3083 (1968).
- [102] Harris, F. E. *Int. J. Quant. Chem.*, **23**, 1469 (1983).
- [103] Gill, P. M. W.; Head-Gordon, M.; Pople, J. A. *Int. J. Quant. Chem.*, **36**, 269 (1989).
- [104] Gill, P. M. W.; Head-Gordon, M.; Pople, J. A. *J. Phys. Chem.*, **94**, 5564 (1990).
- [105] Hamilton, T. P.; Schaefer, H. F. *Chem. Phys.*, **150**, 163 (1991).
- [106] Lindh, R.; Ryu, U.; Liu, B. *J. Chem. Phys.*, **95**, 5889 (1991).
- [107] Ryu, U.; Lee, Y. S.; Lindh, R. *Chem. Phys. Lett.*, **185**, 562 (1991).
- [108] Johnson, B. G.; Gill, P. M. W.; Pople, J. A. *Chem. Phys. Lett.*, **206**, 229 (1993).
- [109] Valeev, E. F.; Schaefer, H. F. *J. Chem. Phys.*, **113**, 3990 (2000).
- [110] Andzelm, J.; Wimmer, E.; Salahub, D. R. *ACS Symp. Ser.*, **394**, 228 (1989).
- [111] Fournier, R.; Andzelm, J.; Salahub, D. R. *J. Chem. Phys.*, **90**, 6371 (1989).
- [112] Andzelm, J.; Wimmer, E. *J. Chem. Phys.*, **96**, 1280 (1992).
- [113] Almlöf, J.; Faegri, K.; Korsell, K. *J. Comp. Chem.* **3**, 385 (1982).
- [114] White, C. A.; Head-Gordon, M. *J. Chem. Phys.*, **104**, 2620 (1996).
- [115] Dalgarno, A. L.; Stewart, A. L. *Proc. R. Soc. Lond. A*, **238**, 269 (1956).
- [116] Pulay, P. *Mol. Phys.*, **17**, 197 (1969).
- [117] Reveles Ramirez, J. U. *Geometry optimization in LCGTO-DFT methods with auxiliary functions*, Ph.D. Thesis, CINVESTAV, Mexico City (2004).

- [118] Flores-Moreno, R. *Analytic derivatives in LCGTO-DFT pseudo-potential methods with auxiliary functions*, Ph.D. Thesis, CINVESTAV, Mexico City (2006).
- [119] Korminicki, A.; Ishida, K.; Morokuma, K.; Ditchfield, R.; Conrad, N. *Chem. Phys. Lett.*, **45**, 595 (1977).
- [120] Challacombe, M.; Schwegler, E.; Almlöf, J. *Chem. Phys. Lett.* **241**, 67 (1995).
- [121] Greengard, L.; Rokhlin, V. *J. Comp. Phys.* **73**, 325 (1987).
- [122] White, C. A.; Head-Gordon, M. *J. Chem. Phys.* **101**, 6593 (1994).
- [123] Petersen, H. G.; Soelvason, D.; Perram, J. W.; Smith, E. R. *J. Chem. Phys.* **101**, 8870 (1994).
- [124] Kudin, K. N.; Scuseria, G. E. *Chem. Phys. Lett.* **283**, 61 (1998).
- [125] White, C. A.; Johnson, B. G.; Gill, P. M. W.; Head-Gordon, M. *Chem. Phys. Lett.* **230**, 8 (1994).
- [126] Strain, M. C.; Scuseria, G. E.; Frisch, M. J. *Science* **271**, 51 (1996).
- [127] Kudin, K. N.; Scuseria, G. E. *Phys. Rev. B* **61**, 16440 (2000).
- [128] Stone, A. J. *The Theory of Intermolecular Forces*, Clarendon Press: Oxford, UK, 1996.
- [129] Quintanar, C.; Caballero, R.; Köster, A. M. *Int. J. Quant. Chem.* **96**, 483 (2004).
- [130] Warshel, A.; Levitt, M. *J. Mol. Biol.* **103**, 227 (1976).
- [131] Alvarez-Ibarra, A.; Köster, A. M.; Zhang R.; Salahub, D. R. *J. Chem. Theor. Comput.* **8**, 4232 (2012).
- [132] Köster, A. M., private communication (unpublished).

- [133] Köster, A. M.; Calaminici, P.; Gómez, Z.; Reveles, J. U. Density functional theory calculation of transition metal clusters. In *Reviews of Modern Quantum Chemistry. A celebration of the contribution of Robert G. Parr, Vol. II*; Sen, K.; World Scientific, Singapore, Singapore, 2002.
- [134] Clementi, E., *J. Chem. Phys.*, **38**, 996 (1963).
- [135] Mintmire, J. W.; Sabin, J. R.; Trickey, S. B. *Phys. Rev. B* **26**, 1743 (1982).
- [136] Godbout, N.; Salahub, D. R.; Andzelm, J.; Wimmer, E. *Can. J. Phys.* **70**, 560 (1992).
- [137] Krack, M.; Köster, A. M. *J. Chem. Phys.* **108**, 3226 (1998).
- [138] Saunders, V. R.; Hillier, I. H. *Int. J. Quant. Chem.* **7**, 699 (1973).
- [139] Grande-Aztatzi, R.; Rivillas-Acevedo, L.; Quintanar, L.; Vela, A. *J. Phys. Chem. B* **117**, 789 (2013)
- [140] Mignon, P.; Ugliengo, P.; Sodupe, M. *J. Phys. Chem. C* **113**, 13741 (2009)
- [141] Rimola, A.; Aschi, M.; Orlando, R.; Ugliengo, P. *J. Am. Chem. Soc.* **134**, 10899 (2012)
- [142] Rodríguez-Romero, J.; Aparicio-Ixta, L.; Rodríguez, M.; Ramos-Ortíz, G.; Maldonado, J. L.; Jiménez-Sánchez, A.; Farfán, N.; Santillan, R. *Dyes Pigments* **98**, 31 (2013).
- [143] Rimola, A.; Cono, M.; Zicovich-Wilson, C. M.; Ugliengo, P. *Phys. Chem. Chem. Phys.* **11**, 9005 (2009).
- [144] Rojas, A.; San-Roman, M. L.; Zicovich-Wilson, C. M.; Cambor, M. A. *Chem. Mater.* **25**, 729 (2013).
- [145] Ramos, G.; Grande-Aztatzi, R.; Solorza-Feria, O.; Vela, A. La Química Computacional en el desarrollo de celdas de combustible. In *Energías Renovables Biológicas - Hidrógeno-Pilas de Combustible-II*. Ríos-Leal, E.; Solorza-Feria, O.; Poggi-Varaldo, H. M.; ICYTDF: Mexico City (2009).

- [146] Zhang, R.; Salahub, D. R. *Unpublished* (2013).
- [147] Calaminici, P.; Köster, A. M. *In preparation* (2013).
- [148] Vásquez-Pérez, J. M.; Calaminici, P.; Köster, A. M. *Submitted* (2013).
- [149] Nosé, S. *J. Chem. Phys.* **81**, 511 (1984).
- [150] Hoover, W. G. *Phys. Rev. A* **31**, 1695 (1985).
- [151] Martyna, G. J.; Klein, M. L.; Tuckerman, M. *J. Chem. Phys.* **97**, 2635 (1992).
- [152] Geudtner, G.; Janetzko, F.; Köster, A. M.; Vela, A.; Calaminici, P. *J. Comput. Chem.* **27**, 483 (2006).
- [153] Ferrenberg, A. M.; Swendsen, R. H. *Phys. Rev. Lett.* **61**, 2635 (1988).
- [154] Ferrenberg, A. M.; Swendsen, R. H. *Phys. Rev. Lett.* **63**, 1195 (1989).
- [155] Bocian, W.; Sitkowski, J.; Bednarek, E.; Tarnowska, A.; Kawęcki, R.; Kozerski, L. *J. Biomol. NMR* **40**, 55 (2008).
- [156] Boas, M. L., Vector Analysis. In *Mathematical methods in the physical sciences*, Wiley: New York (1983).